Investigating Interactions of Deuterons and Protons with the Hydrogen Pellet Target of the CELSIUS/WASA Experiment.

Dissertation
zur Erlangung des Doktorgrades
des Fachbereichs Physik
der Universität Hamburg

vorgelegt von
Levent Demirörs
aus Hamburg

Hamburg
2005

Gutachter der Dissertation:	Prof. Dr. W. Scobel Doz. Dr. K.–Th. Brinkmann
Gutachter der Disputation:	Prof. Dr. W. Scobel Prof. Dr. U. Strohbusch
Datum der Disputation:	14. April 2005
Vorsitzender des Prüfungsausschusses:	Dr. H. D. Rüter
Vorsitzender des Promotionsausschusses:	Prof. Dr. G. Huber
Dekan des Fachbereichs Physik	Prof. Dr. G. Huber

Kurzfassung

Der WASA Detektor ist ein vielseitiges Nachweisgerät, das speziell zur Untersuchung der Produktion von Mesonen und ihrer Zerfällen entworfen wurde. Beheimatet am CELSIUS Protonensynchrotron bietet es eine fast vollständige Abdeckung des Raumwinkels im Laborsystem und eine Ratenfestigkeit für Luminositäten von bis zu 10^{32} cm^{-2}s^{-1}. Um so hohe Reaktionsraten erreichen zu können, wurde ein einzigartiger Generator für gefrorene Wasserstoffkügelchen entwickelt, deren Protonen als Stosspartner für den zirkulierenden CELSIUS–Strahl dienen.

Die vorliegenden Arbeit wurde in der Phase der Inbetriebnahme des WASA Detektors begonnen. In ihr wird die Analyse zweier unabhängiger Datensätze vorgestellt. Der erste wurde in einer Messung im November 2001 aufgenommen. Das Ziel dieser Messung war die Fortsetzung des Programms aus dem vorhergehenden Experiment am IUCF in Bloomington (Indiana) [R$^+$93, Roh94] und des PROMICE/WASA Experiments [Gre99, G$^+$00].

Beide Experimente haben sich mit der genauen Vermessung der schwellennahen Pionenproduktion im Deuteron–Proton–System gemäß $pd \to pd\pi^0$ beschäftigt. Die experimentell gewonnenen Verteilungen wurden mit dem Spectator Model [MN93] verglichen, einem phänomenologischen Modell, das die Pionenproduktion als einen quasifreien Prozess beschreibt, dem die Nukleon–Nukleon–Reaktion $pn \to d\pi^0$ zugrunde liegt. Es stellte sich heraus, dass dieses Modell allein nicht in der Lage ist die differentiellen Verteilungen zu beschreiben, es mussten kohärente Mechanismen, in denen alle drei Nukleonen an der Wechselwirkung beteiligt sind, in die Modellbeschreibung hinzugenommen werden. Ähnlich sahen die Ergebnisse für den Bremsstrahlungsprozess $dp \to dp\gamma$ aus, der in [Gre99, G$^+$02] zum ersten Mal in dem hier vorliegenden Energiebereich gemessen wurde.

Die hier vorgestellten Messungen zielten auf eine Verbesserung der Datenlage für die Reaktion $dp \to dp\pi^0$ und $dp \to dp\gamma$ durch eine höhere Detektorakzeptanz ab, um die Ergebnisse aus [G$^+$00, G$^+$02] abzusichern bzw. nachzuprüfen. Tatsächlich bestätigt sich die Zusammensetzungen der Modellbeschreibungen mit der gegenüber dem Vorexperiment abgewandelten Akzeptanzverteilung über den Phasenraum. Allerdings erlaubt die niedrigere Statistik der vorliegenden Messungen keine Verbesserung der früheren quantitativen Aussagen. Ursache waren die niedrige Lebensdauer des Deuteronenstrahles der Energie $T_d = 560$ MeV sowie ein hoher Untergrund durch einen aufgeweiteten Strahl, beides eine Folge der Wechselwirkung des Deuteronenstrahles mit dem Wasserstofftarget. Zusätzlich fehlte eine simultan gemessene, gut bekannte Referenzreaktion zur Kalibration, Luminositätsbestimmung und zur Minimierung der systematischen Fehler.

Zum besseren Verständnis des WASA Detektors wird ein zweiter Satz von Daten analysiert, die in dem Zeitraum vom Dezember 2002 bis zum Dezember 2003 aufgenommen wurden. Um die experimentellen Schwierigkeiten der vorangegangenen Analyse zu vermeiden, werden Daten vorgestellt, die mit einem Protonenstrahl der Energie $T_p = 1.36$ GeV gemessen wurden. Die sowohl aus diesen Daten selektierten als auch mit Monte Carlo Methoden simulierten Ereignisse der elastischen Proton–Proton–Streuung werden verwendet, um die Position der Strahl–Target–Wechselwirkung (Vertexposition) und die Luminosität zu bestimmen. Die Vertexposition weicht im Rahmen der Fehler in allen drei Raumrichtungen von der nominellen Position etwas zu kleineren Werten ab. Die Luminosität lässt sich mit einem systematischen Fehler kleiner als 5% bestimmen und steigt im untersuchten Zeitraum um etwa einen Faktor sieben auf $6 \cdot 10^{30}$ cm^{-2}s^{-1} im Dezember 2003.

Abstract

The WASA detector is a multi–purpose detection system designed to investigate the production of mesons and their decays at the CELSIUS hadron storage ring. Together with a unique target system that provides small frozen hydrogen or deuterium spheres, it is optimized to measure all final state particles in hadron–hadron collisions due to its near to 4π solid angle coverage in the laboratory system and to cope with high luminosities up to 10^{32} cm^{-2}s^{-1}.

In this work, the analysis of data taken during the commissioning phase of the CELSIUS/WASA experiment is described. Experimental data taken in November, 2001 and in the time period from December, 2002 till December, 2003 are analyzed.

The analysis of the former data set focuses on the continuation of the physics program from the preceding experiments at the IUCF in Bloomington, Indiana [R$^+$93, Roh94] and the PROMICE/WASA experiment [Gre99, G$^+$00].

In both works, precise measurements of the reaction $pd \to pd\pi^0$ in the near threshold region were carried out. The data were compared to predictions from [MN93] that describes the pion production in the dp system by a quasifree process involving the nucleon–nucleon reaction $pn \to d\pi^0$. It turned out that the phenomenological Spectator Model alone failed to describe the experimental distribution over the whole energy range measured and that so–called coherent mechanisms involving all three nucleons had to be added to the model description. Similar result were shown in [Gre99, G$^+$02] for the bremsstrahlung process $dp \to dp\gamma$, which had never been measured before in the given energy range.

The measurement discussed here has been intended to put the results from [G$^+$00, G$^+$02] on firmer ground, since the detector acceptance has not only increased but is sensitive to phase space regions not accessible in the previous experiment. Indeed, the previous results for the Spectator Model contribution are confirmed in this thesis for both reactions. However, limited statistics do not allow an improvement of the previous quantitative conclusions. Apparently, the deuteron beam with an energy of $T_d = 560$ MeV suffered from the beam–target–interaction with the hydrogen pellets, resulting in a rather low deuteron beam life time and large beam heating which caused high background conditions. Furthermore, a simultaneously measured, well–known reaction has not been available for calibration purposes, luminosity determination and estimation of systematic errors.

To address the open questions about the actual performance of the WASA detector, the examination of the second data set is presented. To circumvent the intricatenesses involved with a low energy deuteron beam, data with a high energy proton beam of $T_p = 1.36$ GeV are chosen. The generation and selection of the elastic proton–proton scattering is discussed in detail. The gained data samples are then used to check the efficiency and acceptance of the WASA detector and to diagnose the beam and target performance by determining the vertex position and the luminosity. The calculated vertex position shows a small shift in all three coordinates which is not in agreement with the nominal vertex position within the given errors. The luminosity is determined with a systematical error of less then 5%. In the time period investigated, it increased about a factor of seven, reaching $6 \cdot 10^{30}$ cm^{-2}s^{-1} in December, 2003.

I know of no more encouraging fact
than the unquestionable ability of man
to elevate his life by a conscious endeavor.
— Henry David Thoreau, Walden [Tho92]

Contents

List of Figures

List of Tables

Chapter 1

Introduction

Now it came about that the two great luminaries Signore Giovanni Francesco Sagredo and Signore Filippo Salviati, who had applied themselves methodically to the contemplation of the wonders of God in the heavens and upon the earth in earlier meetings, resolved to meet again to discuss and shed some light on the matters covered in this Thesis. As usual, they met together with Simplicius in the palace of the illustrious Sagredo; and, after the customary but brief exchange of compliments, Salviati commenced as follows[1]

SALVIATI. We shall now turn our wits towards the Thesis laid out here in front of us. To begin our discussion we shall examine the wide field of nuclear physics and, if not discuss in much details the character and efficacy of it, at least reflect upon the phenomena which have been given great heedfulness in the experiment that has been the central subject here. As other experiments in the past decades, CELSIUS/WASA has dedicated itself to shed some light on the still remaining mysteries in nuclear physics, among which the greatest is the description of the nuclear world by the basic theory of the strong force or interaction, that is the QCD, the Quantum Chromo Dynamics.

SIMPLICIUS. Really, to be quite frank, I have the impression that nuclear physics and the questions of the QCD are separate matters and not affiliated with each other. It seems that the world of nuclear physics is governed by a law of nature that should best be called nuclear force, inasmuch as the QCD concerns itself with strange and peculiar phantasms that no one has ever seen nor observed.

SALVIATI. My dear Simplicio, you shall see in a few moments that your objection is without grounds. Truly, the objects at hand, namely hadrons and mesons, are the degrees of freedom observed in the nuclear world and the force between is also identified as the ordering principle in nuclei. However, investigating those corpuscles closer, they appear to be composed of smaller entities, which have been given the name of quarks and gluons. Though never observed as free particles, they neverthe-

[1] This prelude and the dialogue are following closely the style of the "Dialogue Concerning the Two Chief World Systems" by Galileo Galilei [Gal67]. The contents reflects the presentations in [H+04, Nef95, M+92, Höi79].

less are far from being phantasms of a troubled mind. This is a fact that has been proven countless times over and over again. The strong force now mediates between these exotic quarks and since they constitute the hadrons and mesons, it is the very same strong force that must be identified as the underlying fundamental interaction in nuclear physics. In conclusion, the QCD is the fundamental description of all the phenomena involving strongly interacting corpuscles.

SIMPLICIUS. I shall not say that this argument of yours is not conclusive. Still, the QCD cannot be applied to explain the rich variety of phenomena in nuclear physics.

SAGREDO. Perhaps, Salviati, you might consider to reiterate the characteristics of QCD? I can put myself in Simplicios place and see that he is sceptical for a reason.

SALVIATI. I shall do that and in another moment I will give Simplicio satisfaction to explain the difficulties he mentioned. QCD is a quantum field theory of the forementioned quarks, mediated by bosons named gluons. The charge of the QCD is called color, there are three and their specific anti–colors. In contrast to the QED, where the intermediating objects carry no charge themselves, gluons are allowed to do so. The result is a highly nonlinear dynamics in QCD that brings about such features as *confinement* and *asymptotic freedom*. The former means that there is no free color–charged object in nature, the latter means that at high energy scales the interaction between quarks and gluons grows weaker.

SAGREDO. With your last argument you imply that the force grows stronger and stronger when the energy scale diminishes.

SALVIATI. Indeed, I do so. Now the energy scale or temperature here on Earth is much lower than the typical energy of QCD, therefore we encounter quarks and gluons frozen in nucleons, wherein they are bound very vigorously. Even in experiments where one nucleon has collided with another microscopic object, numerous new hadrons or mesons are observed but never a colored corpuscle. The rapidly increasing strength of the force at low energies, the realm of nuclear physics, poses now an unsurmountable challenge, it seems, since it makes it impossible to apply pertubative techniques in theoretical calculations. That is the reason, dear Simplicio, why the application of the QCD in the low energy realm is challenging, to say the least. However, the ingenuity of the human mind is remarkable and several QCD–based predictions are now available in the nonpertubative domain, which give us the hope that with well directed experiments an understanding of the properties of nucleons and their mutual interactions in or outside nuclei can be achieved in terms of the QCD.

SAGREDO. This is all very well but I wonder if we have not strayed from our principal topic, which is this Thesis about certain demonstrations at the CELSIUS/WASA experiment.

SALVIATI. Not so far as you may think, Sagredo, not so far at all. But before I go ahead I shall recount the technical aspects involved in the making of this Thesis, which shall give us an insight on how the wide universe of nuclear physics is explored.

Then, Sagredo, the contiguity with the previously said will become evident. I already mentioned the collision of a nucleon with another object, which may be another nucleon or even a nucleus, whatever fits the experimentators intentions best. Now these scattering experiments, as they are named, play an important role in the experimental method of nuclear physics. The importance is of two sorts. The first is the *production* of new particles, mainly mesons, through the strong force. The second is the observation of the *decays* of the formerly produced. If we turn our attention now closer to the former, it must be noticed that in the last thirty years or so the accelerator based nuclear physics gave access to an extensive amount of experimental data. Especially the developement of facilities that deliver cooled ion beams and have the capability to store these over great periods of time led to remarkable precise measurements of numerous reactions near their kinematical threshold. All these efforts have given us an understanding of the complexities involved in describing the laws of the interaction between hadrons and mesons.

SIMPLICIUS. I have a different opinion on this matter. It seems that the more and more data have been observed and measured, the more the laws of the strong force have shown themselves quite resilient in their withstanding towards any deeper understanding, leaving us mostly phenomenological models.

SALVIATI. Now, now, dear Simplicio, we already discussed the restrictions that are involved if the phenomena in low energy, that is nuclear physics have to be described with the QCD directly. However, the developements in both experimental and theoretical efforts have led to considerable improvements beyond pure phenomenological descriptions. But I agree with you as much that more work is needed to untie this rather difficult knot.

SAGREDO. I guess that you will now explain how both aspects of this field, the production and the decay of mesons come together in the experiment described here.

SALVIATI. You are quite right. The WASA detector, domiciled at the CELSIUS storage ring, was built with the purpose to advance the field of nuclear physics by exploring both aspects. The main aim has been to investigate the decays of mesons, in particular of the η meson. This meson is a rather exotic corpuscle, since its vital statistics make it appear to be massive vacuum. Several of its hypothetical decays would violate basic symmetries like P, C, CP or even CPT. The observation of any such decay could even point to physics beyond the Standard Model.

SAGREDO. Which is the model spanning the whole field of particle physics, is it not?

SALVIATI. Yes, indeed. The identification of some of these decays is rather difficult, though, since their signature can be very similar to more ordinary processes like multiple charged or neutral pion production. So the second aim coincides with production physics, where not only the properties of several production reactions are observed to have a better understanding of the background they impose for the decay physics, but also to push forward the understanding of nonpertubative QCD.

SIMPLICIUS. The Thesis at hand seems not to cover any of the aspects of nuclear physics you have just reviewed.

SALVIATI. On the contrary, my dear Simplicio, though you are right in so far as the decay physics is not addressed. This Thesis has basically two topics. The first explores the feasibility of production physics in deuteron–proton collisions during the commissioning phase of the CELSIUS/WASA experiment. The deuteron–proton system, the former being the simplest nucleus that nature provides, links the elementary production processes in nucleon–nucleon interactions to reactions in a more complex nuclear environment. It has the advantage that its nuclear structure is well known. Moreover, the deuteron provides an elegant way to elude the difficulties involved in producing a neutron target or beam. The second concentrates on the detection system itself, testing and probing its performance and status. A great many aspects have to be investigated carefully before dependable conclusions can be drawn from the measurements at a detection system, notably if it is as complex as the CELSIUS/WASA setup.

SIMPLICIUS. I am not yet convinced by your comments.

SAGREDO. Perhaps we will understand these matters better if we turn our attention to the Thesis here and let it speak for itself. I guess we should start by examining the contents, which is outlined on the very first pages.

Sagredo proceeds to enumerate to contents of the chapters to follow. Soon, the three embark on reading the Thesis silently, so that they can discuss it in its entire depth at a later meeting.

This thesis is organized in the following manner.

Chapter 2 introduces the experimental setup and describes the properties of its components.

Chapter 3 explains the analysis framework that is used to process both simulated Monte Carlo data and experimental data taken with the WASA setup. Both the tools and the procedures necessary to obtain an input for the physics analysis are described.

Chapter 4 outlines the investigations of bremsstrahlung and single pion production in deuteron–proton collisions at a deuteron beam energy of $T_d = 560$ MeV.

Chapter 5 deals with the investigation of the CELSIUS beam and target properties. Data taken with a proton beam of $T_p = 1.36$ GeV are used to select elastic proton–proton scattering. The resulting event samples are applied to determine the vertex position and the luminosity.

Chapter 6 summarizes the results of this work and gives a brief outlook.

Chapter 2

The Experimental Setup

The "The Svedberg[1] Laboratory" (TSL) [TSL98, TSL00, TSL02] was founded in 1986 and operated from 1994 to 2003 as a Swedish national research facility for accelerator–based research. Currently, proposals are being collected for the direction of the future activities at the TSL. It has been decided, though, that the basic research program at the CELSIUS storage ring will end in the fall of 2005.

At the TSL, two accelerators are operated (cf. Fig. 2.1): the Gustav Werner cyclotron and the already mentioned CELSIUS storage and cooler ring. The facility can deliver light ion beams from protons to highly charged Xenon to its users, whose work cover a wide field of activities, ranging from nuclear and hadron physics to biomedicine and proton therapy.

Together with COSY at the Forschungszentrum Jülich, the TSL is the only operating facility focusing on the investigation of the properties and interactions of nucleons and light baryons in the strongly nonpertubative region of QCD by delivering hadronic probes in a storage ring. Hence, it is one of two possible locations for a multi–purpose detection system like the WASA detector for the study of light neutral meson production and their decays.

In the following, first the CELSIUS storage ring is introduced (Sec. 2.1). Then, the Pellet Target is described in Sec. 2.2. Section 2.3 introduces the components of the WASA detector. The chapter closes with Sec. 2.4, where the front-end electronics and the data acquisition system is discussed.

2.1 The CELSIUS Storage Ring

The CELSIUS[2] storage ring has been in operation at the TSL since 1988. Originally, the lattice magnets were used in the Initial Cooling Experiment (ICE, cf. [C+78]) storage ring, which was built at CERN in the late 1970s to test the feasibility to store and cool anti–proton beams. With the CELSIUS ring, the proton energy available

[1] The(odor) Svedberg (1884–1971), professor of physical chemistry at Uppsala University from 1912 to 1949, Nobel Prize laureate in chemistry, 1926.

[2] **C**ooling with **EL**ectrons and **S**toring of **I**ons from the **U**ppsala **S**ynchrotron

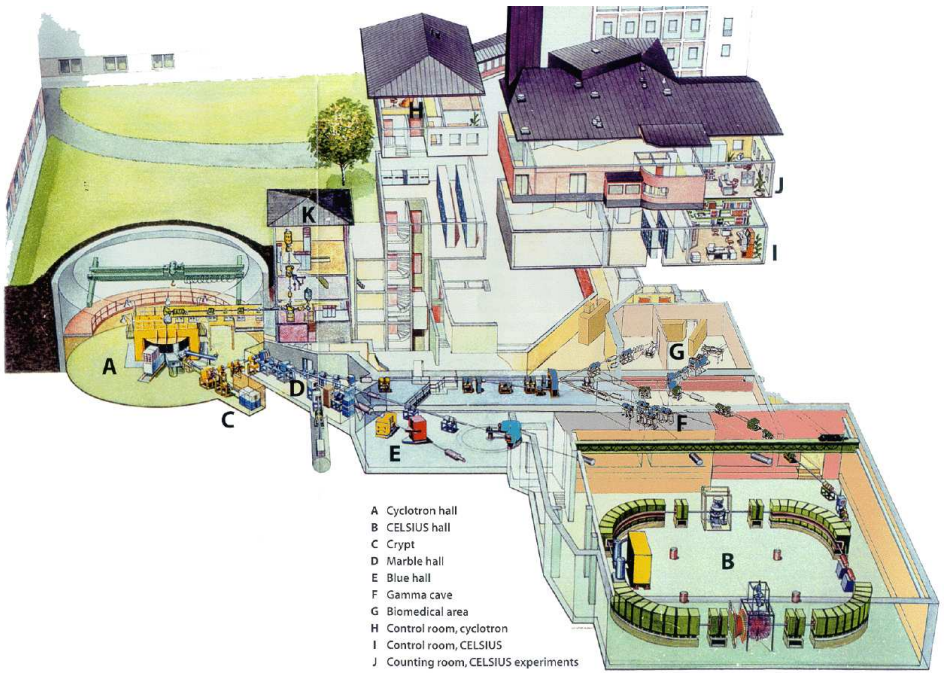

Figure 2.1: *Drawing of the The Svedberg Laboratory (TSL) (from [TSL99]).*

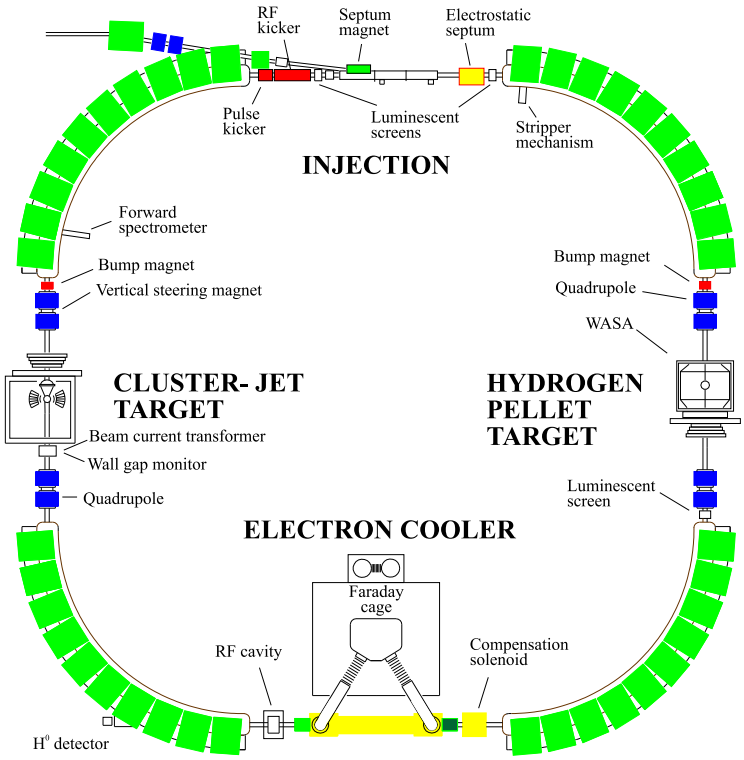

Figure 2.2: *Top view of the CELSIUS storage ring.*

at the TSL was raised well over 1 GeV, making a new field of research available [Kul00].

The ring consists of four quadrants (cf. Fig. 2.2), each with ten dipole magnets and two quadrupole magnets. The four sections contain the injection system (top), the electron cooling system and the RF system for the beam acceleration (bottom), and the two target installations for the experiments: the Cluster–Jet Target, previously utilized by the PROMICE/WASA experiment [C+96], and now used by the CHICSi experiment [CHIC03b, CHIC03a, CHIC04] (left), and the Pellet Target system, where the CELSIUS/WASA experiment is located (right).

The CELSIUS ring operates in cycles. In each cycle, first the molecular ions H_2^+ and D_2^+ are accelerated in the cyclotron and then injected into CELSIUS. During the injection, the molecules pass a 30 $\mu g/cm^2$ carbon stripping foil [B+97] where they loose all their electrons, thus yielding the desired hydrogen or deuterium nuclei.

After filling the ring to its typical capacity (compare Table 2.1), the ions are accelerated up to the chosen kinetic energy and are stored for a certain time. This part of the cycle is called *flat top*. It is the time interval that is used for the experiment, meaning that pellets from the Pellet Target (see Sec. 2.2 below) are injected into the CELSIUS ring and the data acquisition system is activated.

At the end of the flat top, the beam is dumped and the dipole magnets are ramped down to injection level, so that a new cycle can begin. Cycle times can vary from 1 min to 15 min. Some values are listed in Table 2.2. The duty factor listed there is defined as the ratio of the flat top duration to the whole cycle length. It gives the maximum time fraction that can be used for data acquisition.

Circumference	81.8 m
Length of injection and cooling straight sections	9.6 m
Length of diagnostics and target straight sections	9.3 m
Bending radius	7.0 m
Maximum momentum per charge	2.1 GeV/c
Maximum kinetic energy for	
protons	1.36 GeV*
ions with $Q/A = 0.5$	470 MeV/A
Typical number of stored particles for	
protons	1×10^{11}
deuterons	1×10^{10}

* 1.45 GeV since December, 2003

Table 2.1: *Basic parameters of the CELSIUS storage ring.*

beam period	beam	beam energy	cycle length	flat top	duty factor
Nov, 2001	d	560 MeV	100 s	37 s–65 s	28%
Mar, 2003	p	1360 MeV	180 s	55 s–147 s	51%

Table 2.2: *Accelerator parameters for some beam periods.*

2.2 The Pellet Target

The rare decay physics program, which is the main goal of the CELSIUS/WASA experiment, sets high demands on the performance of the target system [E+96]:

- To achieve an almost 4π solid angle coverage in the laboratory system, the target generator has to be placed far away from the interaction point.
- Background considerations rule out the usage of a container for the target, it must be moving through the beam.
- The low branching ratios of the decays of interest require high luminosities of about 10^{32} cm^{-2}s^{-1} or higher, which, in combination with the given beam intensity of the CELSIUS ring, lead to a minimum target thickness of $10^{15} - 10^{16}$ atoms/cm^2. This requirement excludes gas or cluster jet targets.

To comply with these demands, a novel internal target system was developed and commissioned at the TSL [Tro95]. It provides a narrow stream of small frozen ^{1}H (since 2003 also ^{2}H) pellets as a target for the circulating CELSIUS beam.

Figure 2.3 shows a schematic of the Pellet Target system, including secondary systems and the target chamber. The pellets are produced in the pellet generator (top), where a high–purity liquid jet is broken up into uniformly sized and spaced micro–spheres through acoustical excitation. The spheres freeze by evaporation while passing the droplet chamber towards the injection capillary through which they enter into the vacuum chamber. Here, the pellet beam is collimated by the skimmer and travels down the narrow pellet tube to the scattering chamber. After

Pellet diameter	25-35 μm
Pellet frequency	
at jet nozzle	68 kHz
at interaction point	5-12 kHz
Pellet stream divergence	0.04 °
Pellet stream diameter at CELSIUS beam	2-4 mm
Effective target thickness	$> 10^{15}$ cm^{-2}s^{-1}

Table 2.3: *Basic parameters of the Pellet Target System.*

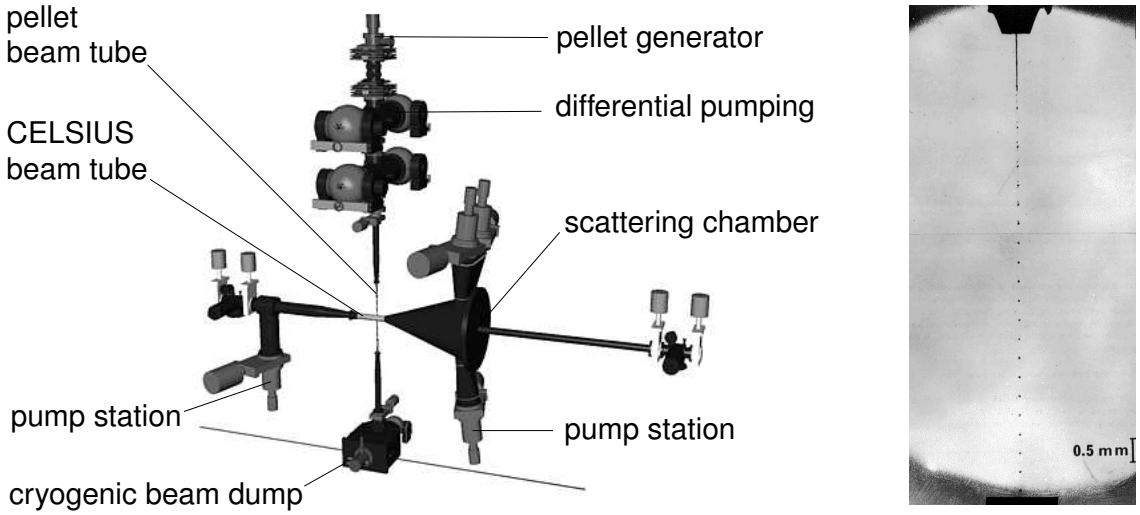

Figure 2.3: *Left: Schematic of the Pellet Target System, including secondary systems like pumps and the target chamber. Right: Photograph of the droplet chamber. The liquid hydrogen jet enters on top through the jet nozzle and is broken up into small droplets, which leave the chamber on the bottom through the vacuum injection capillary.*

crossing the CELSIUS beam, the pellets are collected in the beam dump. Some basic parameters of the Pellet Target are summarized in Table 2.3

2.3 The WASA Detector

The WASA[3] detector was proposed to the Program Advisory Committee of the TSL in 1987 [Kul87]. It was realized in two steps. The first one was the PROMICE[4]/ WASA detector, which successfully took data from 1990–1997. Its main goal was the study of meson production in the proton–proton and the proton–deuteron system. From 1997 to 1999, the PROMICE/WASA setup was rebuilt to the WASA detector, which is shown in a cross section in Fig. 2.4. The main specifications of the WASA detector include

- a large solid angular coverage with sensitivity to both hadrons and mesons and their decay particles like electrons, photons and charged pions,
- measuring the energy and the particle track for all ejectiles,
- the ability to cope with high luminosities of 10^{32} cm^{-2}s^{-1} or more,

[3] **W**ide **A**ngle **S**hower **A**pparatus
[4] **PRO**duction of **M**esons **I**n **CE**lsius

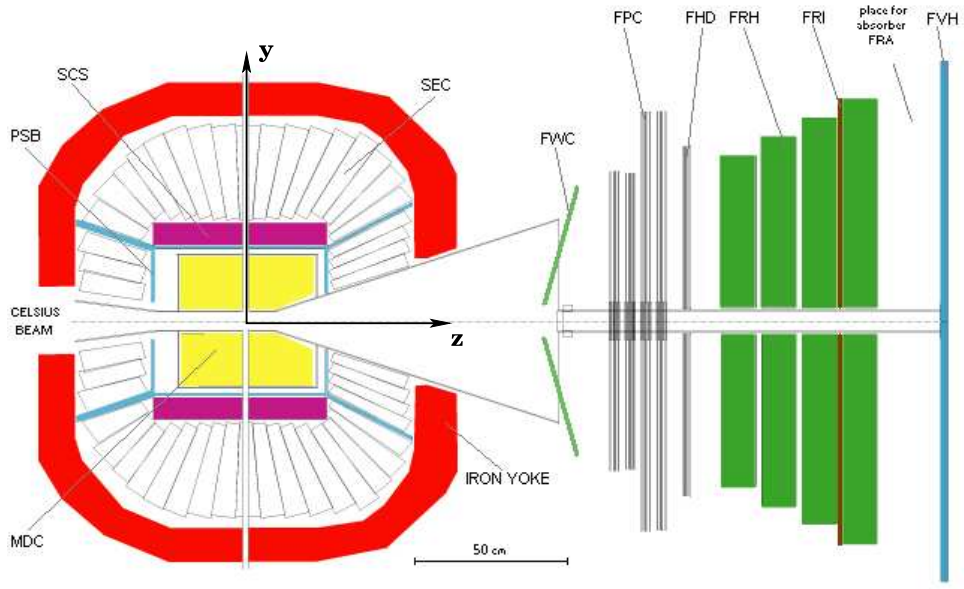

Figure 2.4: *Schematic of the WASA detector setup. The coordinate system is defined by the nominal intersection of the pellet beam with the circulating CELSIUS beam, with y pointing up and z along the CELSIUS beam.*

- insensitive material with low radiation lengths to reduce background contribution from converting particles and to extend the detector sensitivity to lower energies, and
- a highly selective trigger system to gain access to very rare processes.

The WASA detector is composed of two[5] detectors: the Central Detector which surrounds spherically the interaction point and the Forward Detector. Both detectors are designed to fulfill specific tasks:

- The Forward Detector tags the charged target recoil particles and scattered projectiles and measures both their kinetic energy and the spatial coordinates of the particle tracks.
- The Central Detector is optimized for the measurement of mesons and their decay particles. It is sensitive to both charged and neutral particles, giving energy, charge and track position information for each registered ejectile.

The coordinate system used in the analysis is defined by the nominal intersection of the pellet beam with the circulating CELSIUS beam (cf. Fig. 2.4). The z–axis

[5]Actually, there is a third component, the Zero Degree Spectrometer. Since it was not commissioned in the time period covered in this work, the discussion will concentrate on the Forward and Central Detector.

points along the CELSIUS beam, with the y–axis pointing upwards. The x–axis (not shown) points outwards from the CELSIUS ring, completing the coordinate trihedron. Two angles can be defined in this coordinate system; the angle measured towards the z–axis is the polar or scattering angle Θ, the angle in the (x, y)–plane is the azimuth angle Φ.

2.3.1 The Forward Detector – FD

The Forward Detector's role in the whole experimental setup is the detection of the charged particles emerging from the beam–target interaction region. The measurement of the four–vector of each charged particle is desirable. In addition, signals have to be provided for the trigger logic. To cover these tasks, the Forward Detector consists of six subdetectors with dedicated functions.

The Forward Window Counter – FWC

Viewed from the interaction zone, the FWC is the first subdetector of the Forward Detector, placed directly behind the window of the target chamber.

It consists of 12 sector shaped plastic scintillators (BC408) with a thickness of 5 mm. Each element is inclined 10° relative to the plane perpendicular to the beam to follow as close as possible the cone–shape of the target chamber window. The readout is done with photo multipliers (Philips XP2020) connected via light guides (cf. Fig. 2.5). For details please refer to [Mes99].

The FWC signals are used in the first level of the trigger decision. By placing the FWC close to the target chamber window and requiring hits from it, possible background from particles scattering in the beam pipe is reduced.

The Forward Proportional Chamber – FPC

The FPC is the tracking device of the Forward Detector, measuring the track coordinates of a traversing charged particle track.

Of the originally built four modules (cf. Fig. 2.6), only two have been in use in the scope of this work. The two modules, rotated by 90° in the plane perpendicular to the beam with respect to each other, contain four layers of straws, i.e. thin–walled cylindrical drift tubes fabricated from aluminized Mylar foil with a central sense wire. Every second layer is staggered by the radius of a straw thus leaving no gaps in the sensitive area. There are 122 individual straws in each layer. A detailed discussion of the operation mode and the readout electronics can be found in [Dyr97].

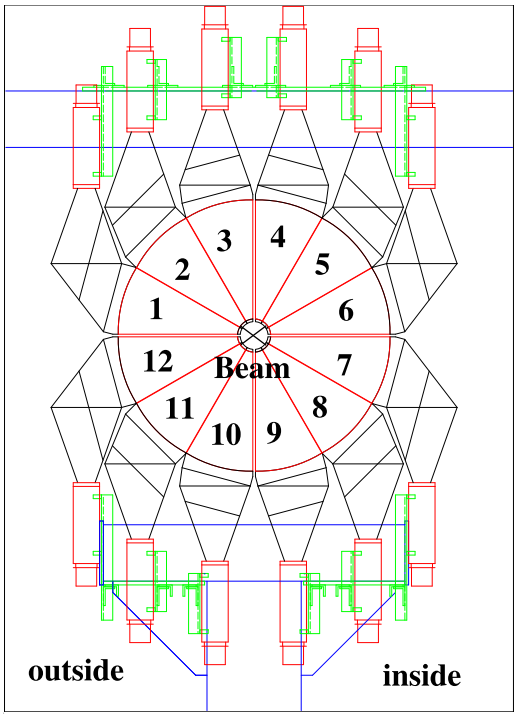

Figure 2.5: *Schematic of the Forward Window Counter.*

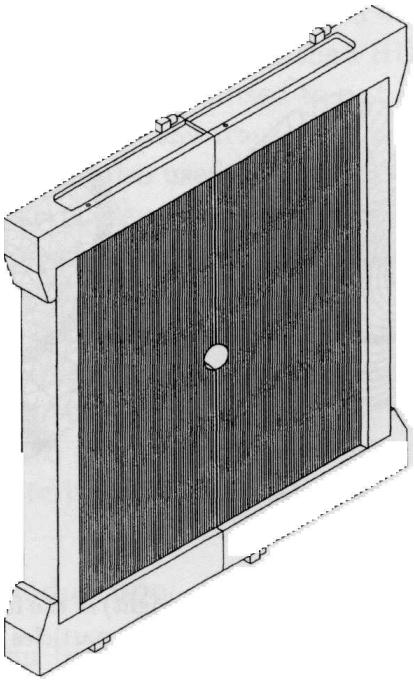

Figure 2.6: *Schematic of one module of the Forward Proportional Chamber.*

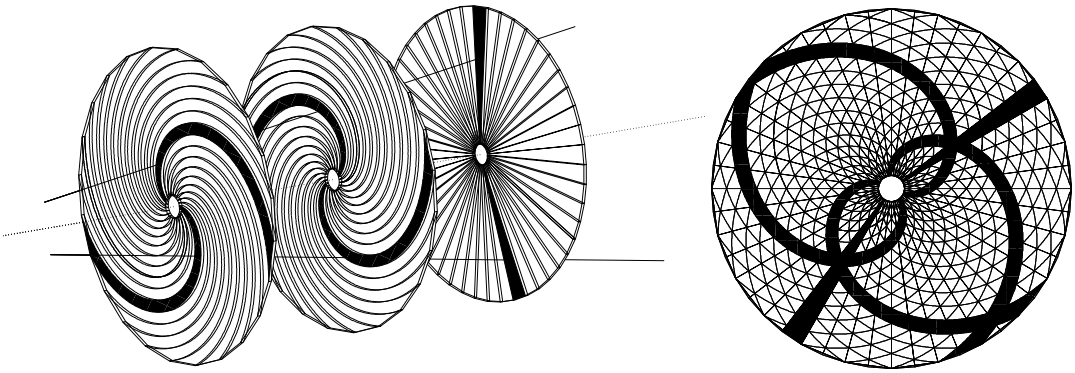

Figure 2.7: *Schematic of the Forward Hodoscope Detector (FHD), shown from the side (left) and front (right). In addition, two charged particle tracks have been plotted to demonstrate the measurement of the punch through coordinates by combining all three layers.*

The Forward Hodoscope – FHD

The next subdetector seen from the beam–target interaction area is the FHD — sometimes also called FTH (Forward Trigger Hodoscope) or FJH (Forward Jülich Hodoscope).

It is made up of three layers of plastic scintillators (BC404). While the 48 elements of the third layer are sector shaped, the 24 elements of the first two layers are spirally shaped, the curvature of the segments following an Archimedes spiral. All elements are 5 mm thick and are read out with Thorn–Emi 9954B photo multipliers.

The FHD provides three sets of information:

- Combining all three layers, two spiral segments and one straight sector form a so–called pixel (cf. Fig. 2.7). These were the means to measure the track coordinates before the commissioning of the FPC. The information is still available and can be used, if desired.

- The energy loss of a charged particle passing through the FHD is recorded for the particle identification via the ΔE–E method and for the reconstruction of the total kinetic energy.

- The third layer is included in the first level trigger decision. The information available covers hit position (azimuth angle) and charged multiplicity.

A comprehensive description of the detector concept of the FHD and similar devices can be found in [D+94].

The Forward Range Hodoscope – FRH

The FRH is the largest component of the Forward Detector. Consisting of four layers of 11 cm thick plastic scintillators (BC400) in the shape of straight 15° sectors, the FRH is oriented in such a way that one of its 24 sectors covers two neighboring elements of the third FHD layer. Light guides provide the optical coupling to the Philips XP2412B photo multipliers. Figure 2.8 shows a schematic of the active material only.

The main purpose of the FRH is the measurement of the kinetic energy of traversing charged particles. The division into four planes provides the energy deposit information used in the particle identification via the ΔE–E method.

Signals for the trigger logic are available from the FRH, giving the azimuth angle and multiplicity information. In the near future, also the usage of the energy information in the trigger is planned.

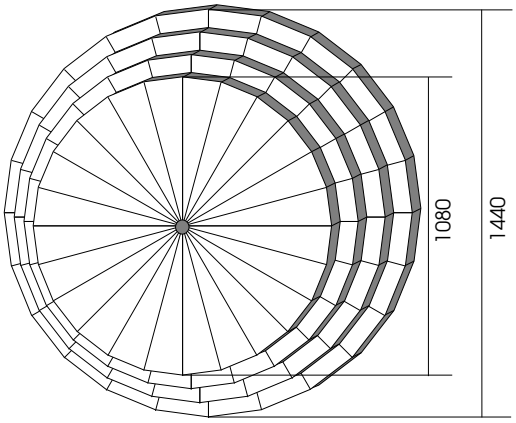

Figure 2.8: *Schematic of the Forward Range Hodoscope with the diameter of the first and last layer given in* mm.

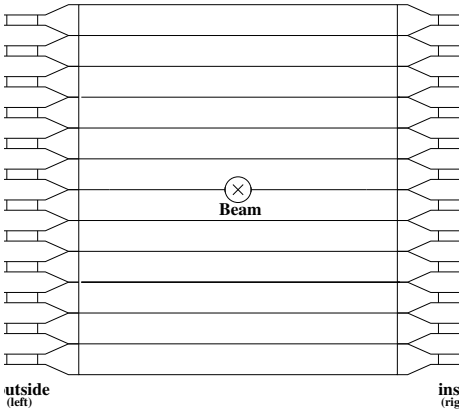

Figure 2.9: *Schematic of the Forward Veto Hodoscope.*

The Forward Veto Hodoscope – FVH

The commissioning of the FVH is described in [Bro95]. It is a single plane of 12 horizontally arranged plastic scintillator bars (BC408) with a thickness of 2 cm and a width of 13.7 cm that are read out at both bar ends with Philips XP2262B photo multipliers.

While the granularity along the vertical line gives the y–coordinate, the x–coordinate is calculated by comparing the readout times at both bar ends and using the known velocity of light in the medium. Thus a two dimensional hit information for each particle is recorded.

The FVH principal task, though, is the discrimination between particles stopping in and escaping the FRH. Since in the latter case, only a fraction of the particle energy is measured, they are treated differently in the software analysis, when the particle's kinetic energy is reconstructed from the deposited energy (cf. Sec. 3.3.7). The discrimination is done in the trigger logic or in the software analysis by requiring particle tracks to have *no* hit in the FVH.

The Forward Range Intermediate Hodoscope – FRI

The FRI Hodoscope is an addition into the Forward Detector setup as it has been described so far. Its purpose is to extent the capabilities of the FRH by adding two-dimensional position sensitivity in conjunction with a fast timing. The extension of the FRH features is motivated by experience with previous projects at PROMICE/WASA, where the poor position resolution and the rather slow timing of the FRH seemed to limit the selectivity for true rare events [Sco01].

One interesting application is the possibility to detect recoil protons from neutrons produced in the beam–target interaction. The efficiency of the FRH for neutrons

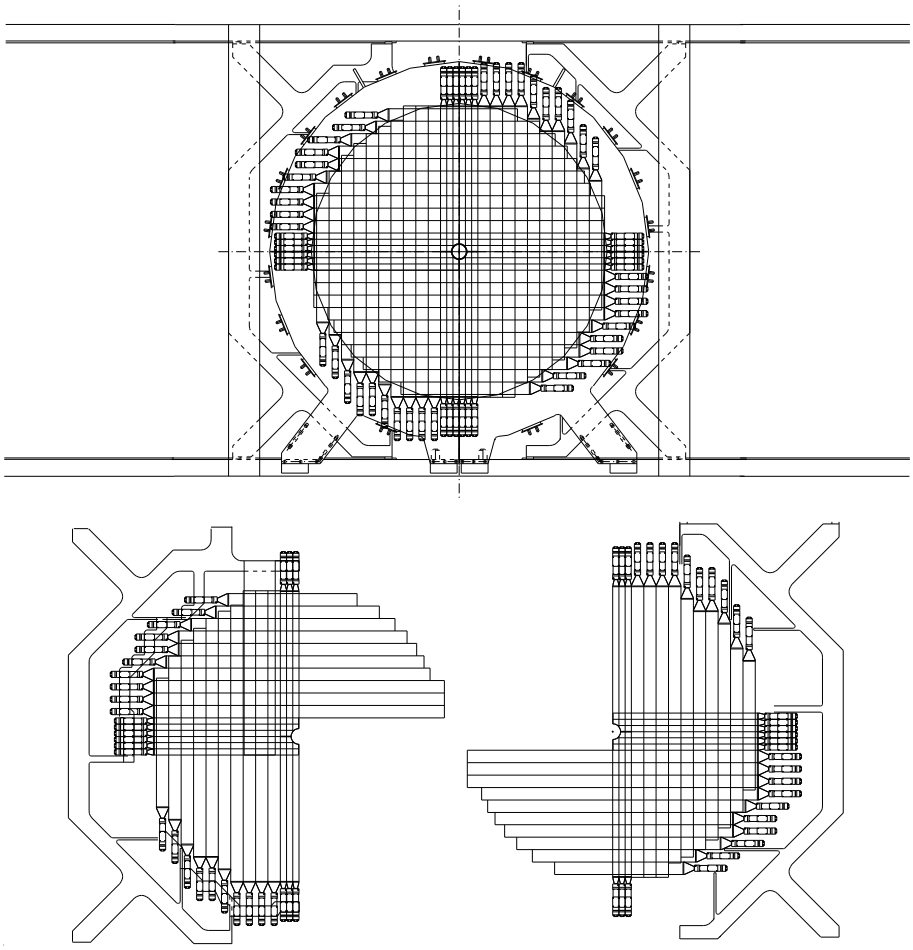

Figure 2.10: *Schematic of the Forward Range Intermediate Hodoscope.*

is in the vicinity of 10%–20%, depending on the neutron energy. With the FRI Hodoscope, the angles of the recoil protons can be measured and probably used to enhance the neutron tagging in the Forward Detector.

The most demanding constraint on the FRI Hodoscope design was its installation location between the third and forth layer of the FRH, a gap not wider than 30 mm. Furthermore, it has to be easily removable to allow for experiments with an undisturbed FRH energy resolution.

The FRI Hodoscope is sketched in Fig. 2.10. It consists of two layers of 32 plastic scintillator bars (BC408) each. They are rotated 90° with respect to each other so that the overlap areas between the bars of both layers form rectangular pixels.

The bars are 5 mm thick and 6 cm or 3 cm wide. The former are placed in the outer rim of the detector while the latter are mounted around the beam pipe hole where the count rates are higher. They are read out on one side with Philips XP1911

photo multipliers optically coupled to the bars by acrylic glass light guides.

The FRI Hodoscope development and commissiong is described in [Pau01, Leh01, Sta03] at length and shall therefore not be repeated here. The feasibility studies concerning the neutron tagging with FRH/FRI are done in [Pau05].

The Forward Range Absorber – FRA

In the first half of 2003, a passive absorber made of iron was inserted between the last layer of the FRH and the FVH. Consisting of several iron sheets, its thickness can be varied from 5 mm up to 10 cm. Furthermore, the absorber is build on rails, making it possible to remove it entirely from the setup.

The absorber in combination with the FVH enhances the tagging efficiency of trigger conditions including the FVH for the η–meson production. This can be explained by the smaller kinetic energy of protons originating from $pp \to pp\eta$ events in contrast to protons coming from the most prominent background reactions like the $2\pi^0$ or $3\pi^0$ production. The former are almost entirely stopped in the FRA while the latter escape more easily the absorber and produce signals in the FVH.

Table 2.4 contains a summary of the main parameters of the Forward Detector.

scattering angle coverage	3°- 18°
scattering angle resolution (tracker)	<0.2°(FWHM)
hit time resolution	<3 ns (FWHM)
amount of sensitive material	50 g/cm^2
radiation lengths	~1
nuclear interaction lengths	~0.6
vacuum chamber window thickness	~2 mm Al
max kinetic energy for stopping (T_{stop}):	
$\pi^{\pm}$	170 MeV
proton, deuteron, alpha	300 / 400 / 900 MeV
energy resolution for stopped particles	~3% FWHM
energy resolution for particles $T_{stop} < T < 2 \times T_{stop}$	4-8% FWHM
particle identification	ΔE-E

Table 2.4: *Basic parameters of the Forward Detector.*

2.3.2 The Central Detector – CD

The Central Detector has the main purpose to detect neutral (photons) and charged particles (electrons and mesons) produced directly or originating from light meson decays. Nevertheless, it can also be used for the detection of charged baryons, e.g. from elastic scattering. It gives the energy, charge and track position information

for each registered ejectile with a large acceptance covering almost the whole solid angle in the laboratory frame.

The signals provided by the Central Detector are used also in the trigger logic, either on the first (fast timing) or second (slow timing) level (cf. Sec. 2.4).

Since the components of the Central Detector are discussed in detail in the works of [Jac04] (Mini Drift Chamber and Plastic Barrel), [Rub99] (Superconducting Solenoid), and [Koc04] (Scintillator Electromagnetic Calorimeter), they are introduced only briefly below.

The Mini Drift Chamber – MDC

Moving from the inside out, the innermost component of the Central Detector, placed directly around the target chamber, is the MDC. Similar to the FPC (cf. Sec. 2.3.1 above), it consists of 1738 straws, i.e. aluminized Mylar tubes with a central sense wire. Each tube is connected to a gas supply and signal cable. The readout electronics include preamplifiers and discriminators.

The straws are arranged in 17 cylindrical layers, with 9 layers being parallel to the beam axis and the other eight having a small skew angle of 6–9° with respect to the beam axis (cf. Fig. 2.11). The two different types of layers are stacked alternatingly to build up the MDC.

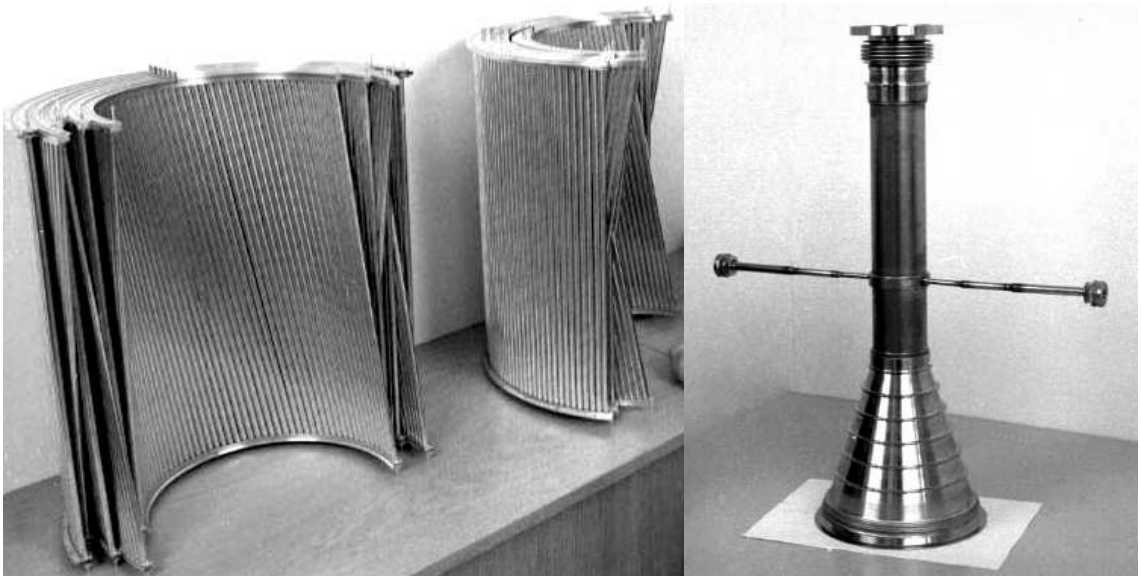

Figure 2.11: *Photograph of the two halves of the MDC prior to installation (left). The layers consisting of the drift tubes are shown. The MDC is installed around the target chamber (right) made out of Beryllium. The thin horizontal pipes are the lead–through for the target pellets.*

The MDC provides high accuracy tracking information for charged particles and is the main apparatus for the vertex determination, either alone or in combination with the FPC.

The Plastic Scintillator Barrel – PS

The PS is a barrel made of plastic scintillators (BC408) surrounding the MDC. It is divided in three subsections, called forward (PSF), central (PSC), and backward (PSB) (cf. Fig. 2.12). There are 48 straight sectors in both the PSF and the PSB, while the PSC contains 50 bars, since the one on the top and the bottom are split to let through the pellet tube. All 146 segments are 8 mm thick and cover 15° in the azimuth angle. They are coupled with acrylic light guides to FEU–115M photo multipliers.

The PS is the Central Detector counterpart to the FHD, fulfilling a multitude of tasks:

- It provides fast timing signals for trigger purposes.
- It gives energy loss information of charged particles for particle identification via ΔE–E (with the SE) or ΔE–p (in combination with the MDC) method.
- It allows the discrimination of charged and neutral particles either in the offline reconstruction or in the trigger decision.

The Superconducting Solenoid – SCS

The next component of the Central Detector, the SCS, is an ultra–thin walled superconducting solenoid magnet that provides a central axial field of up to 1.3 T that serves

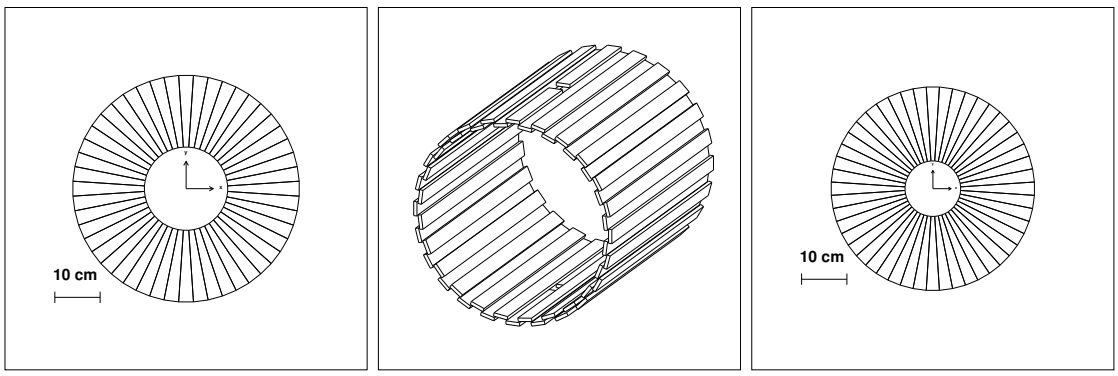

Figure 2.12: *Schematic of the forward, central and backward parts (from left to right) of the PS.*

- the measurement of the charged particle momenta in the MDC and
- the protection of the Central Detector against low–energy delta electrons that are produced in the beam–target–interaction.

Placed inside the Calorimeter, the SCS has an optimized wall thickness as small as 0.18 radiation lengths, thus minimizing the probability of electromagnetic showers in its walls and maintaining an accurate energy measurement in the SE.

The solenoid is cooled down to 4.5°K by a small helium refrigerator. The field of 1.3 T, obtained with a current of 875 A, is confined by a yoke made out of 5 t of pure iron with a very low carbon content. The yoke also shields the SE photo multipliers and readout electronics from the magnetic flux and serves as a support for the SE crystals.

The Scintillator Electromagnetic Calorimeter – SE

The outmost layer of the Central Detector "onion" is the Electromagnetic Calorimeter (SE). It consists of 1012 sodium–doped CsI scintillating crystals arranged in three sections: a forward part (SEF), a central part (SEC), and a backward part (SEB), which can be seen in Fig. 2.13. The crystals in each part differ in shape and size as sketched in Fig. 2.14. The gaps between the three parts of the SE contain the light guides of the PS.

The crystals are read out with FEU-84-3 photo multipliers in the SEB and SEF, while the forward part is equipped with Hamamatsu R1924 photo multipliers due to their smaller size and the limited space in the forward cap of the SE. All photo multipliers are placed outside the iron yoke and connected to the crystals inside by 20–30 cm long plexiglass light guides.

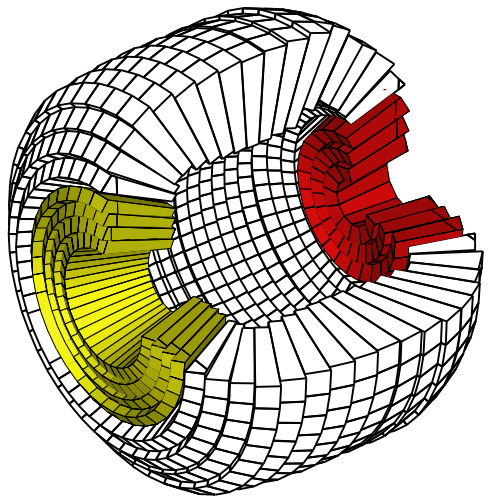

Figure 2.13: *Schematic of the Scintillating Electromagnetic Calorimeter. The marked regions on the left and right correspond to the forward and the backward part, respectively, with the central part in between.*

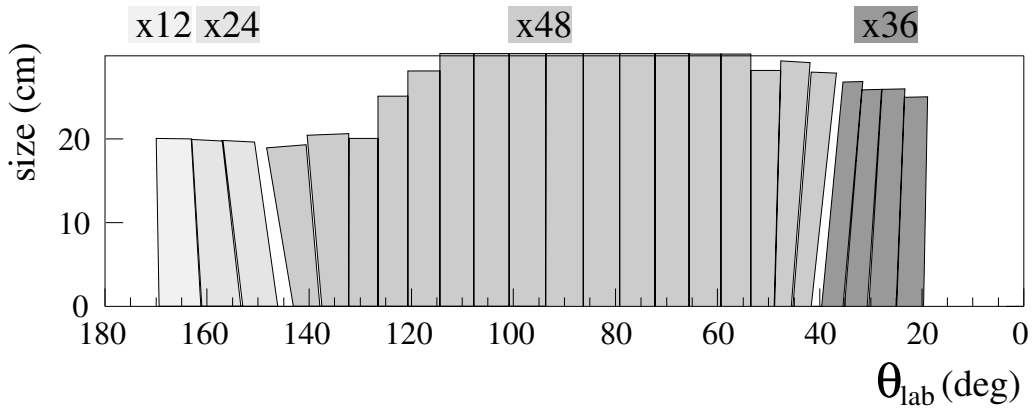

Figure 2.14: *Coverage of the polar angle by the Electromagnetic Calorimeter. The shape and size of the CsI crystals for the backward (first three layers from the left), the forward (first four layers from the right), and the central part are shown. The figures on the top indicate the number of elements found in the respective layer.*

amount of sensitive material (SE)	135 g/cm^2
radiation lengths	~16
nuclear interaction lengths	~0.8
geometric coverage:	96%×4π steradians
in scattering angle	~ 20–169°
in azimuthal angle	~ 0–180°
max kinetic energy for stopping	
$\pi^{\pm}$/proton/deuteron	190/400/450 MeV
scattering angle resolution	
charged / neutral	~ 1.2° / ~ 5° (FWHM)
hit time resolution	
charged particles	<3 ns (FWHM)
photons	~ 40 ns (FWHM)
relative energy resolution (SE)	
photons (100 MeV)	~ 8% (FWHM)
charged particles	~ 3% (FWHM)
particle identification via ΔE-E or ΔE-p	
measurement of π^0 and η mesons by γγ decay:	
energy resolution π^0/η	10% / 20% (FWHM)
angular resolution π^0/η	7° / 7° (FWHM)

Table 2.5: *Basic parameters of the Central Detector.*

The SE measures the kinetic energy of charged and neutral particles alike. The information is also available to the data acquisition system to enhance the selectivity of the trigger.

Table 2.4 contains a summary of the main parameters of the Central Detector.

2.3.3 Differences between PROMICE/WASA and WASA

Though some detector components listed above have been part of the previous PROMICE/WASA detector setup, the rebuilding into the WASA setup changed the overall detector properties significantly:

- the Forward Detector has been moved closer towards the interaction point, changing the scattering angle coverage from $4-22°$ to $3-18°$. Changes in the FWC and additions like FRI or FRA have enhanced the selectivity of the trigger conditions.

- the Central Detector replaced the two crystal arrays, changing both the azimuthal coverage (from 100° to 360°) and the covered scattering angle (from $30-90°$ to $20-169°$.

- the Pellet Target system increased the target density by about a factor of 20 from $1.3 \cdot 10^{14}$ atoms/cm^2 to $5 \cdot 10^{15}$ atoms/cm^2.

Besides the changes in the detector setup, the whole data acquisition system has been subjected to large modifications. This will be the topic of the next section.

2.4 The Data Acquisition System – DAQ

All of the WASA detector components described in the preceding Sec. 2.3 are connected to a setup of dedicated hardware and software called the data acquisition system (DAQ), which is described in depth in [Mar01]. It handles the readout, processing, and storage of the detector signals. A schematical diagram of the DAQ is shown in Fig. 2.15. Basically three components can be distinguished: the front-end electronics, the trigger system, and the event building and monitoring, all of which will be described below.

Another important component of the experimental setup is the so–called slow control. It is used for the steering of configuration parameters like high voltage settings, discriminator thresholds, or trigger setup. Partly, it is realized by integration into the TSL accelerator control system. Other susbsystems rely on proprietary solutions.

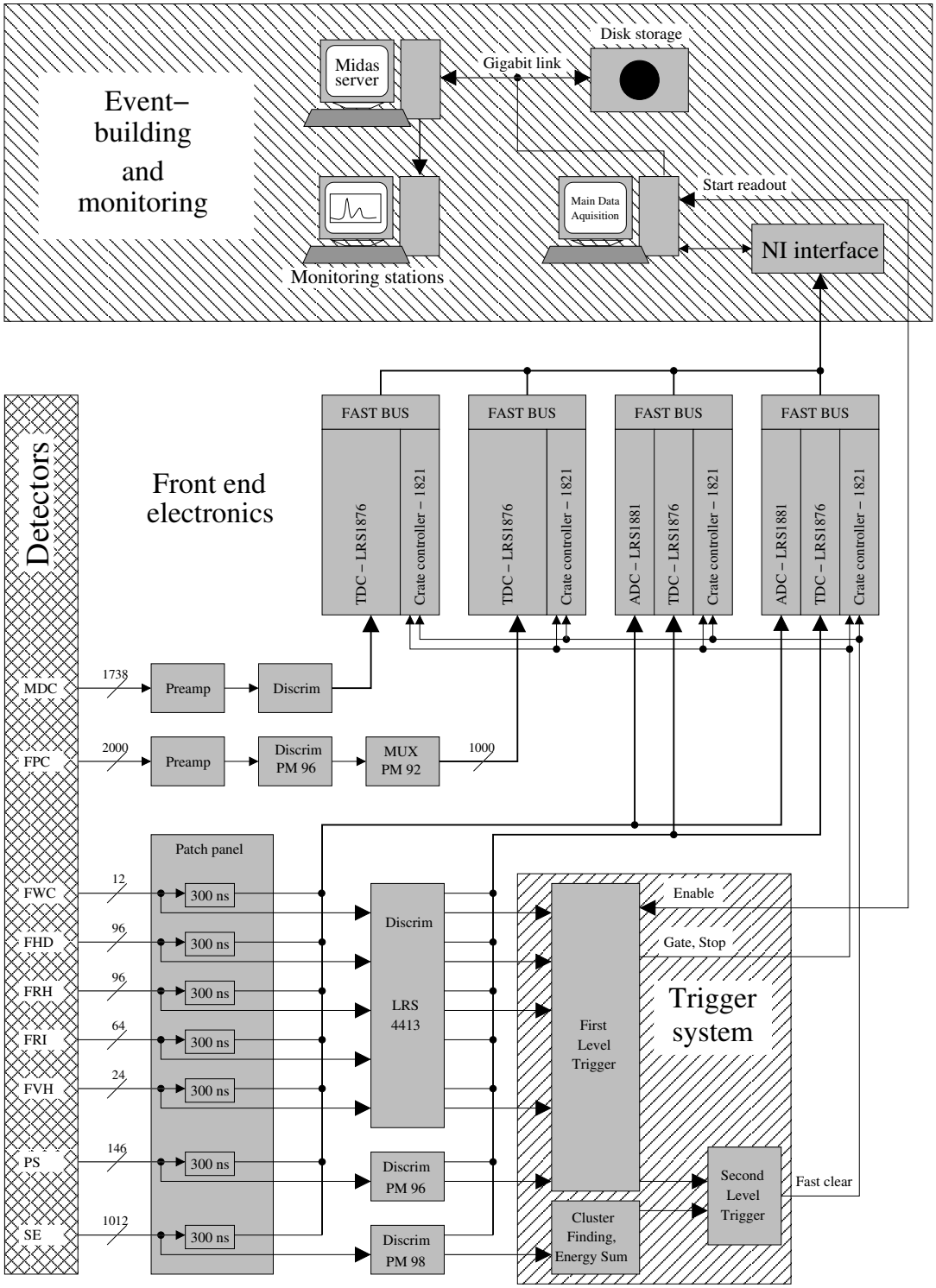

Figure 2.15: *Schematic of the data acquisition system.*

2.4.1 Front-End Electronics

All analog signals from the scintillating detectors (approx. 1500 channels) are transmitted from the experimental hall to the electronics hut via coaxial cables (RG58). Here, the signals are split into two branches in dedicated splitter–delay boxes (cf. Fig. 2.15, "Patch panel" in the lower half, left).

One branch is delayed by 300 ns via passive delay line circuits and then fed into charge sensitive Fastbus Analog–To–Digital Converters (QDC's) of the type LRS1881. Dynamic range matching of the signal is done via so–called paddle cards equipped with passive damping and impedance matching circuits.

The other branch is connected to discriminators of the type LRS4413 (CAMAC modules, all Forward Detector signals) or PM 96/98 (Euro crate modules, PS/SE signals). After discrimination, the signals are once more split, with one branch being used as input for the trigger system, which is described below. The other branch is connected to Fastbus Time–to–Digital Converters (TDC's) of the type LRS1876 that are capable of recording multiple hits per channel.

The signals from the two straw chambers (approx. 3000 channels after multiplexing the FPC signals) are treated differently. Having their front-end electronics down in the experimental hall, already discriminated signals are transmitted to the electronics hut via twisted pair cables. There, all signals are connected directly to Fastbus TDC's.

All Fastbus digitizers are controlled by the trigger system. For a valid event, control signals are sent to the QDC's and TDC's to start the signal conversion. Two QDC gate signals are generated, a short one of 150 ns for the fast plastic scintillators and a long one of 1 μs for the CsI crystals. The TDC's are operated in the so–called common stop mode where the individual hit signals mark the start of the time interval and the stop signal comes from the trigger system. The modules can also be reset by a fast clear signal if the second level trigger discards the event.

When the modules have finished converting the signals, the digitized data are transferred to the main data acquisition, a commercial PC running a real time Linux, via a PCI interface connected to the LRS1821 Fastbus crate controllers.

Data sheets for some of the LeCroy (LRS) modules mentioned above can be found on the web [LeC01]. All PM modules were designed and developed in [Mar01].

2.4.2 The Trigger System

For the design luminosity of 10^{32} cm^{-2}s^{-1} in the WASA experiment, the reaction rate amounts to several MHz. Since not all reactions that occur are of interest for the WASA physics program and the maximum readout rate of the DAQ is less than 1.5 kHz, it is necessary to apply a filter of some sorts to reduce the input rate by three orders of magnitude while retaining as much of the interesting reactions as possible.

The trigger system consists of a set of dedicated hardware modules developed at the TSL. They have replaced the NIM and CAMAC based trigger logic from the PROMICE/WASA setup, making the configuration and maintenance of the trigger system easier and more flexible.

The discriminated signals from the scintillation detectors serve as input signals. They are grouped into two sets of fast and slow triggers.

In the fast trigger branch signals from the plastic scintillator hodoscopes are processed. As shown in Fig. 2.16, this means first counting the cluster multiplicity per detector plane by merging hits in adjacent detector segments to a cluster. Then, the track alignment is checked by combining clusters in FWC, FHD, and FRH that overlap geometrically. Additionally, the veto conditions set on PS or FVH are tested.

These multiplicity, alignment, and veto signals are now either fed into the *first level trigger* branch or they are treated as pretriggers for the second level trigger. Either way, they are combined into more complex trigger conditions after delay matching and shaping. The trigger combining logic uses five coincidence matrices that can handle up to 48 input signals and produce eight output signals each. These are prescaled, if necessary, to balance out the net trigger rate, and connected to the trigger mask and selection unit. Here, the incoming 40 bit pattern is compared to a mask that selects active triggers.

The processing time for the first level trigger is around 200 ns which does only allow to test simple analytical and logical expressions. Therefore, a *second level trigger* is implemented that has a larger time window of up to 500 ns. This scheme ensures a low dead time while achieving a high selectivity.

The second level trigger uses the signals from the SE as input signals. In two dedicated systems, both the counting and forming of the SE cluster multiplicity and the SE total energy sum is calculated (cf. [Mar01]). Both signals are delay matched with the pretrigger signals from the fast branch and combined in the coincidence matrices described above. Prescaling and trigger selection works analogous to the first level trigger.

The next steps after a valid trigger signal is generated depend on the trigger signal type:

- If a valid first level trigger is present, the synchronization and gate generation unit produces the gate and stop signals for the QDC's and TDC's, respectively. Furthermore, the production of a fast clear signal is inhibited.

- The synchronization and gate generation unit is also activated if a pretrigger signal is set. In this case, however, also a fast clear signal is generated. The trigger system now waits for the second level trigger logic. If a valid second level trigger pattern is found, the fast clear signal is inhibited and the event recorded. If not, the fast clear signal resets the Fastbus digitizers, discarding the current data. This takes about 3 µs.

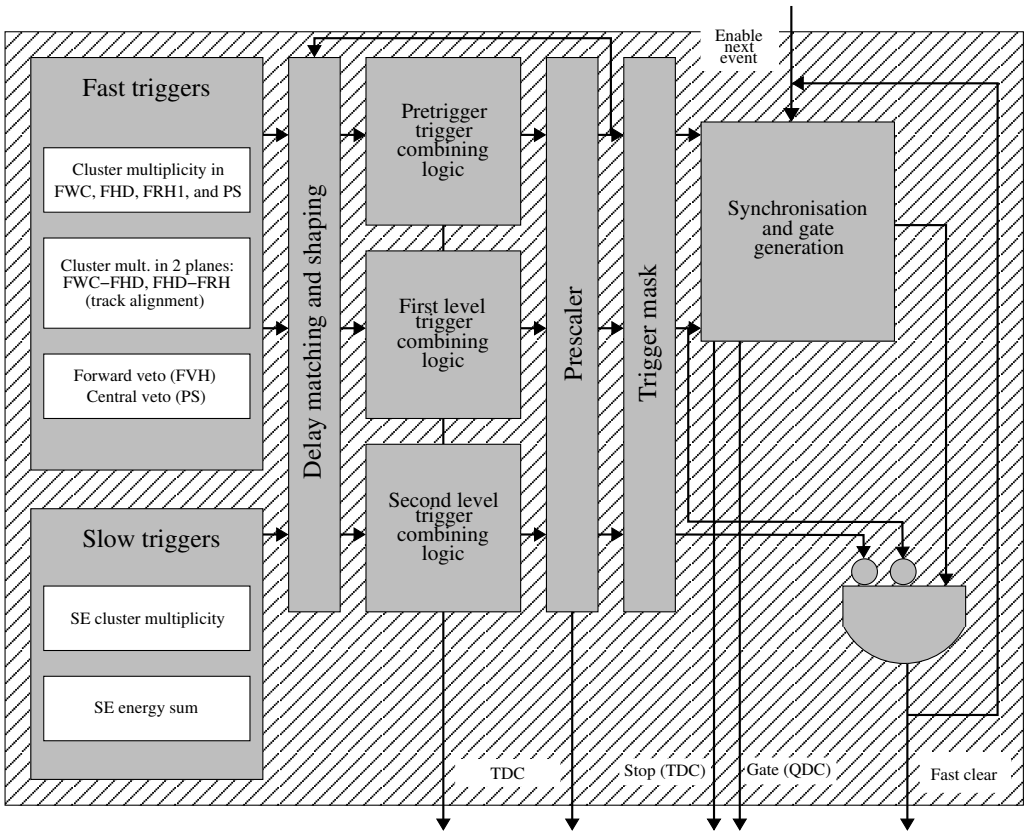

Figure 2.16: *Schematic of the WASA trigger system (from [Fra04]).*

Beside the control signals for the front-end electronics, also the generated trigger signals are output to be recorded in Fastbus TDC's. This information is used later in the offline analysis to determine which condition actually triggered a certain event. Furthermore, all trigger signals are counted in two independent scaler systems, based on the Fastbus and VME standard, respectively. The scaler rates are used for online monitoring and for offline analysis for checks of the trigger system or dead time calculation and correction.

2.4.3 Event Building and Monitoring

If a trigger signal is set, the four Fastbus crates digitize the input signals and send their data sequentially via a 16–bit data link to an interface in the main data acquisition computer.

The computer is responsible for the so–called event building and logging. The information from the Fastbus crates and modules is formatted, an additional header is added, and the event is stored in a large disk storage array that is connected via a Gigabit LAN interface. With a typical readout rate of 800 Hz and an event

size of 3 kB, about 2.4 MB are written to disk per second. While the DAQ is busy recording the actual event, the generation of further gate or stop signals is inhibited by the main data acquisition computer.

The Monitoring stations are running a collection of tools which give basic information on the experiment status. Through MIDAS[6], developed and used at PSI [MID01] and TRIUMF, web based history plots of the trigger rate changes are provided. The ODIN and the WASALIB program packages deliver online analysis by reading data from the disk storage array.

[6] **M**aximum **I**ntegration **D**ata **A**cquisition **S**ystem

Chapter 3

The Analysis Tools

This chapter deals with the analysis framework that is used to process experimental data taken with the CELSIUS/WASA setup. Basic procedures for raw data processing like the energy calibration are described here as well as higher level reconstruction methods.

For most studies of the detector setup, e.g. the energy calibration, experimental data have to be compared to a data sample that expresses the experimentalist's expectation of the detector performance. In particle physics such a data sample is produced by simulating the detector response to incident particles via Monte Carlo techniques.

Throughout this chapter the importance of identical treatment of experimental data taken with the WASA detector and simulated data generated with a Monte Carlo simulation will be stressed. Such a treatment ensures that the corrections for limitations of the detector system concerning resolution, acceptance and efficiency can be deduced and applied to experimental data.

To provide a framework of suitable tools several program packages have been written for the offline analysis of the CELSIUS/WASA experiment. Table 3.1 contains the most prominent ones.

Name	Language	Operating System	Ref.
WASALIB: the WASA program library	F77	Unix, GNU/Linux	[CK00]
ODIN: Online/offline Data Inspection Program	F77	Windows	[Zło03]
CWlib event reconstruction and analysis library	C++	Unix, GNU/Linux	[Kup02]
CWanalysis	C++	Unix, GNU/Linux	[Pät02]

Table 3.1: *Offline analysis tools for the CELSIUS/WASA experiment.*

Since only the WASALIB package was used in this work, the detailed discussion below is restricted to that program library. The chart in Fig. 3.1 shows the logical

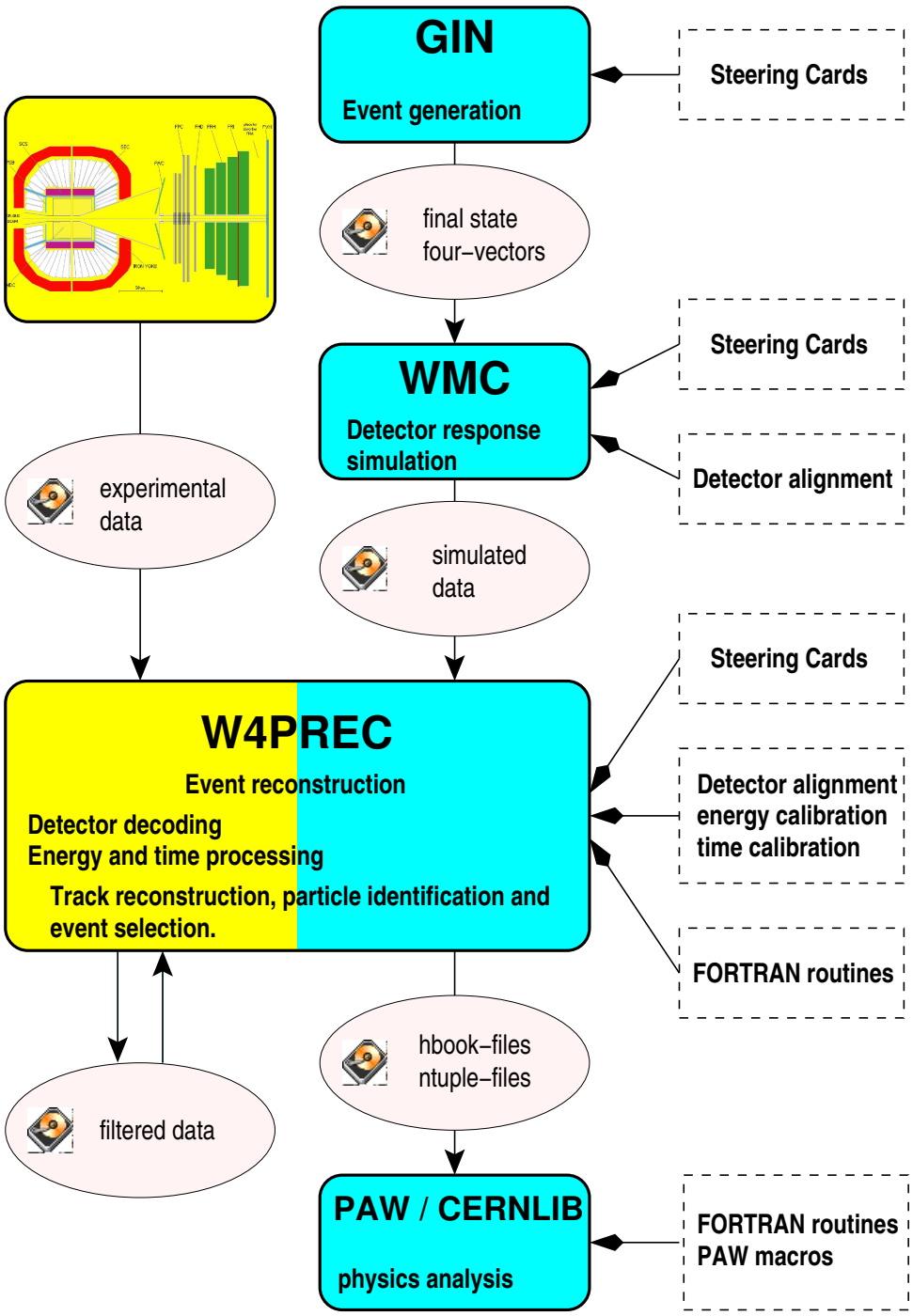

Figure 3.1: *Flow chart of the WASA offline analysis program package. Either experimental or simulated data are fed into the reconstruction program to select events for further analysis. The user manipulates the data flow by changing the information symbolized by the dashed boxes.*

layout of the application flow.

The following remarks will first cover the preparation of a Monte Carlo data sample which is a two step process. In Sec. 3.1, the production of a set of final states with an event generator is described. This set serves as an input for a detector simulation, which outputs the simulated detector response to the incident final state particles (Sec. 3.2). The outline of the reconstruction tool for both experimental and simulated data is discussed second in Sec. 3.3. The physics analysis will not be addressed here but rather in the following Chaps. 4 and 5.

3.1 The Phase Space Monte Carlo Event Generator – GIN

Generating an event in a specific channel originating from a pp or dp reaction means to produce a set of N final state four–vectors $P_i = (E_i, \vec{p}_i)$, $i = 1, \ldots, N$ with $E_i^2 = \vec{p}_i^{\,2} + m_i^2$. The total cross section in this channel can be written as (cf. [PDG04, BK73])

$$\sigma = \frac{1}{F} \int |M|^2 \, d\Phi_n(P_a + P_b; P_1, \ldots, P_N), \tag{3.1}$$

where P_a and P_b denote the projectile and target four–vectors respectively and $F = 4 m_b |\vec{p}_a| \, (2\pi)^{-4}$ the flux factor. Equation 3.1 can be derived directly from Fermi's Golden Rule (cf. [Gri87] and citations therein). It shows that the phenomenological description of the reaction properties can be roughly split into two parts, one of them describing the dynamical and the other the kinematical and statistical aspects [Hag63]:

- The term $d\Phi_n(P_a + P_b; P_1, \ldots, P_N)$ expresses both the *kinematical* and *statistical* properties of the reaction. The former refers to the energy and momentum conservation while the latter relates to the density of states:

$$d\Phi_n = \underbrace{\delta^4 \left(P_{tot} - \sum_{i=1}^{N} P_i \right)}_{\text{(energy and momentum conservation)}} \underbrace{\prod_{i=1}^{N} \frac{d^3 P_i}{(2\pi)^3 \, 2E_i}}_{\text{(density of states)}}, \tag{3.2}$$

  with $P_{tot} = P_a + P_b$. Since Eq. 3.2 defines which states are accessible, it defines a kinematically allowed $3N - 4$ dimensional region in the momentum space called phase space. Hence, Eq. 3.2 is also referred to as phase space factor.

- The *dynamical* aspect is contained in the other term, the matrix element $|M|^2$. It gives the transition probability from the initial state Ψ_i to the final state Ψ_f via the transition operator T:

$$|M|^2 = |\langle \Psi_f(P_1, \ldots, P_N) | T | \Psi_i(P_a, P_b) \rangle|^2. \tag{3.3}$$

Before the integration in Eq. 3.1 can be carried out, $|M|^2$ needs to be defined. If the reaction dynamics is known or described by a model, it can be taken into account during the event generation process by an appropriate definition of $|M|^2$, e.g. as final state interaction (FSI). However, for several reactions such definitions are not available. In that case, a constant $|M|^2$ is set per default during the event generation, thus producing a distribution with constant density. This kind of distribution is usually referred to as phase space distribution and the integration in Eq. 3.1 gives the phase space volume R_N:

$$R_N = \int \delta^4 \left(P_{tot} - \sum_{i=1}^{N} P_i \right) \prod_{i=1}^{N} \frac{d^3 P_i}{(2\pi)^3 \, 2E_i}. \tag{3.4}$$

The event generator used in the WASA program library is called GIN (**G**EANT **In**put). It employs Monte Carlo techniques to integrate over phase space and is based upon the FOWL [Jam77] program from the CERN program library (CERNLIB, [CER93a]). Besides its primary function as an event generator it can also be used to make fast detector acceptance studies by defining geometrical cuts on the generated event sample. Furthermore, it offers the possibility of simulating effects like limited detector resolution by defining energy smearing parameters.

Without a definition of any reaction dynamics (this is the default), FOWL calculates the kinematical weight per generated event according to Eq. 3.2. Though the kinematical weight is not necessarily a constant, the resulting distribution in phase space has a constant density.

If reaction dynamics are included, GIN treats $|M|^2$ as an additional "weight" function by multiplying the kinematical weight factor of each event accordingly. Throughout the whole analysis chain — detector simulation and event reconstruction — this weight has to be considered when histograms are filled.

For an in depth study on the subject of the implementation of a Monte Carlo phase space generator the reader is referred to [Jam68].

3.2 The Full Detector Simulation – WMC

The detector simulation included in the WASA program library is called WMC (**W**ASA **M**onte **C**arlo). It is a GEANT (**Ge**ometry **a**nd **T**racking, cf. [CER93b]) based program package that uses Monte Carlo techniques to simulate the detector response to incident particles.

The incident particles are read in from a GIN file. The reaction vertex is determined and the incident particles are tracked through the detector material in small steps. For each step, all possible reactions with the surrounding material are simulated according to their respective probability. If a reaction occurs, the effects are calculated and the particle energy and direction is adjusted accordingly. The

procedure is repeated until all particles have either left the detector volume or are "lost" by decay or absorption (cf. Fig. 3.2 for a single Monte Carlo event).

The main prerequisite for a working simulation is a complete description of the detector in the GEANT language. It defines the shape and material of all active detector elements, e.g. scintillators, as well as all passive ones like the beam pipe, flanges or packaging material. Furthermore, parameterizations of cross sections for all possible reactions in these materials are needed. Included reactions in GEANT cover energy losses, angular straggling, particle decays, and a variety of secondary reactions.

The resulting data set is similar to an experimental data set. For each event the deposited energies and hit times in each element are stored. The data format is the same as used for experimental data and therefore readable by the reconstruction program.

The original four–vectors of the generated particles are also written to the WMC output. The comparison of the original energies and directions of the incident particles with their reconstructed values yields both the efficiency and the resolution of the reconstruction routines.

3.3 Event Reconstruction – W4PREC

The WASA program library provides the W4PREC (**W**ASA **4π Rec**onstruction) tool for experimental or simulated data processing. It has been derived from the PROMICE/WASA program package PWREC to include the handling of the extended 4π detector setup of the CELSIUS/WASA experiment.

W4PREC handles input from various sources like hard disks or magnetic tapes. It outputs either histograms or Ntuples to be used with physics analysis packages like PAW (**P**hysics **A**nalysis **W**orkstation, [CER99]) or ROOT, or filtered data in the raw data format for further processing in custom analysis tools like the C++ tool package.

The reconstruction program is steered and configured with so–called data cards. These cards implement the detector decoding, matching hardware addresses to software coding, calibration and alignment information and user options for applying conditions on the reconstruction process. Furthermore, users can add or change the processing code itself, thus adjusting the program to their needs.

For certain reconstruction steps it is necessary to distinguish between experimental and simulated data, e.g. energy calibration constants have in general no meaning in Monte Carlo data sets. This is taken care of by the DAQ event builder and WMC program which assign different record types to the written data files.

The data processing in the W4PREC program is described step–by–step below.

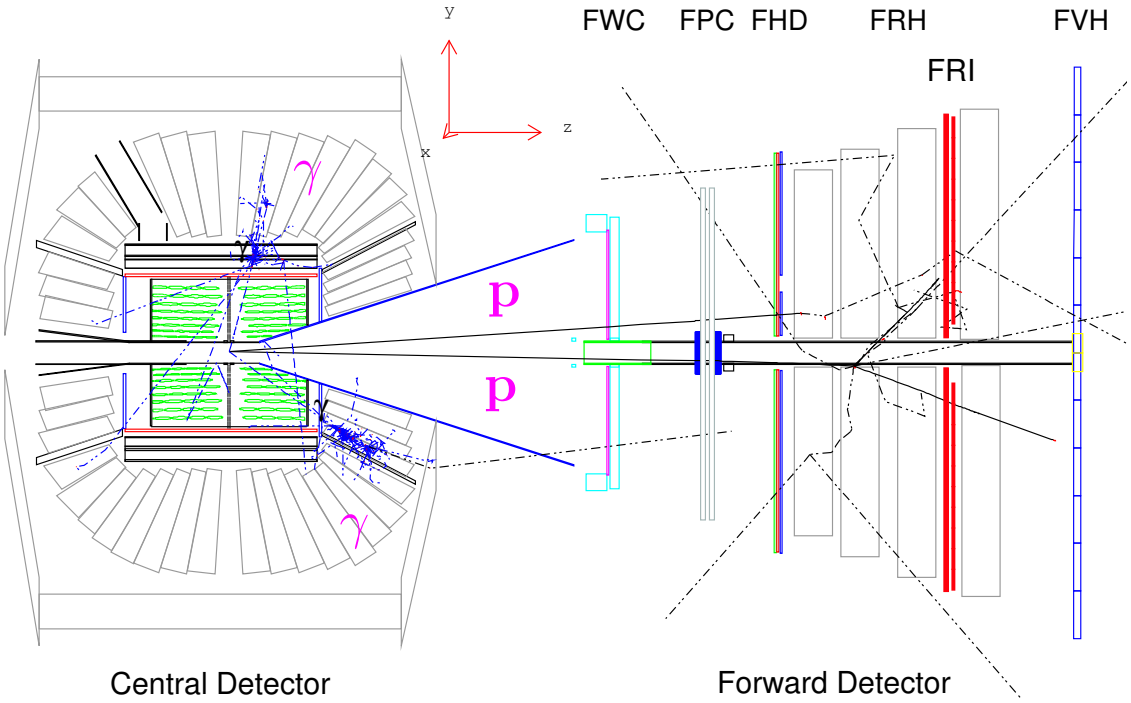

Figure 3.2: *The WASA detector as described in the detector simulation. A* $pp \to pp\eta$ *event is shown with two protons (thick black lines) stopped in the Forward Detector and two photons from* $\eta \to \gamma\gamma$ *decay showering in the Central Detector.*

3.3.1 Decoding

Each WASA detector element is either read out through a TDC, or a QDC, or both (compare Chap. 2). Each readout channel has a hardware address, defined by the location of the FASTBUS module. This hardware address, given in crate, slot, and channel number has to be translated to a software address, defined by detector, plane, and element number. This is called decoding and is the first step in the event reconstruction. After decoding, the information for each detector element hit is sorted into the so–called Hit Bank for further processing.

The detector decoding also covers the handling of all available general information on the event, e.g. scaler rates, trigger TDC's set, accelerator time, or beam current. This data are stored in Special Blocks and can be accessed throughout the following reconstruction process. One application is to set selection conditions on these general information to get rid of unwanted events in a very early stage of the reconstruction process to save time. For example, one might choose to consider only events that occurred in a certain time window during the accelerator cycle.

3.3.2 Energy Calibration in the Forward Detector

After decoding the experimental data one obtains a set of QDC and TDC values for each detector element hit. These values are related to the physical energy deposition and hit time. Parameterizing the relation is called calibration, the parameters are the calibration constants. They must be known for the conversion of the QDC and TDC values into physical energies and times.

While the treatment of the time information is fairly straight forward, since the TDC channels correspond to 1 ns each, the following effects must be taken into account to extract the proper QDC channel to energy deposition function:

- The *scintillator response* and hence the light output depends on the particle type and its energy (cf. Fig. 3.3). This effect is called quenching and is increasing with the ionization density of the incident particle. The light yield per unit path length $\frac{dL}{dx}$ as a function of the deposited energy $\frac{dE}{dx}$ is commonly given by "Birk's formula"

$$\frac{dL}{dx} = \frac{S\frac{dE}{dx}}{1 + kB\frac{dE}{dx}}, \tag{3.5}$$

  with

$$S = \text{scintillation efficiency.}$$

  For all practical purposes, kB is treated as a single parameter to fit experimental data for a specific scintillator. See also [Kno79, Bir64].

- The *light collection efficiency*, i.e. the fraction of the initially produced light that actually reaches the PM tube, depends on the geometry and material of the scintillator, the light guide, and the position of the track.

- *Nonlinearities* can arise in the PM tube for large pulses due to space charge effects or dynode voltage fluctuations. They have to be taken into account by allowing the calibration constants to be light output dependent.

- The QDC count registered for a null energy deposition is called the *pedestal*. It is deliberately set to be non–zero to extract the zero–point of each QDC spectra and measured easily by collecting random experimental data in dedicated pedestal runs. For practical purposes — mainly to reduce the size of a recorded event — the pedestals are loaded into the QDC modules to suppress the output for channel contents below the pedestal value (pedestal suppression). In the offline analysis the pedestal must be subtracted from the QDC values of each channel.

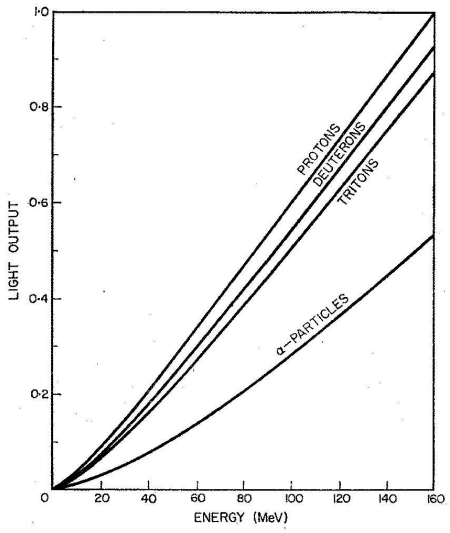

Figure 3.3: *Calculated scintillation response to protons, deuterons, tritons, and α–particles in NE 102 plastic scintillator [GP60].*

The calibration procedure consists of a manual "tuning" to migrate the set of previous calibration constants to a new beam period by using them as first order approximation[1]. The tuning is done by comparing correlations of energy depositions in different elements of the FRH extracted for both Monte Carlo and experimental data. Figure 3.4 shows the relevant ΔE–E–plots for the four FRH planes. These are all possible sets of plotting the energy deposition of an arbitrary FRH plane versus the energy deposition sum of this and an adjacent plane. Three characteristic energies have been marked with circles and are used as calibration points:

- Blue: Minimum ionizing particles. Their energy deposition is given by the scintillator thickness $t = 11$ cm and the typical specific energy loss[2] of $\frac{1}{\rho}\frac{dE}{dx} = 1.956\ \mathrm{MeV}/(\mathrm{g/cm^2})$.
- Red: Particles that are stopped in the second layer. The maximum energy sum deposited amounts to 160 MeV.
- Green: The "equilibrium" point, where the particle deposits equal amounts of energy in both layers (65 MeV).

By making slices and superimposing the Monte Carlo distributions on the experimental ones (cf. Fig. 3.5), an adequate representation of the calibration can be found. The reconstruction program contains two steering cards that can be changed now to adjust the calibration constants to the marked regions.

[1] For a description of a calibration procedure starting from "scratch" see [CW93].

[2] cf. [PDG04], Table 6.1. The FRH segments consist of BC400 scintillator, which is basically ($> 97\%$) Polyvinyltoluene.

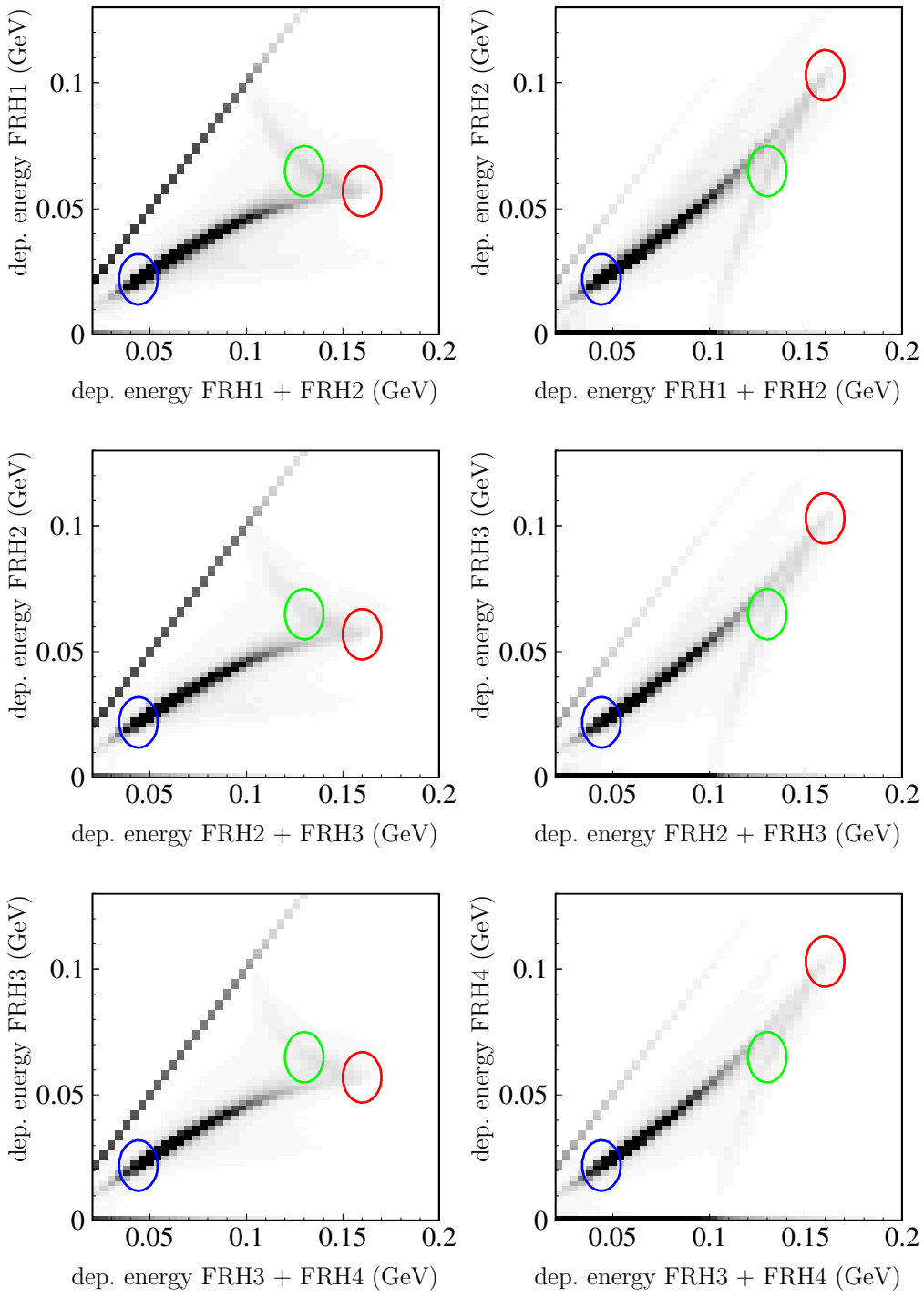

Figure 3.4: *Plotting the energy deposition of one FRH plane versus the energy deposition sum in this and an adjacent plane gives six* ΔE*–*E*–plots. For an explanation of the marked areas see the text.*

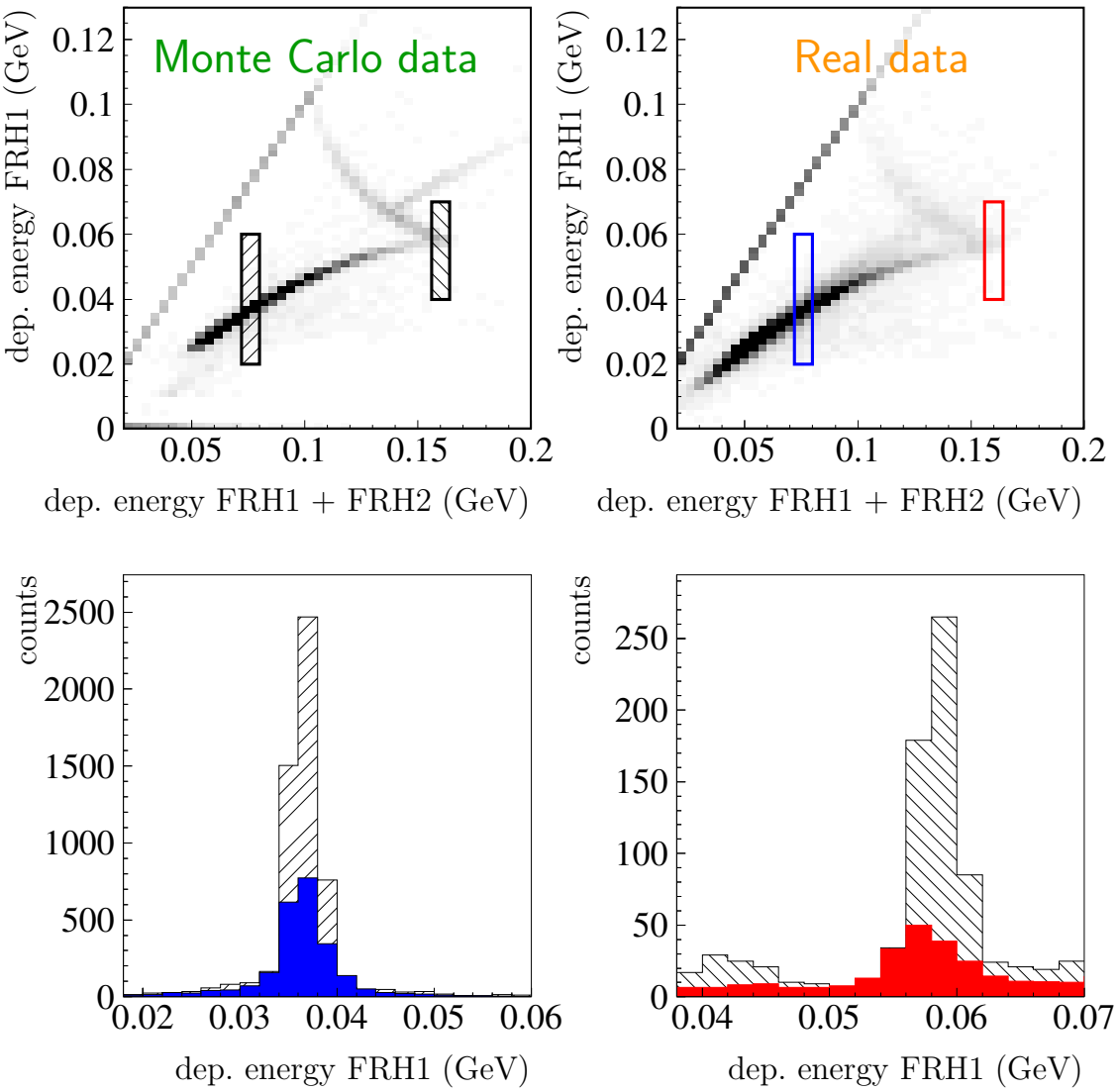

Figure 3.5: *Example spectra used in the energy calibration tuning. Cutting out the marked areas out of the* ΔE–E*–plots (upper row) and projecting them on the ordinate one obtains the histograms in the lower row. Now the experimental distribution (colored) can be compared to the expected spectra (hatched) and adjusted.*

3.3.3 Energy Calibration in the Central Detector

The calibrations of the scintillation detectors of the Central Detector are discussed in [Jac04] (PS) and [Koc04] (SE). While in the former basically the same procedure as described above for the Forward Detector is used, the calibration of the CsI calorimeter is done by selecting a sample of the reaction $pp \to pp\pi^0\pi^0$. It can be selected with a minimum bias on the kinematics since the signature — two charged particle tracks in FD and four neutral clusters in CD — is rather unique. By combining the four neutral clusters to two π^0's, the calibration is adjusted to give the correct pion mass.

For further details, please refer to the two mentioned publications.

3.3.4 Track Reconstruction

Different reconstruction procedures are applied depending on which part of the WASA detector a particle traversed.

For a *neutral* particle in the Central Detector, only hits in the calorimeter are registered. Therefore, the track reconstruction is reduced to an algorithm that decides which hits originated from the same particle and merges those hits into a cluster.

A *charged* particle also leaves signals in the PS and the MDC. For an in–depth description of the track finding and reconstruction routines of the MDC, see [Jac04].

If the Forward Detector is considered, the track reconstruction routine has to combine hits in adjacent detector planes into tracks by checking for geometrical overlap and coincidence. All the detectors in the Forward Detector except FRI are involved in this routine. Details about the inclusion of FRI into the offline analysis see [Pau05].

Following scheme describes the track finding in the Forward Detector:

- First, for all detector planes hits in adjoining detector elements are merged to so–called hit clusters. The user can decide how many hits in which planes should be clustered by adjusting a steering card. In the standard configuration, clustering is done for all FHD, FRH, and FPC planes for up to two hits. The hit time is ignored.

- Clusters in detector planes belonging to the same detector are merged into a so–called detector track, if they overlap geometrically and — optionally — in time.

  Special attention is paid to the FHD, since here all three planes have different geometrical shapes. Combining all three planes yields a set of detector track candidates which are compared to a lookup table to find valid detector tracks. These are called pixels.

- Finally, tracks are composed by matching FHD and FRH detector tracks. Again, matching is done by checking overlap in space and time. For each such track, all clusters in all remaining detector planes are tried and added if they fulfill the overlap conditions. The deposited energy of the track is the sum of all cluster energies. However, since not all Forward Detector planes are calibrated, only FHD3 and FRH1–4 are added up. The track time is defined by the average of the hit time of all included clusters. The track direction is given by the FPC hit coordinates with respect to the nominal vertex. If a FPC hit is missing, then the FHD defines the track direction. In either case, a vertex position at the coordinate origin is assumed. Tracks with neither FPC or FHD hit are considered to be neutral tracks.

All track candidates found this way are filled into the Track Bank. Of course, these candidates are not perfect: Some tracks may share the same hit cluster, others may consist only of single clusters that could not be matched. A simple clean–up procedure deletes some of these cases from the Track Bank. Furthermore, the user has the possibility to merge tracks that are too close reducing the number of "ghost tracks" even more.

3.3.5 Particle Identification

This section is restrained to the particle identification in the Forward Detector since no identification methods in the Central Detector were needed in this work.

For each track in the Forward Detector the direction and the deposited energy have been determined as outlined. To get a proper four–vector the momentum of each track needs to be calculated. This can only be done if the mass of each incident particle is known.

The identification of particles in the Forward Detector makes use of the dependence of their specific energy loss in matter on their mass and charge as described by the Bethe Bloch formula. When plotting the energy loss in a rather thin scintillator element ΔE against the total deposited energy E, different particles will form bands in different regions of the ΔE–E plane.

Figure 3.6 shows such a plot for preselected events from the beam period in November, 2001. Protons populate the lower band while deuterons form the upper. While the left picture contains tracks stopped in the first layer of the FRH, using the third layer of the FHD as a ΔE–counter, the right picture shows tracks stopped in the second layer of the FRH. Here, the first layer of the FRH can be used as a ΔE–counter, resulting in an obviously better separation of both bands. Therefore, whenever possible the latter was applied for identification purposes, the former only being exercised for stopped particles in FRH1. The lines depict the cuts defining a proton or deuteron, respectively.

It should be noted that for beam periods with a high energy proton beam and

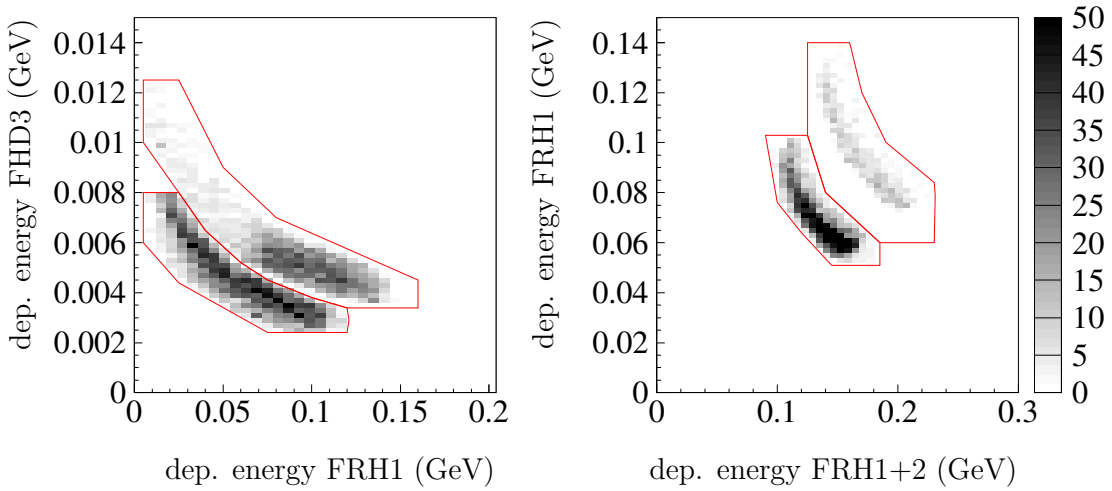

Figure 3.6: *Particle identification via* ΔE–E*–plot for preselected events. The (lower) proton band is clearly distinguishable from the (upper) deuteron band. The lines depict the cuts used in the offline analysis.*

hydrogen pellets the particle identification is not crucial since almost all registered tracks in the Forward Detector originate from protons. Additionally, the WASA 4π detector renders it possible to detect and measure all outgoing particles thus adding redundancy to the particle identification, especially for neutral meson production and decays.

3.3.6 Nonuniformity Correction

As mentioned above, the light collection efficiency of each FHD and FRH element is a function of their respective geometry and depends on the particle type due to quenching effects. It results in a nonuniform light output which can be corrected once particle type and scattering angle of each track are known.

The nonuniformity constants are extracted by comparing the expected energy deposition given by a Monte Carlo data sample with the measured energy response. Usually, particles reaching the FVH are selected for this analysis assuring an almost constant energy deposition and an even event distribution over the whole Forward Detector.

The scattering angle dependence is parameterized by defining 11 radial bins along the straight elements of the FHD third layer. These are projected on the FRH leaving the 11th bin outside the FRH and therefore empty. Empty or only partially filled bins are given the nonuniformity constant of the nearest bin with a valid value. A linear interpolation is applied for scattering angles in between radial bins. The

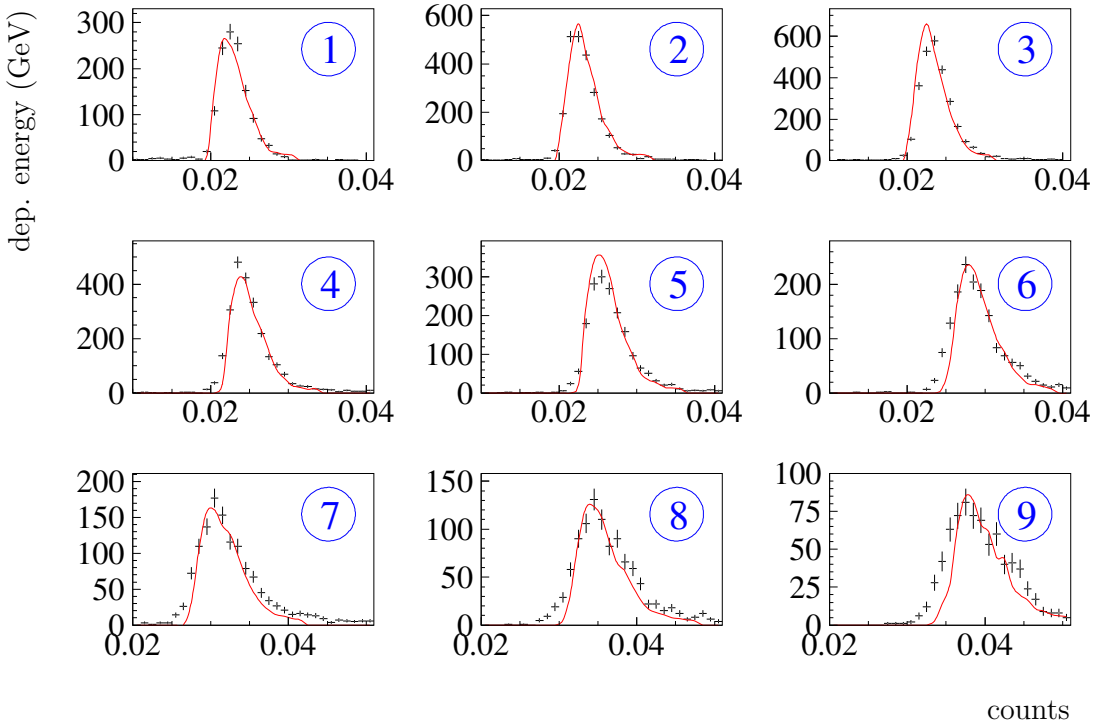

Figure 3.7: *Superimposing MC data on real data (crosses), the nonuniformity constants can be obtained by comparing the peak positions of both distributions. The spectra shown are for radial bins 1 (innermost) to 9 from element No. 1 of FRH1. Note that the position of the photo multiplier readout via lightguide is beyond bin 9.*

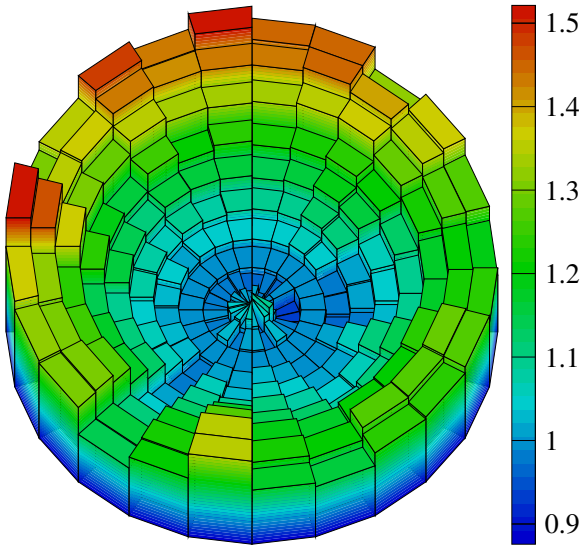

Figure 3.8: *Nonuniformity constants for all elements of FRH1. The ϕ angle relates to the element number, starting at nine o'clock with element no. 1, while the radius shows the radial bins.*

spectra of the first nine bins for an arbitrary element of FRH1 are shown in Fig. 3.7. The resulting nonuniformity constants for FRH1 can be seen in Fig. 3.8.

3.3.7 Energy Reconstruction

So far, only deposited energies have been mentioned. For an ideal detector with no gaps, no passive material in it, and perfect scintillation efficiency (no quenching!), the deposited energy would be identical to the kinetic energy, if the particle was stopped in the calorimeter. In reality, these energy losses have to be taken into account by calculating a set of kinetic energy reconstruction parameters that translate the measured deposited energy into the original kinetic energy of the traversing or stopped particle.

Here, such parameters are determined by analyzing a Monte Carlo sample, comparing the reconstructed energy to the "true" energy given by the GIN four–vectors. This is done by taking into account the segmentation of the Forward Detector along the z–axis, having one set of reconstruction parameters for each plane in the FRH and the FHD3. An additional set is needed for particles that are not stopped in the Forward Detector.

The energy reconstruction marks the final step in the obligatory part of the reconstruction procedure. The user has now a complete set of four–vectors at his disposal. All further analyses depend now on the specific reaction to be investigated.

Chapter 4

Inelastic Reactions in Deuteron–Proton Collisions

Since its discovery in the cosmic radiation [OP47], the pion has played an important role in nuclear physics. As a *virtual* particle, it is the exchange corpuscle of the Yukawa potential and is accountable for the long range component and a large part of the tensor force of the nuclear potential [EW88] in multiple meson exchange models. The *real* pion is the lightest meson and therefore the one to be produced with lowest energies in inelastic nucleon–nucleon or nucleon–nucleus reactions. This makes it particularly interesting, since

- it provides an easily accessible testing ground for the predictive power of nuclear interaction models for parity and isospin symmetries,
- its characteristics serve as input parameters for the *virtual* pion, and
- it can be used as a probe to test the properties of nuclear matter, especially the high momentum component of the nuclear wave function due to the high momentum transfer in (p,π) reactions.

The latter led to an extensive experimental and theoretical effort which has been reviewed in [Höi79] and [MM79], for example. It turned out that the influence of the (p,π) reaction mechanisms involved could not be disentangled easily from the nuclear structure effects due to the complexity of the nuclei investigated.

The logical step was to focus the measurements on the simplest nucleus available, the deuteron, so that the effects of the nuclear environment may be visible while a detailed theoretical treatment might be possible as the structure of the deuteron nucleus is well known. Furthermore, with the increasing high quality data on the pion production in the nucleon–nucleon system, the knowledge of the $\mathrm{NN} \rightarrow \mathrm{NN}\pi$ reactions could be utilized directly to examine if the nucleon–nucleon interaction is sufficient to explain the total cross section and differential distributions of the pion production in the nucleon–deuteron system (impulse approximation) or if three nucleon mechanisms might be involved.

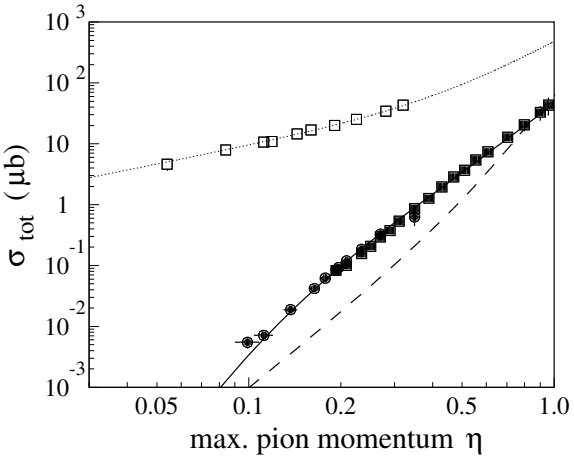

Figure 4.1: *The excitation function for* $pd \to pd\pi^0$ *(filled symbols) obtained from [Roh94]. The data are compared to predictions from Spectator Model [MN93] without (dashed line) and with (solid line)* pd*-FSI. The latter includes an arbitrary normalization factor, therefore having no predictive power in regard to the absolute magnitude of the cross section. The open symbols show the* $pn \to d\pi^0$ *cross sections and the parameterization (dotted line) used as input to the Spectator Model calculation.*

The first near threshold experiment in this spirit was done in 1991 at the Indiana University Cooler Facility (IUCF) in Bloomington, Indiana [Roh94]. Here, a cooled proton beam in conjunction with a windowless gas jet target allowed for precise measurements of the reactions $pd \to pd\pi^0$ and $pd \to nd\pi^+$ close to the reaction threshold, where

- the $NN \to NN\pi$ cross sections had been determined accurately,
- only the lowest partial waves contribute to the reaction which allows the interpretation and theoretical treatment of the data, and
- the Δ resonance is not excited, therefore giving a clear view on nonresonant production mechanisms.

Data were taken for proton beam energies between $T_p = 208.4$ MeV and $T_p = 294.6$ MeV. For an easier comparison of the two reactions, it is convenient to introduce the threshold parameter η defined as $\eta = p^\star_{\pi,\max}/m_\pi c$, where $p^\star_{\pi,\max}$ is the maximum pion momentum in the center of mass system. In terms of η, the above energy range translates to $0.1 \leq \eta \leq 0.96$. The resulting excitation function for $pd \to pd\pi^0$ is shown in Fig. 4.1.

To analyze the data, the measured total cross sections and differential distributions were compared to the so–called *Spectator Model* by [MN93]. Basically, it describes the $pd \to Nd\pi$ reaction through an underlying *quasifree* process $pN \to d\pi$ where the initial beam proton interacts with only one of the nucleons in the deuteron while the other does not participate in the interaction at all. It will be described in some detail further down.

The following conclusions were reached in [Roh94]:

- For the low energy data, $0.1 \leq \eta \leq 0.5$, the Indiana experiment yielded reliable total cross sections. The data were well described by a partial wave analysis, indicating an almost constant matrix element. The Spectator Model failed to describe the magnitude of the excitation function by a factor of up to five (cf. Fig. 4.1).

- For $\eta > 0.5$, the results were inconclusive with respect to the reaction mechanism due to the rapidly decreasing acceptance of the detector. This is illustrated with the Dalitz plots shown in [Roh94] (Fig. 4.3) at $\eta \approx 0.89$. The second row shows (from left to right) the generated Dalitz plot for the Spectator Model, the simulated distributions including detector acceptance for $pd \rightarrow pd\pi^0$, and $pd \rightarrow nd\pi^+$. Obviously, the detector sensitivity for the regions of phase space that are favored by the Spectator Model was almost negligible for $pd \rightarrow pd\pi^0$.

The decreasing acceptance of the IUCF experiment for high η can be explained with Fig. 4.2, where the square of the deuteron wave function in momentum space is plotted as a function of the spectator momentum κ (top) and the region, which can contribute to a quasifree $pd \rightarrow Nd\pi$ reaction is shown as a function of η (bottom). The higher η is, the larger the kinematically allowed region grows. Since the deuteron wave function favors lower momenta, one can deduce that with increasing η the spectator is produced preferably with low or no momentum in the center of mass system, rendering it undetectable for the IUCF setup.

To overcome this limiting acceptance and to clarify the ambiguities in the IUCF experiment at higher energies, a modified experiment was carried out with the

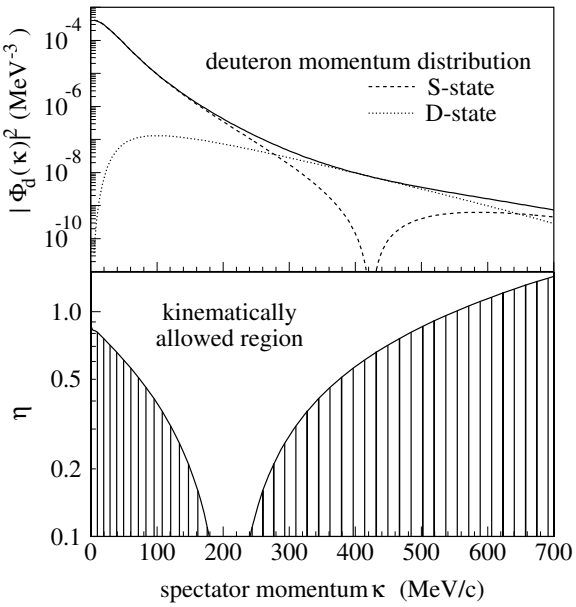

Figure 4.2: *The square of the deuteron wave function in momentum space is plotted as a function of the spectator momentum (top). The region, which can contribute to a quasifree $pd \rightarrow Nd\pi$ reaction is shown as a function of η (bottom). Its upper limit is given by energy and momentum conservation within the overall system and its lower limit is given by the minimum invariant mass within the two nucleon system $pN \rightarrow d\pi$ [Roh94].*

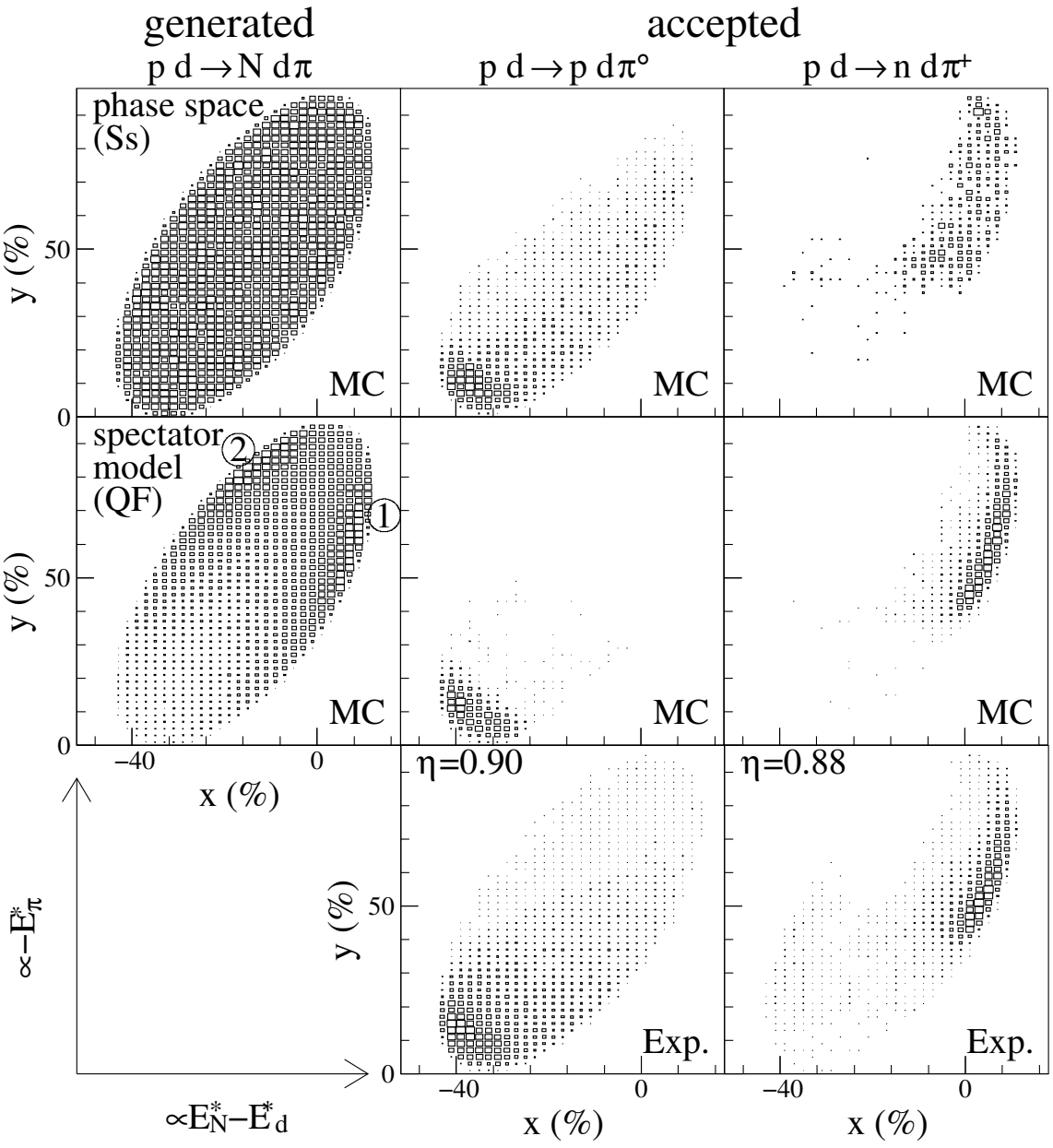

Figure 4.3: *Dalitz plots for* $pd \to Nd\pi$ *at* $\eta \approx 0.89$ *from [Roh94]. The top two lines are Dalitz plots obtained from Monte Carlo simulations, assuming a pure phase space distribution and the Spectator Model [MN93]. The left column shows the generated distributions, simulated ones including the detector acceptance are shown in the middle for* $pd \to pd\pi^0$ *and on the right for* $pd \to nd\pi^+$*. The bottom line shows the experimental IUCF data. Clearly, the limited acceptance for the Spectator Model in* $pd \to pd\pi^0$ *for forward (①) and backward (②) going* π^0 *can be seen.*

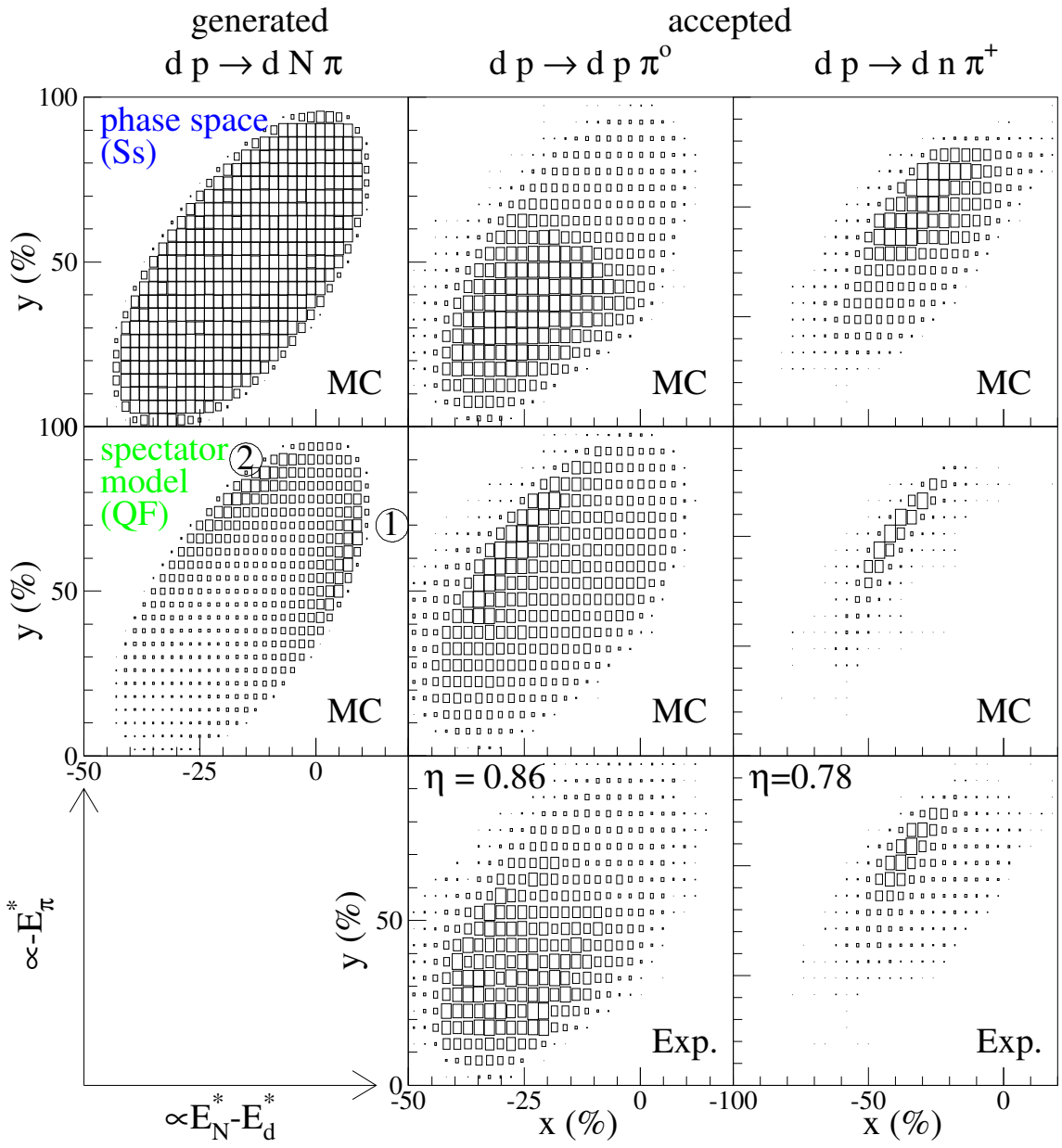

Figure 4.4: *Dalitz plots for* $dp \to dN\pi$ *at* $\eta \approx 0.80$ *from [Gre99]. The plots are arranged in the same order as in Fig. 4.3. Note the increased acceptance for forward (①) and backward (②) going* π^0*'s in the second line.*

PROMICE/WASA setup at CELSIUS [Gre99]. Besides the additional capability of the PROMICE/WASA setup to detect γ's from the decaying π^0 the significant increase in detector acceptance was achieved by using inverse kinematics, i.e. a deuteron beam impinged on a cluster jet hydrogen target (deuteron beams of the necessary energies were not available at the IUCF). This gives both nucleons in the deuteron roughly half the beam energy, so that the spectator nucleon whose momentum, following the argumentation above, remains mostly unchanged, is emitted into the front cone, where it can be registered by the Forward Detector. Beam energies between $T_d = 437$ MeV and $T_d = 559$ MeV were used, corresponding to an η range of $0.32 \leq \eta \leq 0.86$.

The results in [Gre99] can be summarized as follows:

- For $\eta < 0.5$, the data were in good agreement with the previous measurement at Indiana.
- At higher energies, the cross sections turned out to be larger which was explained by the already mentioned limited acceptance of the Indiana setup at higher energies.
- With the higher sensitivity for the Spectator Model (cf. Fig. 4.4), [Gre99] could show that the differential distributions cannot be described with the quasifree process alone. The discrepancies were solved by assuming so–called coherent pion production mechanisms, where all three nucleons participate in the momentum transfer. Since this coherent contribution is based on a partial wave analysis (see below), it was concluded that the data were still not understood in terms of detailed reaction mechanisms.
- Besides the two reactions already discussed, first data on $dp \to ppp\pi^-$ and $dp \to dp\gamma$ were presented. However, since an investigation of these reactions had not been planned for, the experimental conditions were not optimal: For the former, the detection of all particles, especially the π^- would have helped to reject background, the latter suffered from limited acceptance.

In April, 1999, the TSL Program Advisory Committee (PAC) accepted the proposal CA55 [Sco99]. Its goal was the extension of the investigation of inelastic channels in the deuteron–proton system as outlined above with the close to 4π acceptance of the WASA detector. Explicitly, its physics goal were

- the verification of the previous experiments with a large acceptance. In particular the $dp \to dn\pi^+$ reaction would benefit from the detection of the π^+ at large angles so that the accepted phase space would overlap with the one for $dp \to dp\pi^0$, probably opening insights into the coherent mechanisms,
- the determination of the $dp \to ppp\pi^-$ cross section by measuring and identifying all four final state particles,

- gaining access to regions of the phase space with low γ energies in $dp \to dp\gamma$, and
- extracting angular distributions of the pion and the γ in all reactions above, respectively, because they are more sensitive to the production mechanisms involved than the angle integrated cross sections obtained so far.

Moreover, comparisons with the data taken from the previous setup were supposed to help improve the performance of the new experimental setup during its commissioning phase and establish a solid understanding of the WASA detector.

In this work, the analysis of the data taken within the scope of proposal CA55 were carried out. The two reactions of interest are the neutral pion production $dp \to dp\pi^0$ and the bremsstrahlung process $dp \to dp\gamma$. In the following, first the necessary event generation and Monte Carlo simulation procedures will be outlined and the key differences between the PROMICE/WASA and the WASA setup shown (Sec. 4.1). Next, Sec. 4.2 will cover the selection and analysis of experimental data using the previously simulated Monte Carlo data sets.

4.1 Creating and Analyzing Monte Carlo Data

As already has been pointed out in Sec. 3.1, the generation of an realistic event sample requires the supplement of the matrix element $|M|^2$. Following the argumentation in [Gre99], two different approaches will be used to describe the experimental data: the already mentioned Spectator Model and a coherent mechanism. The two models will be introduced now in more detail.

4.1.1 The Spectator Model [MN93]

For a pure quasifree dp reaction, only one of the nucleons in the deuteron interacts with the proton while the other does not participate in the momentum transfer (hence the name spectator, cf. Fig. 4.5). There are three possible nucleon–nucleon processes that could contribute to $pd \to pd\pi^0$:

1. $pn \to d\pi^0$
2. $pp \to pp\pi^0$
3. $pn \to pn\pi^0$

According to the reasoning in [MN93], reaction No. 1 dominates, because

- near threshold reaction two has a smaller cross section and
- reaction three favors the four body final state $ppn\pi^0$.

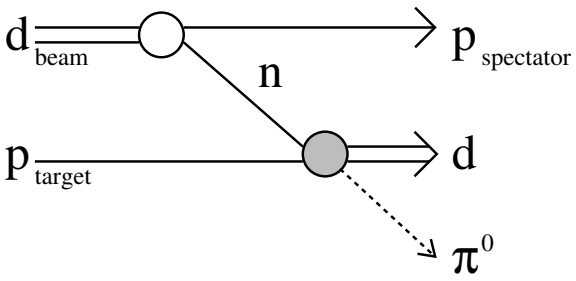

Figure 4.5: *The Spectator Model from [MN93]. The two vertices denote the deuteron wave function (white) and the free* $np \to d\pi^0$ *reaction (grey).*

The neutron that interacts with the target proton according to reaction No. 1, however, is not at rest but has momentum according to the momentum distribution inside the deuteron. Consequently, the Spectator Model needs two ingredients:

- The nucleon momentum (κ) probability density of the deuteron $|\Phi_d(\kappa)|^2$, here obtained from the Bonn potential [MHE87], where the S and D state probabilities of the deuteron were added incoherently (cf. Fig. 4.2), and
- the total cross section for $np \to d\pi^0$.

Combining both contributions, the matrix element of the Spectator Model can be written as

$$|M_{spec}|^2 = \frac{2\,E'_p\,E'_B\,E'_s}{E^*_n\,E^*_p}\;|\Phi_d(\kappa)|^2 |M_{np\to d\pi^0}|^2, \tag{4.1}$$

where

E'_p, E'_B, E'_s: the total energies of the target proton (p), the beam deuteron (d), and the spectator (s) in the $dp \to dp\pi^0$ frame, where the $d\pi^0$ subsystem is at rest.

E^*_n, E^*_p: the total energies of the participating proton (p) and neutron (n) in the center of mass system of the $np \to d\pi^0$ reaction.

$|\Phi_d(\kappa)|^2$: the deuteron wave function in momentum space with

κ: the neutron momentum in the deuteron, and

$|M_{np\to d\pi^0}|^2$: the invariant matrix element of the elementary $np \to d\pi^0$ process.

The matrix element $|M_{np\to d\pi^0}|^2$ is not derived from a microscopic model. Instead, the existing experimental cross sections are used to express the matrix element:

$$|M_{np\to d\pi^0}|^2 = 16\,(2\pi)^2\,s_2 \frac{p^*_p}{q^*} \frac{d\sigma_{np\to d\pi^0}}{d\Omega_{q^*}}, \tag{4.2}$$

where

s_2: the square of the total invariant mass in the $np \to d\pi^0$ system.

p^*_p, q^*: the proton and pion momenta in the center of mass system of the $np \to d\pi^0$ reaction.

$d\sigma_{np\to d\pi^0}/d\Omega_{q^*}$: the experimental cross section of $np \to d\pi^0$.

In [Roh94], the calculations were extended to introduce a parameterization of the differential cross section for $pn \to d\pi^0$:

$$\frac{d\sigma_{np\to d\pi^0}}{d\Omega_{q^*}}(\cos\Theta^*_\pi) = \frac{\sigma_{np\to d\pi^0}(\eta)}{4\pi} + a_2(\eta)P_2(\cos\Theta^*_\pi), \tag{4.3}$$

with the Legendre polynomial P_2 and the parameter $a_2 = (47.2\ \mu b)\eta^3$, obtained from a fit to the experimental $pn \to d\pi^0$ data.

The angle integrated cross section $\sigma_{np\to d\pi^0}(\eta)$ is calculated in [H+91] with the following parameterization (cf. Fig. 4.1)

$$\sigma_{np\to d\pi^0}(\eta) = \frac{1}{2}[(184\mu b)\eta + (781\mu b)\eta^3], \tag{4.4}$$

which is valid for values of $\eta < 1$ in the $pn \to d\pi^0$ center of mass system. For larger center of mass energies, a Lorentzian form was fitted to the world data set of $pp \to d\pi^+$ cross sections. The result was then scaled according to

$$\sigma(pp \to d\pi^+)/\sigma(pn \to d\pi^0) = 2, \tag{4.5}$$

the factor of two arising from isospin invariance.

For the bremsstrahlung reaction, the Spectator Model is derived in a similar fashion by replacing the cross section $d\sigma_{np\to d\pi^0}/d\Omega_{q^*}$ in Eq. 4.2 with $d\sigma_{np\to d\gamma}/d\Omega_{q^*}$. According to [G+02], however, these cross sections are not well known, so that parameterizations of the total and differential cross sections of the inverse process, i.e. the photodisintegration $\gamma d \to np$, are used.

4.1.2 Coherent Mechanisms

Since the Spectator Model failed to describe the experimental data in both previous works, the gap was closed with a purely phenomenological approach by making a partial wave expansion for $dp \to Nd\pi$. According to Eq. 3.3, the matrix element is given by

$$|M|^2 = |\langle \Psi_f(\vec{p}_N, \vec{p}_d, \vec{p}_\pi)|T|\Psi_i\rangle|^2, \tag{4.6}$$

with the initial and final state wave functions Ψ_i and Ψ_f and the transition operator T.

For a three body final state $dp \to Nd\pi$, the wave function can be factorized into two parts

$$\Psi_f(\vec{p}_N, \vec{p}_d, \vec{p}_\pi) = \Psi_{Nd}(\vec{p}_{Nd})\Psi_\pi(\vec{q}), \tag{4.7}$$

where $\vec{p}_{Nd}$ is the momentum of the nucleon relative to the deuteron in the Nd center of mass system and $\vec{q}$ the momentum of the pion with respect to the Nd subsystem. The factorized wave function can now be parameterized in terms of a partial wave expansion, introducing the angular momentum L for the Nd subsytem and l for the pion angular momentum in respect to the Nd subsystem. Following the argumentation in [Gre99], only the eight partial wave contributions listed in Table 4.1 are considered.

$\lvert M\rvert^2 \propto$ constant	Ss wave (L=0, l=0)
$\lvert M\rvert^2 \propto \lvert\vec{p}_\pi\rvert^2$	Sp wave (L=0, l=1)
$\lvert M\rvert^2 \propto \lvert\vec{p}_{Nd}\rvert^2$	Ps wave (L=1, l=0) isotropic
$\lvert M\rvert^2 \propto \lvert\vec{p}_{Nd}\rvert^2\lvert\vec{p}_\pi\rvert^2$	Pp wave (L=1, l=1) isotropic
$\lvert M\rvert^2 \propto \lvert\vec{p}_{Nd}\rvert^2\lvert\vec{p}_\pi\rvert^4$	Pd wave (L=1, l=2) isotropic
$\lvert M\rvert^2 \propto (\lvert\vec{p}_{Nd}\rvert\cos\Theta_N)^2$	Ps wave (L=1, l=0) anisotropic
$\lvert M\rvert^2 \propto (\lvert\vec{p}_{Nd}\rvert\cos\Theta_N)^2\lvert\vec{p}_\pi\rvert^2$	Pp wave (L=1, l=1) anisotropic
$\lvert M\rvert^2 \propto (\lvert\vec{p}_{Nd}\rvert\cos\Theta_N)^2\lvert\vec{p}_\pi\rvert^4$	Pd wave (L=1, l=2) anisotropic

Table 4.1: *The applied parameterizations for coherent production mechanisms [Gre99].*

As can be seen, anisotropies in the pion angle or interference terms are neglected. Also, no assumption whatsoever is made on the nature of the microscopic production mechanism. The incoherent sum of the partial wave contributions in Table 4.1 is called the coherent mechanism.

4.1.3 Selection Rules and Cuts

To ensure comparability with the data taken with the PROMICE/WASA setup, similar selection rules as in [Gre99] are used, where applicable.

For the reactions $dp \to dp\pi^0$ and $dp \to dp\gamma$, the following common criteria are applied on Monte Carlo data to classify a valid event:

1. There are two charged particle tracks in the Forward Detector ("FDCFDC") with at least hits in the third layer of FHD and the first layer of FRH.

2. The two tracks are identified as a proton and a deuteron track, respectively, via ΔE–E method ("part. id.").

3. There is at least one neutral particle track in the Central Detector ("CDN").

Reaction $dp \to \ldots$	Acceptance (%) of Cut #1 ph.sp.	Cut #1 SM	Cut #2 ph.sp.	Cut #2 SM	Cut #3 ph.sp.	Cut #3 SM
dp	< 0.1	—	0.0	—	0.0	—
$pp\pi$	7.2	—	0.0	—	0.0	—
$dp\gamma$	17.4	54.1	9.8	22.9	8.3	19.5
$dp\pi^0$	48.2	56.4	31.9	29.7	30.5	28.2
$dn\pi^+$	9.2	6.1	0.3	0.4	< 0.1	0.0
$pp\pi\pi^0$	46.1	—	1.4	—	1.3	—
$ppp\pi^-$	44.6	—	0.7	—	0.2	—
$pn\pi\pi^+$	8.1	—	0.0	—	0.0	—

Table 4.2: *Cumulative acceptance for all dominant reactions with at least two charged particle tracks in the FD after the "FDCFDC" (#1) the "part. id." (#2), and the "CDN" (#3) cut (see text). SM: Spectator Model, ph.sp.: phase space distribution.*

Table 4.2 lists all dominant reactions at the given beam energy of $T_d = 560$ MeV that can fulfill the "FDCFDC" cut. They are simulated with a pure phase space distribution (ph.sp.) except in three cases, where also the Spectator Model (SM) is available. For each reaction, the overall acceptance of each cut listed above is given.

While the cuts from [Gre99] on the angles and energies of the deuteron–proton system are not used, the following additional reaction specific selection criteria are adopted:

- For $dp \to dp\gamma$, it must be ensured that the single γ does not originate from a π^0 decay. Therefore, the opening angle and planarity between the predicted γ direction $(\Theta, \Phi)_{\text{miss. momentum FD}}$, obtained from the deuteron–proton system, and the measured CDN track $(\Theta, \Phi)_{\text{CDN}}$ is calculated (cf. Fig. 4.6). An event is validated, if $\angle\left((\Theta, \Phi)_{\text{miss. momentum FD}}, (\Theta, \Phi)_{\text{CDN}}\right) \leq 23^\circ$ and $|\text{missing mass}^2| \leq 0.01\,\text{GeV}^2/c^4$.

- For $dp \to dp\pi^0$, a cut in the missing energy vs. missing mass plane depicted by the box seen in Fig. 4.7 is applied. The box includes events with lower missing mass if the missing energy is large. This follows from the argument in [Gre99] that for high missing energies both the proton and the deuteron are emitted with high energies close to the beam pipe, resulting in a decrease of the energy reconstruction accuracy and therefore smaller missing mass.

Finally, a second neutral track can be demanded in the Central Detector ("CDNCDN") to gain maximum selectivity for the π^0 production channel.

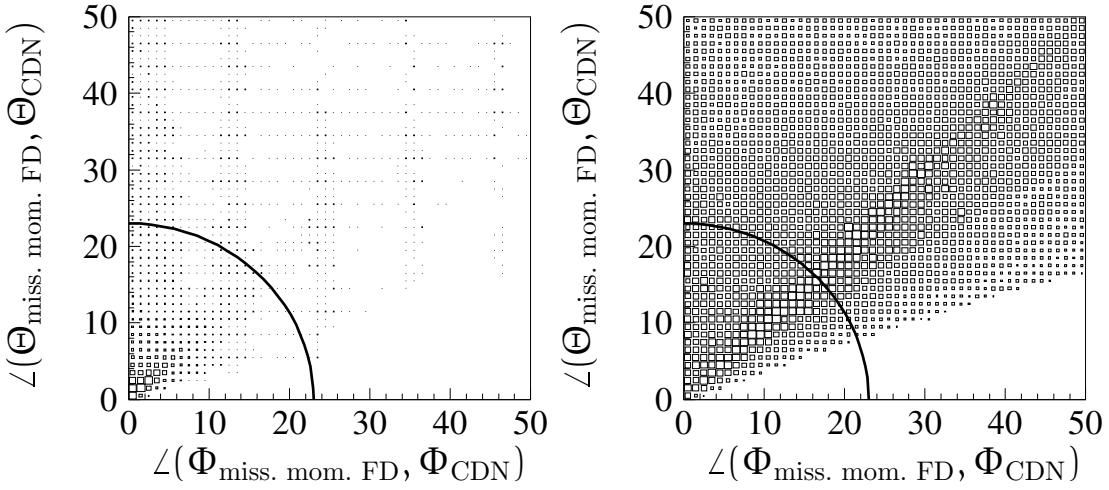

Figure 4.6: *Opening angle* $\angle(\Theta_{\text{miss. momentum FD}}, \Theta_{CDN})$ *vs. planarity* $\angle(\Phi_{\text{miss. momentum FD}}, \Phi_{CDN})$ *distributions for* $\mathtt{dp} \rightarrow \mathtt{dp}\gamma$ *(left) and* $\mathtt{dp} \rightarrow \mathtt{dp}\pi^0$ *(right). For valid* $\mathtt{dp} \rightarrow \mathtt{dp}\gamma$ *events, both angles are expected to be close to zero. The cut is indicated by the arc.*

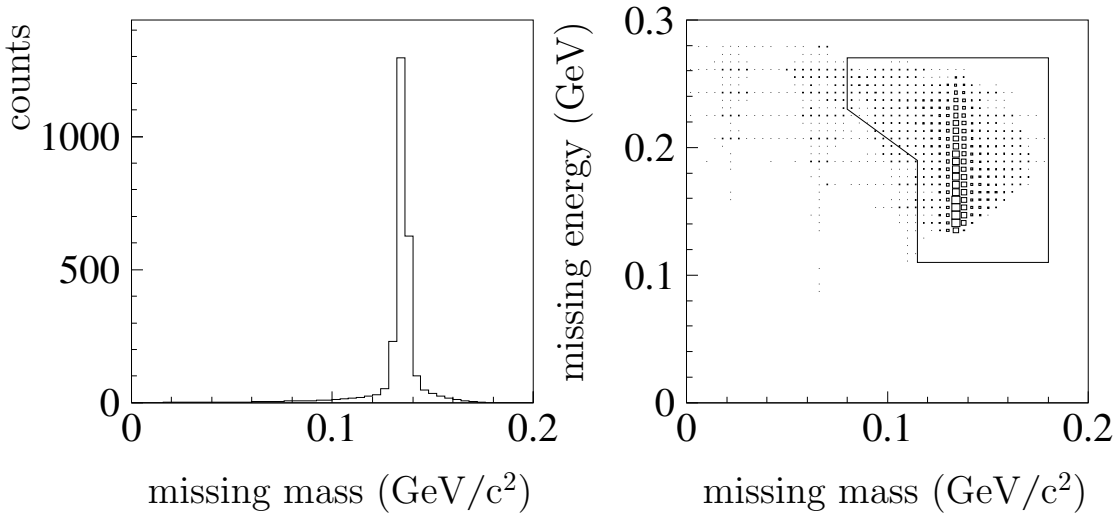

Figure 4.7: *Missing mass spectrum (left) of the reaction* $\mathtt{dp} \rightarrow \mathtt{dp}\pi^0$ *for Monte Carlo data. The right picture shows the missing mass distribution as a function of the missing energy calculated from the* dp *system. The box depicts the missing mass cut.*

Comparison of PROMICE/WASA and WASA

Using the above selection rules, the overall acceptance, i.e. the number of selected events after all cuts divided by the number of initially generated events, of the previous PROMICE/WASA and the recent WASA setup is compared.

In Tab. 4.3, the overall acceptance of the reactions $dp \to dp\pi^0$ and $dp \to dp\gamma$, simulated with a pure phase space distribution and the Spectator Model, are shown. Two values are given for each setup. In the case of the PROMICE/WASA setup, the results from [Gre99] are listed together with azimuth coverage corrected values in parentheses. These take into account that the difference between both experimental setups is partly due to the smaller azimuthal coverage (100°) of the previous experiment (cf. Sec. 2.3.3). Since the full azimuth angle coverage of the WASA detector only increases the statistics measured with a given luminosity without giving access to different regions in phase space, the azimuth coverage corrected values give better comparability to the WASA acceptance. The correction factor amounts to $360°/100° = 3.6$.

Reaction $dp \to \ldots$	Acceptance (%) phase space dist. P/W	phase space dist. WASA CDN/2CDN	Spectator Model P/W	Spectator Model WASA CDN/2CDN
$dp\gamma$	1.5 (5.4)	6.8 / —	1.7 (6.1)	16.5 / —
$dp\pi^0$	8.1 (29.2)	28.9 / 19.8	4.9 (17.6)	26.9 / 18.6

Table 4.3: *Comparison of the PROMICE/WASA (P/W) to the WASA acceptance. The values for the P/W setup are from [Gre99]. See text for discussion.*

The acceptance of the WASA detector is given without and with the last selection level, where two neutral particle tracks are required in the Central Detector. The former are based on the same selection criteria as in [Gre99]. They show that the WASA setup's larger solid angle coverage increases mostly the sensitivity for the Spectator Model. This is only a mild increase for $dp\pi^0$, but a dramatic one for $dp\gamma$. This increase is due to two features of WASA: First, the larger scattering angle coverage of the Central Detector and second, the access to a smaller scattering angle in the Forward Detector due to its reduced distance from the vertex point.

The influence of this increased sensitivity can be seen best in the energy distribution of the final state proton. Figure 4.8 shows the distributions from phase space distribution (ph.sp.) and the Spectator Model (SM) for the pion production (left) and the bremsstrahlung reaction (right). The solid lines depict the spectra from the WASA (C/W) Monte Carlo while the PROMICE/WASA (P/W) Monte Carlo distributions from [Gre99] are drawn with dotted/dashed lines. Note, that the latter are scaled with the azimuth coverage correction factor of 3.6 from above.

Summarizing, one expects a substantially larger acceptance for both reactions due to the complete coverage of the azimuth angle in the WASA Central Detector.

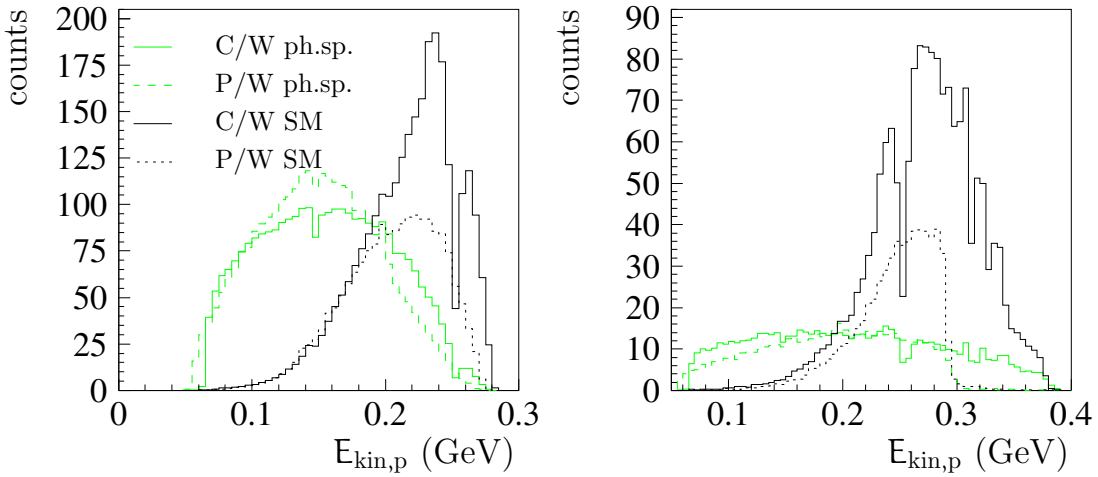

Figure 4.8: *Comparison of the PROMICE/WASA (P/W) to the WASA (C/W) acceptance with Monte Carlo data. The energy distributions of the protons for* $dp \to dp\pi^0$ *(left) and* $dp \to dp\gamma$ *(right) are shown for pure phase space distribution (ph.sp.) and the Spectator Model (SM). See text for discussion.*

Moreover, the extended acceptance due to the larger coverage of the scattering angle gives access to regions of phase space that were not covered before, especially for the reaction $dp \to dp\gamma$.

4.2 Selecting and Analyzing Experimental Data

In total, 15 shifts of eight hours each were allocated for the CA55 proposal. Both in November, 1999, and November, 2000, seven shifts were used, but due to severe experimental problems with the Pellet Target system, only unusable data were taken. In November, 2001, however, some of the experimental difficulties had been overcome and data at a deuteron beam energy of $T_d = 560$ MeV, corresponding to a threshold parameter of $\eta = 0.865$ in $dp \to dp\pi^0$, were recorded during four shifts. Table 4.4 contains a summary of all data runs from this beam period.

Already during data taking, the impact of the detector setup modifications on the data quality could be observed. It proved to be extremely difficult to produce a deuterium beam with the same intensity and accelerator cycle as in the previous experiment. This was related to the Pellet Target that caused beam heating and high intensity losses due to its higher density in comparison to the Cluster Jet Target of the PROMICE/WASA setup. The cycle length was set to 100 s, three times lower than in [Gre99]. The flat top was set from 37 s to 65 s, yielding a duty factor of 28% (79% in [Gre99]).

The trigger setup is summarized in Table 4.5. Only the trigger used in the following sections is listed. No naming convention existed at that time, so all triggers are

Tape #	Run #	Number of events (10^6)	Total time (h)	comment
CW0115	19	1.70	3.89	
CW0115	20	0.25	0.53	
CW0115	21	2.46	6.25	
CW0115	22	0.16	0.42	
CW0115	23	0.05	0.19	pedestal run
CW0116	24	0.04	0.15	unusable
CW0116	25	0.01	0.04	unusable
CW0116	26	1.68	5.34	
CW0116	27	3.08	10.12	

Table 4.4: *Run summary for the beam period in November, 2001, with a deuteron beam of* $T_d = 560$ MeV*, corresponding to a threshold parameter of* $\eta = 0.865$ *in* $dp \to dp\pi^0$.

numbered in the order they appeared in the trigger box. PT stands for prescaled trigger, TR for unprescaled.

Trigger name unpres. / pres.	Definition	comment
TR22 / PT22	$2 \cdot \text{FWC} \wedge 2 \cdot \text{FHD3}$	physics trig. for $dp\pi^0, dp\gamma$

Table 4.5: *Hardware trigger defined in the beam period in November, 2001.*

Trigger PT22 requires two hits in the FWC and two hits in the third layer of the FHD. It is the main physics trigger for all reactions that have two charged particles in the Forward Detector, i.e. the π^0 and the bremsstrahlung production. It is also sensitive to the π^+ production, but due to a very high background the identification of the π^+ proved to be unfeasible.

Several other physics triggers were defined but posed certain problems that led to their ommission. These include

- triggers PT23, PT26, and PT29, though varying in their definitions, had the same geometrical overlap condition. This feature had been implemented just recently into the data acquisition in November, 2001, and was tested during that beam period. It requires two hits in both the third layer of the FHD and the first layer of the FRH that overlap geometrically. Unfortunately, the timing of this overlap condition led to a late gate signal for the QDC's, resulting in lost energy deposition information. It was impossible to reconstruct any reaction of interest in any of the three samples;

- the two triggers PT20 and PT25. In addition to their hit pattern in the

Forward Detector, both required one charged particle track in the Central Detector (CDC). However, the background in the Central Detector was substantial so that this additional condition had no effect on the selectivity of the trigger.

4.2.1 Selection Rules and Cuts

Prior to analyzing the data, the raw data files are trigger filtered, i.e. the trigger condition in Table 4.5 is set as a selection criteria and a data sample is extracted.

Then, basic checks are carried out to ensure soundness of the examined data sample. These include the test for broken or inoperative detector elements, noisy channels or detector elements with gains extraordinarily high or low.

In the next step, the timing of the event and all hits recorded is processed. The former means that the event has to have a time stamp within the flat top. Additional contraints are put on the hit time of each detector element required for a "valid" track. These ensure that all the hits processed in the reconstruction steps belong to the event that triggered the data acquisition. A time window of ±50 ns is chosen for all plastic scintillators in the Forward Detector and the Plastic Barrel, ±125 ns for the FPC. No time cuts are applied to hits in the CsI crystals in the Central Detector. Tracks combined from the remaining hits are required to have hits in at least the third layer of FHD and the first layer of FRH.

The selection rules and cuts explained in Sec. 4.1.3 are now used to extract the desired type of reaction. Table 4.6 recapitulates these cuts for the reactions $\mathrm{dp} \to \mathrm{dp}\pi^0$ and $\mathrm{dp} \to \mathrm{dp}\gamma$ and states the statistics for each selection level.

Cut description	No. of events $\mathrm{dp} \to \mathrm{dp}\pi^0$	No. of events $\mathrm{dp} \to \mathrm{dp}\gamma$
1. All events	9323699	(100%)
2. Trigger PT22 and cycle time	1170114	(12.5%)
3. "FDCFDC"	801883	(8.6%)
4. "part. id."	64765	(0.69%)
5. "CDN"	13860	(0.15%)
6. γ–π^0 separation	13500 (0.14%)	360 (0.0039%)
7. Missing energy vs. missing mass "MM"	4072 (0.044%)	—
8. "CDNCDN"	2484 (0.027%)	—

Table 4.6: *Selection statistics for the reactions* $\mathrm{dp} \to \mathrm{dp}\pi^0$ *and* $\mathrm{dp} \to \mathrm{dp}\gamma$. *See text for an explanation of the cuts.*

The first row lists the sum of all events counted in all usable runs, i.e. runs 19–22 and 26–27 (cf. Table 4.4). Condition No. 2 has already been explained above. The "FDCFDC" cut just requires exactly two charged particle tracks in the Forward

Detector with an minimum kinetic energy of 25 MeV. It is noteworthy that this cut reduces the event sample by approx. 31%, meaning that only two thirds of the events triggered as "FDCFDC" have two reconstructed charged particle track in the FD. This result and similar ones from other analyses led to an improvement of the "FDCFDC" trigger by requiring geometrical overlap between FWC, FHD and FRH.

The next cut requires the two charged particle tracks to be identified as a proton and a deuteron by ΔE–E method (cf. Sec. 3.3.5). The reduction of this cut is immense, about 93% of the remaining events are discarded. One explanation for this could be the abundance of channels without deuterons in the final state after the "FDCFDC" cut (cf. Table 4.2).

A further large reduction of the remaining experimental data sample of about 83% is attributed to the next cut ("CDN"), where at least one neutral particle with an energy of at least 10 MeV is required in the Central Detector. Comparing the acceptances for the previous and this cut in Table 4.2, the changes are rather small. Thus, the high reduction factor of this cut cannot be explained with the outcomes of the Monte Carlo simulation. Figure 4.9 displays both the squared missing mass (left) and the missing energy vs. squared missing mass (right) distributions for experimental data. In the left picture, the squared missing mass is shown for the remaining events after the particle identification cut (solid line) and the "CDN" cut (dashed line). Clearly, the cut reduces primarily events with too low a missing mass. Since this background cannot be identified with any of the reactions in Table 4.2, it is assumed to originate from unclean experimental conditions, e. g. beam halo.

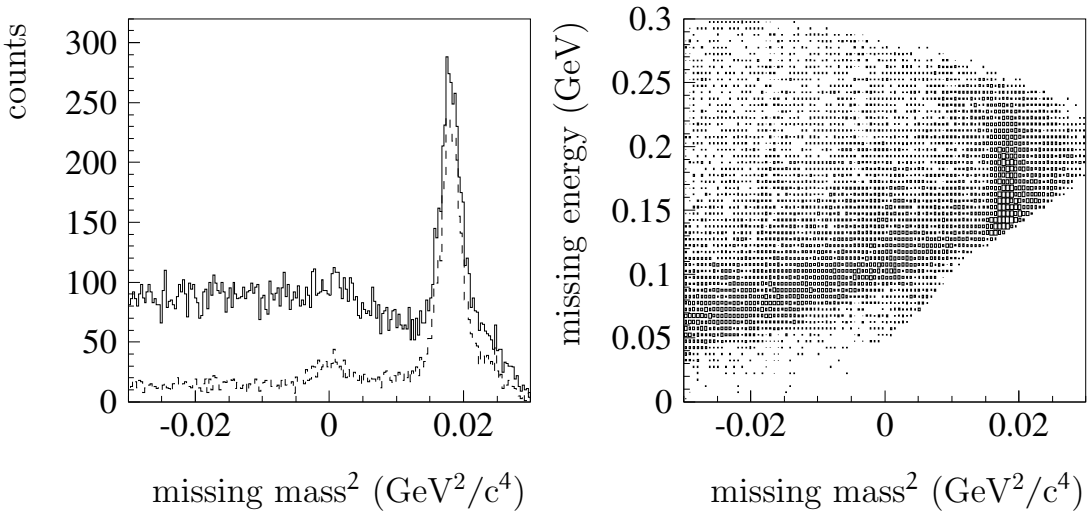

Figure 4.9: *Squared missing mass (left) and the missing energy vs. squared missing mass (right) distributions for experimental data. The solid line in the left picture and the histogram on the right are obtained before the "CDN" cut, the dotted line after its application.*

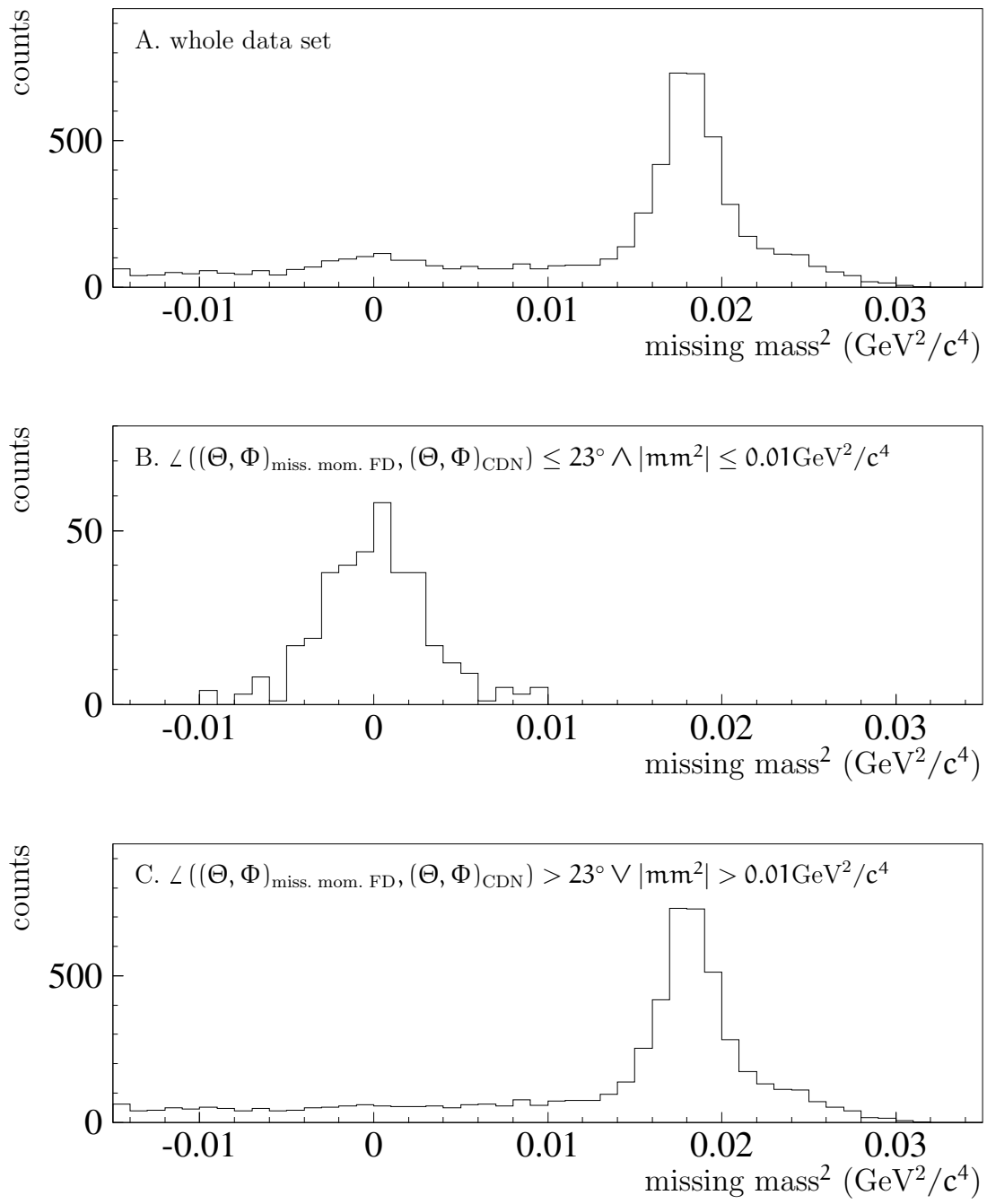

Figure 4.10: *Separation of* $dp\gamma$ *from* $dp\pi^0$ *events. A. shows the squared missing mass distribution for the whole data set. B. is obtained by an angular (cf. Fig. 4.6) and a squared missing mass cut and contains all* $dp\gamma$ *events. C. contains the complement to B. with all* π^0 *candidates and background.*

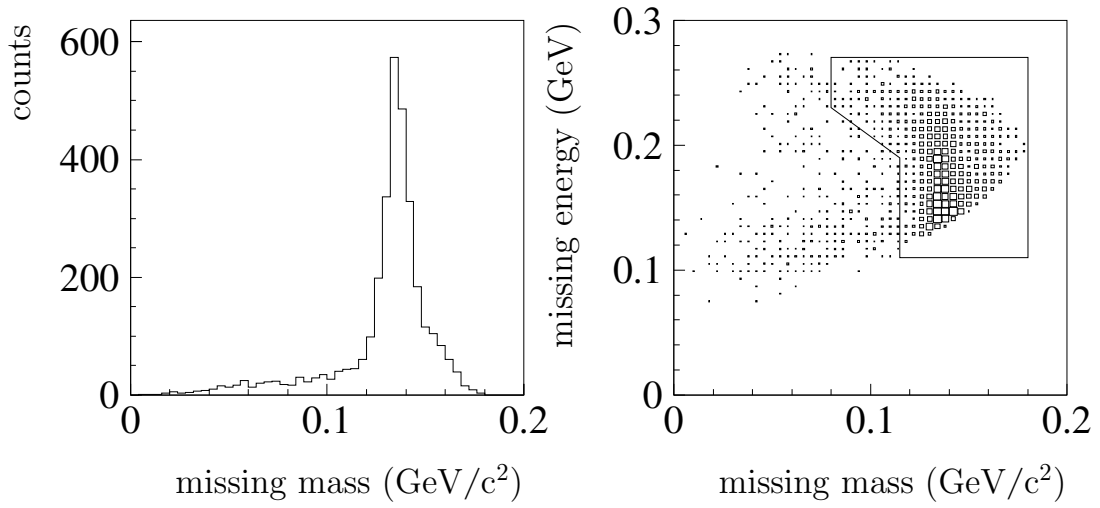

Figure 4.11: *Missing mass spectrum (left) of the remaining experimental data set. The right picture shows the missing mass distribution as a function of the missing energy calculated from the* dp *system. The box depicts the missing mass cut.*

Cut No. 6 separates bremsstrahlung events from $dp\pi^0$ as explained in Fig. 4.6. Figure 4.10 illustrates the effect of this cut on the remaining experimental data sample, of which the squared missing mass distribution is plotted in the first row. The cut on both the squared missing mass and the angle between the missing particle track from the FDCFDC system and the measured CDN track gives the $dp\gamma$ sample in the second row. The distribution in the last row contains the events gained by the negated cut condition.

While this concludes the cuts for the bremsstrahlung reaction, the $dp\pi^0$ sample undergoes another cut to select valid events. This cut on the missing energy vs. missing mass plane has already been explained above (cf. Fig. 4.7). Figure 4.11 shows its application to the experimental data sample.

Finally, the candidates for the reactions $dp \to dp\pi^0$ and $dp \to dp\gamma$ are selected. After the seventh cut ("MM") listed in Table 4.6, 4072 π^0 production events (2484 if cut eight ("CDNCDN") is also required) are left, while 360 bremsstrahlung events remain. This compares to 12480 and 590 events in [G+00] and [G+02], respectively.

4.3 Fitting Procedure

Following the analysis scheme in [Gre99], the two experimental data samples gained so far are analyzed by comparing them with the Monte Carlo data samples generated as described at the beginning of this chapter. The comparison is performed for six observables, viz:

$E_{kin,d}$, Θ_d : the deuteron kinetic energy and scattering angle.

$E_{kin,p}$, Θ_p : the proton kinetic energy and scattering angle.

$|\Delta\Phi_{dp}|$: the planarity of the deuteron–proton system.

$\angle_{dp}$: the opening angle of the deuteron–proton system.

First, the distributions of these observables are extracted from all available samples for a specific reaction. All observables are evaluated in the laboratory system. The distributions of each Monte Carlo model and the experimental data set are stored in arrays:

$r(i,j)$: number of experimentally observed events.

$m_k(i,j)$: number of reconstructed Monte Carlo events for model k with $k = 1$ being the Spectator Model and $k = 2,\ldots,9$ being a coherent contribution according to Table 4.1.

with

$i = 1,\ldots,6$: index of observable.

$j = 1,\ldots,J(i)$: bin of observable distribution i.

By fitting the six experimental distributions $r(i,j)$ simultaneously with all available models $m_k(i,j)$, the relative contribution of each model can be determined:

$$r(i,j) \approx f(i,j) = \sum_{K=1}^{9} c_k \cdot m_k(i,j). \tag{4.8}$$

The resulting function $f(i,j)$ contains the incoherent sum of all models and will be referred to as fit. To find the parameters c_k that describe the experimental distributions best, the $\chi^2(c_k)$ is minimized:

$$\chi^2(c_k) = \frac{1}{I}\sum_{i=1}^{I}\frac{1}{J(i)}\sum_{j=1}^{J(i)}\frac{(r(i,j)-f(i,j))^2}{\sqrt{\delta_r^2(i,j)+\delta_f^2(i,j)}}, \quad r(i,j) > 0. \tag{4.9}$$

The minimization is carried out with the MINUIT package [Jam98] of the CERNLIB. The resulting parameters c_k at the minimum $\chi^2(c_k)$ represent the relative contribution of the different reaction mechanisms to the total cross section of the reaction under study.

4.4 Angular and Energy Distributions

Figure 4.12 shows the six observables defined above for the experimental data set obtained after the "MM" cut. The experimental spectra are compared to the best fit and its contributions from the Spectator Model and the sum of the coherent partial waves.

In the first row, the deuteron spectra for energy and scattering angle are shown. The second row shows the same distributions for the proton. The last row contains the planarity and opening angle of the dp system.

While the angular distributions are smooth, both energy spectra show structures. These are experimental artifacts of two different origins:

- The large dip in the proton energy spectrum at ≈ 0.25 GeV is connected to the FRI hodoscope. Since the energy reconstruction used here does not correct for the 1 cm detector material inserted between the third and forth layer of the FRH, particles stopped in FRI get either a too low or too high reconstructed kinetic energy. The same effect occurs in the deuteron spectrum at around 0.34 GeV. The structure is well described within Monte Carlo and has therefore no influence on the best fit.

- More dips in the proton energy distribution can be seen at 0.2 GeV and 0.15 GeV. These are also connected to the layered structure of the FRH, but in this case the dominating effect is the detector calibration. The dips are caused by protons whose energy is reconstructed with the wrong set of parameters due to a mismatch between the actual stopping plane and the deposited energy measured. These structures would vanish with a better calibration of the FRH. Here, the calibration is limited by poor statistics in the experimental data sets available. However, the impact on the best fit is expected to be small since the events are just sorted into a different bin, causing the small peak between 0.15 and 0.2 GeV.

The proton spectra prove to be most sensitive to the type of model used in the Monte Carlo simulation. For the Spectator Model, the final state proton favors momenta that correspond to half the deuteron beam momentum, thus causing the peak towards higher kinetic energies. These protons are emitted preferably with scattering angles close to zero, causing the peak in the angular distribution towards small angles.

Though the Spectator Model is dominating the observed spectra, it fails to describe the distributions alone. The Spectator Model contribution amounts to 64% here, in comparison to 59% observed in [G+00]. Though this difference can partly be attributed to the different angular range in the WASA setup that gives access to smaller scattering angles as in the PROMICE/WASA detector, the result is still compatible with the previous one within the statistical accuracy. Note, however,

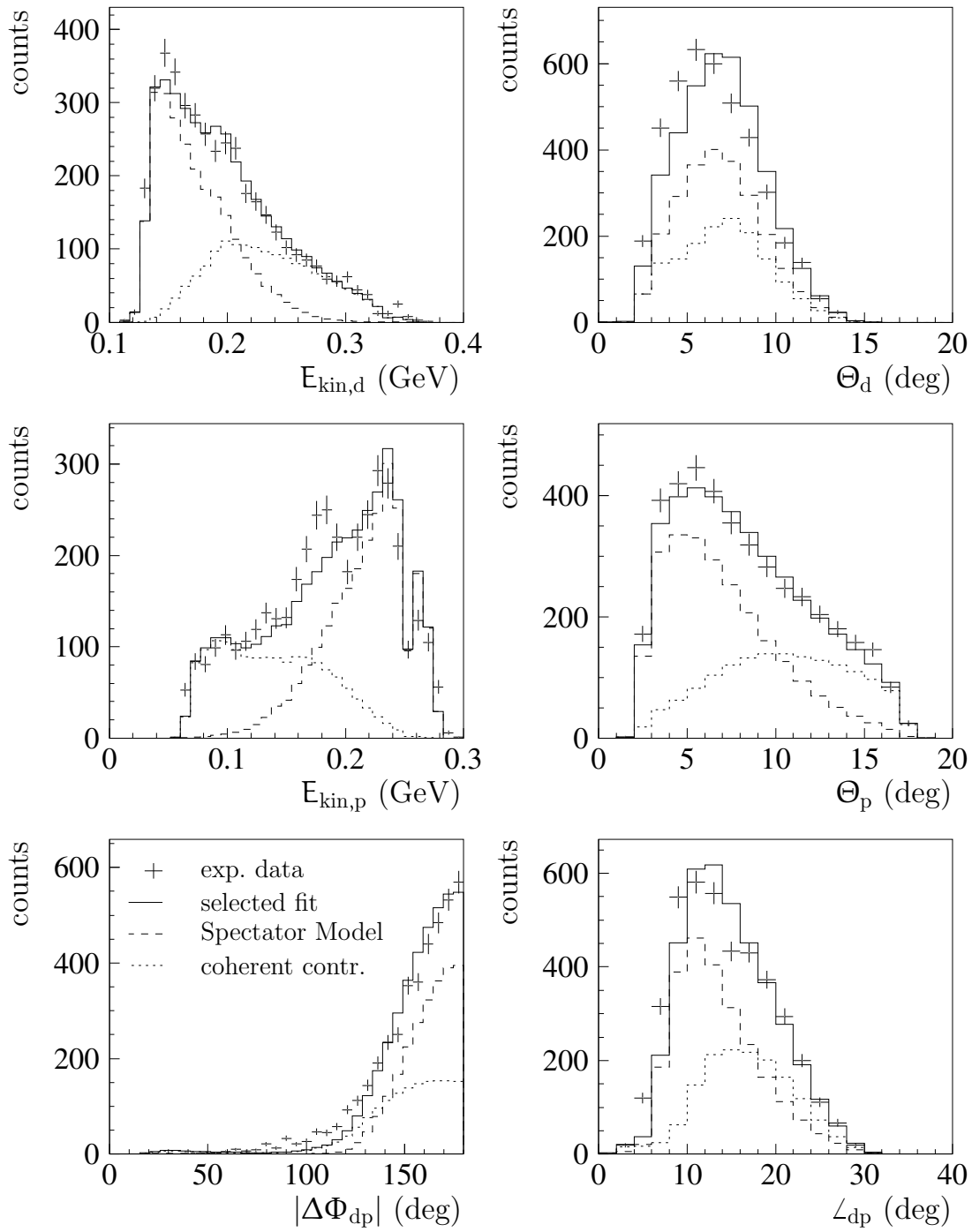

Figure 4.12: *Experimental angular and energy distributions of the* $\mathrm{dp} \rightarrow \mathrm{dp}\pi^0$ *observables after the "MM" cut in comparison to the best fit (solid) composed of the Spectator Model (dashed) and a coherent (dotted) contribution of partial waves.*

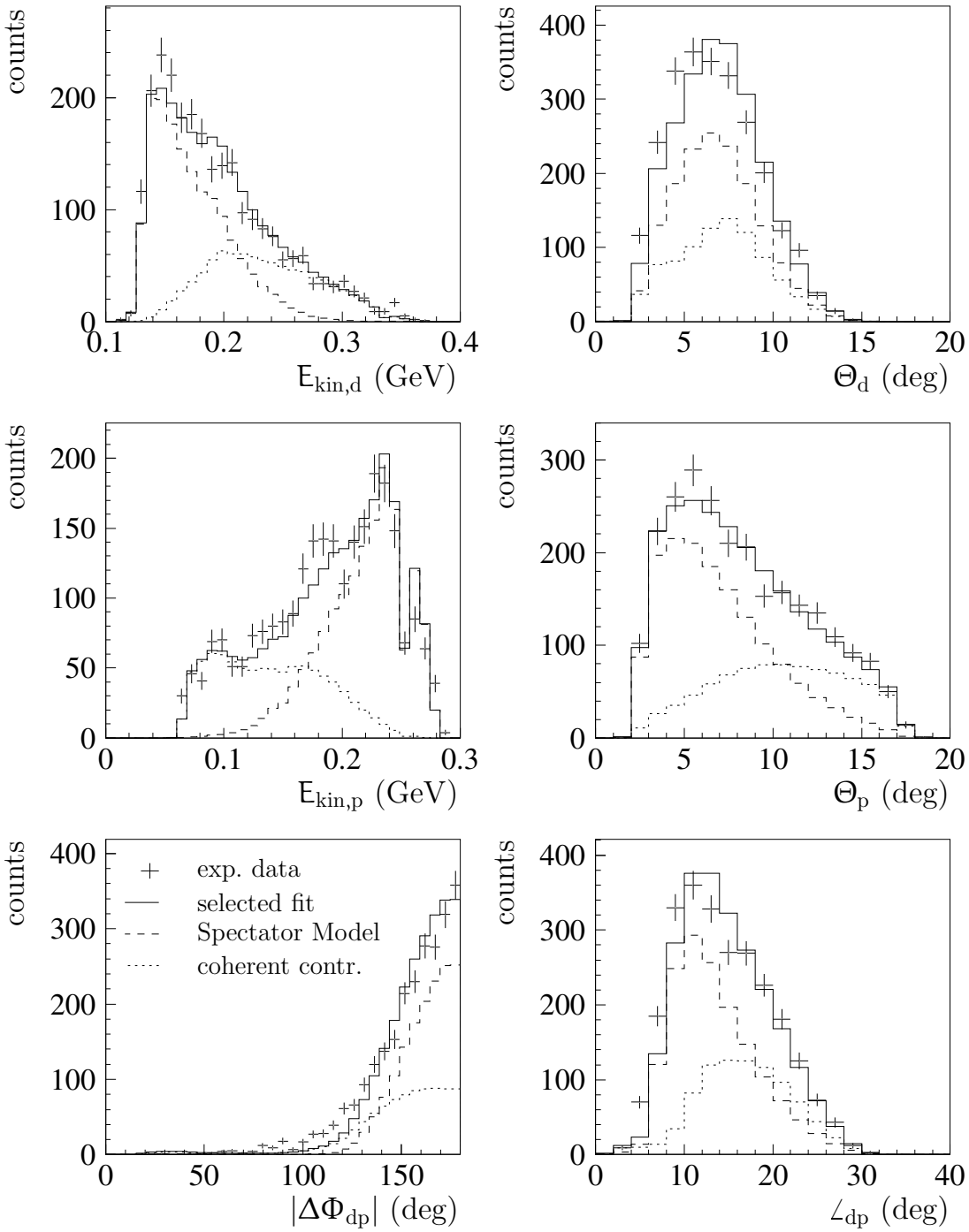

Figure 4.13: *Same as Fig. 4.12 but after the "CDNCDN" cut.*

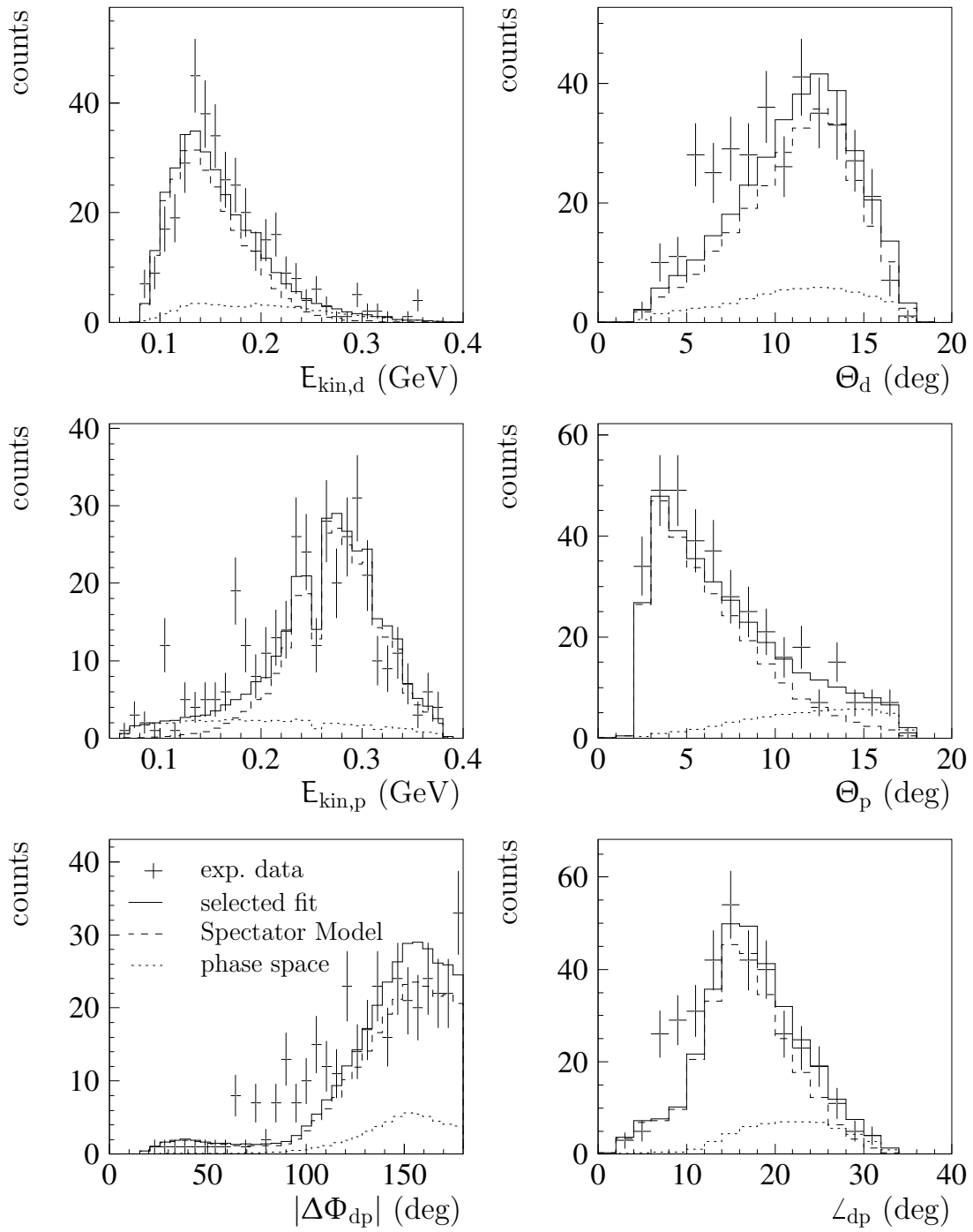

Figure 4.14: *Experimental angular and energy distributions of the* $\mathtt{dp} \rightarrow \mathtt{dp}\gamma$ *observables in comparison to the best fit (solid) composed of the Spectator Model (dashed) and a pure phase space (dotted) contribution.*

that [Gre99] also registered a higher contribution of the Spectator Model (about 74%) when the event was identified by requiring two neutral particle tracks instead of an identified proton in the FD. This gave access to regions of phase space where the proton escaped undetected in the beam pipe. In general, the Spectator Model contribution is more sensitive in regard to the extrapolation towards small scattering angles than the dominant contributions of the coherent mechanism.

The observables of the data set after the "CDNCDN" cut are plotted in Fig. 4.13. Except for the lower statistics, they agree fairly well with the distributions from Fig. 4.12, proving that the additional cut does not introduce any inefficiencies. The best fit here gives a Spectator Model contribution of 66%, being in agreement with the result above within the statistical inaccuracies of around 20%.

Figure 4.14 displays the observables for the $dp \to dp\gamma$ data set. The order is the same as in Figs. 4.12 and 4.13. Again, the experimental data set is compared to the best fit. In the case of the bremsstrahlung reaction, however, a decomposition of the coherent contribution through a partial wave analysis is futile: too many partial waves contribute so far above the reaction threshold. Therefore, only a pure phase space distribution is used to close the gap between the Spectator Model and the experimental results.

Though the sample statistics is rather low, distinct features of the underlying processes are still visible. Both the peak at high proton energies and small proton angles clearly point to a dominant quasifree process as described by the Spectator Model. But as in the case above for $dp \to dp\pi^0$, the Spectator Model is not sufficient to explain the spectra. As already mentioned, the Spectator Model favors protons with half the beam energy. This limits the excess energy in the $d\pi^0$ system, so that the existence of high energy deuterons beyond 0.3 GeV is a clear indication for a process where all three nucleons participate.

The best fit gives a Spectator Model contribution of 66%, which compares to 65% given by [G+02] for the PROMICE/WASA result.

4.5 Phase Space Coverage

The acceptance of the experimental setup can be illustrated best with a Dalitz plot. In the following, the corresponding plots of the WASA experiment to Figs. 4.3 and 4.4 will be given.

For $dp \to dp\pi^0$, the quoted works [Roh94, Gre99] introduced the two variables x and y for the Dalitz plot:

$$x = 100\,\frac{(s_{N\pi} - s_{d\pi}) - (m_N + m_\pi)^2 + (m_d + m_\pi)^2}{s - (m_N + m_d + m_\pi)^2}, \tag{4.10}$$

$$y = 100\,\frac{s_{Nd} - (m_N + m_d)^2}{s - (m_N + m_d + m_\pi)^2}, \tag{4.11}$$

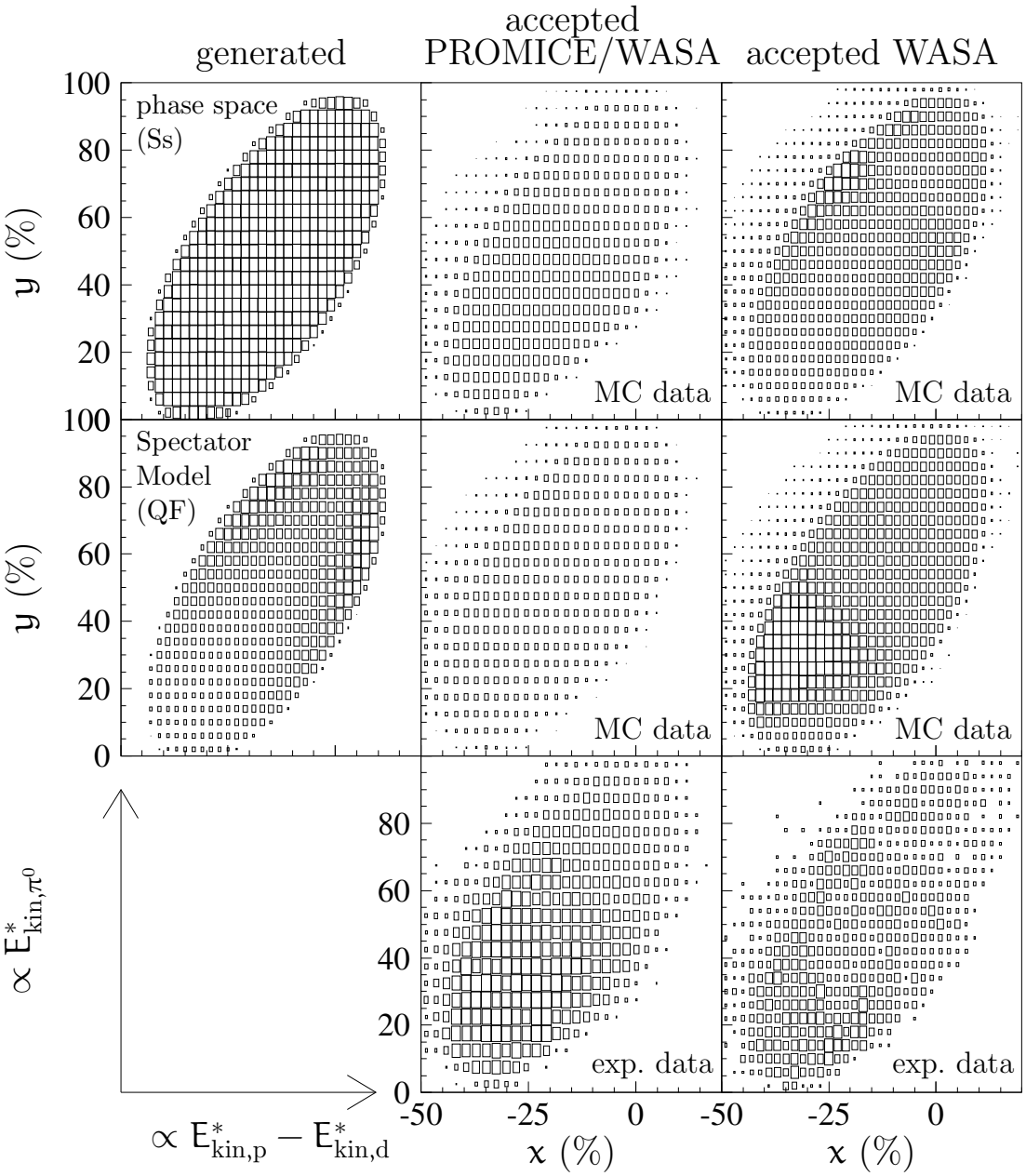

Figure 4.15: *Dalitz plots* $dp \rightarrow dp\pi^0$. *The top two rows are Dalitz plots obtained from Monte Carlo simulations, assuming a pure phase space distribution and the Spectator Model [MN93]. The left column shows the generated distributions, simulated ones including the detector acceptance are shown in the middle for the PROMICE/WASA setup (cf. Fig. 4.4), and the WASA setup on the right. The bottom line shows the experimental data. For the definition of* x *and* y *see text.*

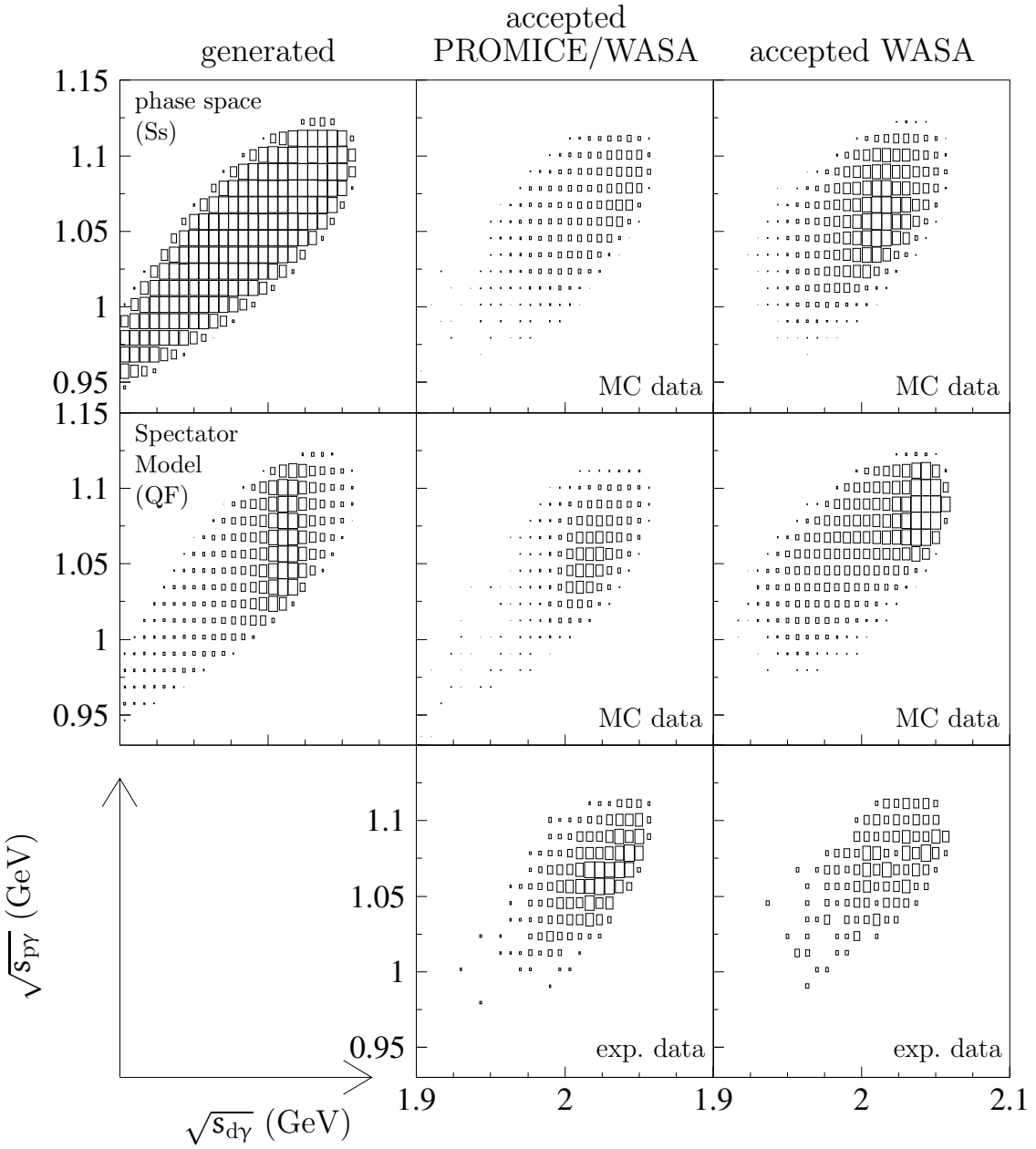

Figure 4.16: *Dalitz plots for* $dp \rightarrow dp\gamma$. *The invariant mass of the* $p\gamma$ *system is plotted as a function of the invariant mass of the* $d\gamma$ *system. The plots are arranged in the same order as in Fig. 4.15.*

with

$s_{N\pi}$: invariant mass of the $N\pi$ system.

$s_{d\pi}$: invariant mass of the $d\pi$ system.

s_{dN} : invariant mass of the dN system.

$m_{N,d,\pi}$: rest mass of nucleon (proton), deuteron, and pion, respectively.

This transformation ensures that the contour in the xy plane of kinematically allowed $dp \to dN\pi$ events is independent of the beam energy. Furthermore, the differences in the particle masses between $dp \to dp\pi^0$ and $dp \to dn\pi^+$ cancel. In [Roh94] and [Gre99], this transformation was needed to compare both reactions measured at different beam energies.

The results for the WASA experiment can be seen in Fig. 4.15. The order of spectra follows the one in the Dalitz plots shown at the beginning of this chapter:

- the first row shows the initially generated Monte Carlo sample for a pure phase space distribution on the left, and the accepted data sample for the PROMICE/WASA (middle) and the current setup (right).
- the second row contains the same Dalitz plots generated with the Spectator Model.
- the last row shows the experimental results from [G+00] and this work.

The larger acceptance of the WASA setup is clearly visible. The statistics is not only higher but also different regions of phase space are more prominent. Especially the region with low x and y in the Spectator Model is highly populated. Nevertheless, WASA also lacks sensitivity where the Spectator Model is expected to be most dominant. That region with high x and y corresponds partly to events with a proton emitted under such small angles that it is lost in the beam pipe.

The same Dalitz plots are shown for $dp \to dp\gamma$ in Fig. 4.16. Here, the invariant mass of the $p\gamma$ system is plotted as a function of the invariant mass of the $d\gamma$ system. Again, the significantly higher acceptance of the WASA setup is easily visible in both statistics and covered phase space. For both reaction mechanisms, the WASA acceptance extends the accessible phase space towards low invariant masses. Still, only a small fraction of the phase space populated by the coherent bremsstrahlung process is accessible. To enlarge that fraction, events with the proton emitted into the Central Detector would have to be included in the analysis (cf. [Sch00]).

4.6 Luminosity and Cross Sections

While the preceding experiment [Gre99] utilized the elastic deuteron–proton scattering to measure the luminosity, that procedure could not be applied here. The cross section for elastic deuteron–proton scattering yields a measurable cross section only for small momentum transfers, otherwise the breakup reaction $dp \to pp n$ dominates. The PROMICE/WASA setup had a set of dedicated silicon detectors placed inside the target chamber that could measure recoil protons with large angles and low energies originating from elastic deuteron–proton scattering (cf. [Koc97]).

Without those silicon detectors or anything similar in the WASA experiment (the MDC had not been commissioned yet), the luminosity is evaluated by using the known cross section for $dp \to dp\pi^0$ from [G+00]. The cross section is given by

$$\sigma = \frac{N_{exp}}{\epsilon L}, \tag{4.12}$$

where N_{exp} is the number of events measured in the experiment for $dp \to dp\pi^0$, ϵ the overall efficiency of the detector system and L the time integrated luminosity. To estimate the efficiency ϵ, a Monte Carlo simulation is carried out, where N_{gen} initial events are generated and N_{rec} events are reconstructed after the simulation. The efficiency is then

$$\epsilon = \frac{N_{rec}}{N_{gen}}. \tag{4.13}$$

After the fitting procedures discussed above, N_{gen} is given by the best fit parameters c_k:

$$N_{gen} = N_0 \sum_{k=1}^{9} c_k, \tag{4.14}$$

with N_0 being the number of initially generated events, i.e. $N_0 = 10^6$ events. Combining Eqs. 4.12 to 4.14 and setting $N_{exp} = N_{rec}$, since we assume that the best fit gives a good description of the experimental results for all observables, gives

$$\sigma = \frac{N_{gen}}{L}. \tag{4.15}$$

The trigger used for $dp \to dp\pi^0$, PT22, has a prescaling factor of $f_{presc} = 80$, which has to be multiplied to the right hand side of Eq. 4.15. Solving for the time integrated luminosity L and replacing it with the luminosity $\mathfrak{L}$ gives

$$\mathfrak{L} = \frac{f_{presc} \cdot N_{gen}}{\sigma \cdot t_{life}}, \tag{4.16}$$

where

$$\mathfrak{L} = \frac{L}{t_{life}}, \tag{4.17}$$

exp. data sample	N_{rec}	N_{gen}	$\mathfrak{L}$ (10^{30} cm^{-2}s^{-1})	L (nb^{-1})
$dp \to dp\pi^0$ "MM"	4072	14407	1.26 ± 0.31	12.81 ± 3.15
$dp \to dp\pi^0$ "CDNCDN"	2484	12753	1.12 ± 0.29	11.35 ± 2.92
[Gre99]	12480	193733	0.82	17.2

Table 4.7: *The luminosity and important parameters of the November, 2001 beam period. The previous results are given for comparison.*

and the life time t_{life}

$$t_{life} = t_{real} \cdot f_{duty} \cdot f_{live}, \tag{4.18}$$

with

$t_{real} = 95520$ s (time elapsed in the laboratory),
$f_{duty} = 28\%$ (accelerator duty factor, cf. Table 2.2),
$f_{live} = 38\%$ (life time factor),
$\sigma = 90 \pm 22$ μb ($dp \to dp\pi^0$ cross section from [G$^+$00].)

Table 4.7 lists luminosity and other parameters from above for the November, 2001 beam period. Also the corresponding numbers from [Gre99] are given. It is noteworthy that the luminosity here is higher than in the previous experiment, though the resulting integral luminosity is less. This can be attributed to the rather small duty factor here of $f_{duty} = 28\%$, while the previous experiment achieved 79%.

The differing statistics of both experiments can be explained, too. Though WASA has a factor of 4.5 higher acceptance than PROMICE/WASA (cf. Table 4.3), a factor of 0.73 less integral luminosity has been measured. Furthermore, the prescaling factor for trigger PT22 is 80, while 8 was sufficient for the previous setup, giving a further factor of 0.1 in disfavor of the work shown here. Combining all factors yields $4.5 \cdot 0.73 \cdot 0.1 = 0.33$, which gives the explanation for the observed ratio between the number of events from both experiments, $\frac{4072}{12480}$.

Using the luminosity obtained from the "MM" sample, the cross section for the second reaction, $dp \to dp\gamma$, can be estimated. Following the argumentation from

exp. data sample	N_{rec}	N_{gen}	$\mathfrak{L}$ (10^{30} cm^{-2}s^{-1})	L (nb^{-1})	$\sigma_{tot,dp\to d\gamma p_s}$ (μb)
[G$^+$02]	590	38485	0.82	17.2	17.9±5.5
$dp \to dp\gamma$	360	1646	1.26 ± 0.31	12.81 ± 3.15	10.3 ± 4.9

Table 4.8: *The total cross section and important parameters of the Nov, 2001 beam period for the reaction* $dp \to dp\gamma$. *The previous results are given for comparison.*

[G+02] and the remarks from Sec. 4.5, a total cross section for both reaction mechanisms fitted in Sec. 4.4 is not given, since the acceptance of the detector towards the coherent reaction mechanism, though higher than in the previous experiment, is still too low. Taking only the Spectator Model contribution, a quasifree cross section $\sigma_{\mathrm{tot,dp}\to\mathrm{d}\gamma\mathrm{p_s}}$ is calculated.

Table 4.8 summarizes the results for $\mathtt{dp} \to \mathtt{dp}\gamma$ and compares the parameters to the previous results. Though the value of $\sigma_{\mathrm{tot,dp}\to\mathrm{d}\gamma\mathrm{p_s}} = 10.3 \pm 4.9\ \mu\mathrm{b}$ is rather low compared to the previous results, both numbers are in agreement within the statistical errors.

Chapter 5

Beam and Target Diagnostics

The examinination of a particle physics detector by analyzing accepted data to extract calibration or input parameters to the experiment, e.g. incident beam energy or detector alignment, is an indispensable procedure to ensure the internal consistency of the whole experiment.

The reaction used in this kind of analysis should be specific to the features under study and well known in its differential distributions; in particular if the detection system is considered not fully explored. Therefore, binary reactions, especially elastic scattering, are chosen for this kind of investigation, wherever applicable. For example, experiments in high energy physics at e^+e^- colliders use Bhabha scattering for monitoring and measuring the luminosity.

At the WASA experiment, the two accessible binary reactions with proton projectiles are the proton–proton (pp) elastic scattering and the pion deuteron production ($pp \to d\pi^+$). Due to kinematics the ejectiles of the latter reaction escape detection at beam energies in excess of approx. 1 GeV, leaving the pp elastic scattering for the following analysis.

This chapter deals with the investigation of the CELSIUS beam and target properties. Section 5.1 explains the selection of pp elastic scattering samples with the WASA detector. Using these samples, the intersection point between the CELSIUS beam and the pellet target, the so–called vertex, is determined in Sec. 5.2. The chapter ends with the analysis of the interaction rate in Sec. 5.3, yielding the luminosities for several beam periods and the calibration of a luminosity monitor.

5.1 Elastic Scattering

For an elastic collision between two particles of equal mass, the final state can be described by the two following relations:

$$|\Phi_1 - \Phi_2| = \pi \tag{5.1}$$

$$\tan\Theta_{1,\mathrm{lab}} \cdot \tan\Theta_{2,\mathrm{lab}} = \frac{1}{\gamma_{\mathrm{cm}}^2} \tag{5.2}$$

Equation 5.1 is the planarity condition whereas Eq. 5.2 is usually referred to as kinematical correlation. The Lorentz factor γ_{cm} describes the movement of the laboratory system with respect to the center of mass systems and can be written as

$$\gamma_{cm} = \sqrt{1 + \frac{T_{lab}}{2m}}, \tag{5.3}$$

with the kinetic energy of the incident beam T_{lab} and the beam particle rest mass m.

The investigations below were all made for a proton beam with $m_p = 938.272$ MeV and a beam energy of $T_{lab} = 1.36$ GeV. Table 5.1 summarizes all the relevant kinematical parameters for this chapter, including the symmetric angle Θ_{sym}, where both protons have the same laboratory scattering angle.

kin. beam energy	$T_{lab} =$	1.360 GeV
inv. mass	$\sqrt{s} =$	2.464 GeV
Lorentz factor	$\gamma_{cm} =$	1.313
symmetric angle	$\Theta_{sym} =$	37.29°

Table 5.1: *Kinematical parameters characterizing the* pp *elastic scattering used in this chapter.*

Besides kinematics, also the dynamical properties of pp elastic scattering are fairly well known, better than for any inelastic nucleon–nucleon reaction in the energy range up to $T_{lab} = 2.5$ GeV. Over the past two decades, it has been measured in several experiments at COSY, the IUCF, or SATURNE. The EDDA experiment located at COSY is particularly worth mentioning since it contributed substantially to several observables of the pp elastic scattering, namely the differential cross section ([EDDA04a]), the analyzing power ([EDDA05]), and some spin correlation parameters ([EDDA04b]). The whole set of available data is compiled in a comprehensive database called SAID [ASW00]. It is accessible via the world–wide web ([SAI04]) and contains in addition the solutions of Partial Wave Analyses, which are utilized in the next section to generate simulated data samples.

5.1.1 Creating and Analyzing Monte Carlo Data

Turning now to the experimental setup at hand, Monte Carlo simulations of pp elastic scattering events provide the understanding necessary to perform the studies outlined further down.

At first, the angular distribution $d\sigma/d\Theta_{lab}$ for the pp elastic scattering at $T_{lab} = 1.36$ GeV is extracted from the SAID database. It is integrated into the GIN event generator as weights to produce a realistic input sample for the Monte Carlo detector simulation. Figure 5.1 shows the GIN produced angular distributions as a

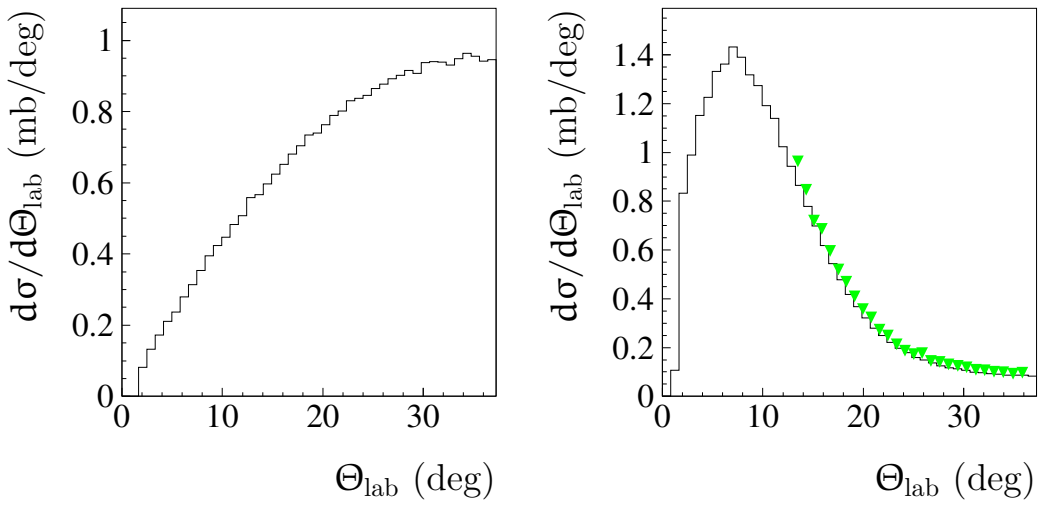

Figure 5.1: *Angular distributions of GIN generated* pp *elastic scattering events at* $T_{lab} = 1.36$ GeV. *The left picture is based on pure phase space, while the right one is weighted with the differential cross section extracted from the SAID database. The superimposed triangles depict data from the EDDA experiment [EDDA04a]. Note, that the phase space distribution follows a* $\sin\Theta$ *dependence since it is plotted as a function of* Θ_{lab}.

function of the laboratory scattering angle Θ_{lab} for pure phase space (left) and the weighted distribution (right). The triangles depict data from the EDDA experiment ([EDDA04a]) at $T_{lab} = 1.328$ GeV. Clearly, the deviation from pure phase space cannot be neglected and has to be taken into account for all Monte Carlo studies.

Selection Rules and Cuts

The Monte Carlo data are classified in three data sets according to the combination of detector parts hit by the ejectiles (Table 5.2).

	forward going proton	backward going proton
A	FD: $\Theta_{lab} = 3° - 18°$	CCD: $\Theta_{lab} = 61° - 85°$
B	FCD: $\Theta_{lab} = 20° - 34°$	CCD: $\Theta_{lab} = 41° - 58°$
C	FCD: $\Theta_{lab} = 35° - 40°$	

Table 5.2: *Detector parts hit by* pp *elastic scattering. FD: Forward Detector, CCD: central part of Central Detector, FCD: forward part of Central Detector.*

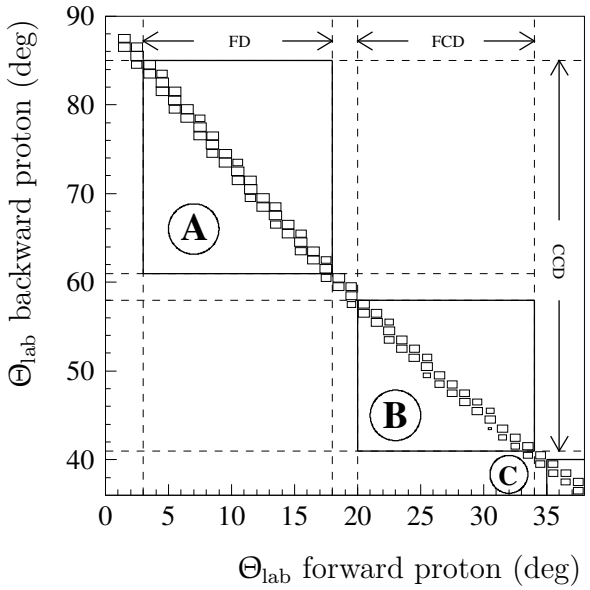

Figure 5.2: *Scattering angle correlation for* pp *elastic scattering at an incident beam energy of* 1.36 GeV. *The boxes show the angular range for samples* ***A***, ***B***, *and* ***C***, *respectively (cf. Table 5.2 and text for further explanation). FD: Forward Detector, CCD: central part of Central Detector, FCD: forward part of Central Detector.*

Figure 5.2 shows the angular correlation of the outgoing protons. The angular ranges defined in Table 5.2 are plotted as colored boxes. From this and Fig. 5.1, one can expect rather low statistics for set **C**, since both the angular range and the cross section are small. Consequently, the analysis focuses on the data sets **A** and **B**.

These are divided into sub-samples by requiring different subdetectors to be present for a valid track in the Central Detector. Because the Plastic Barrel signal is required in the hardware trigger condition (see further down), and since either the SE or MDC is needed to measure the scattering angle of the track, there are two possibilities for the identification of a Central Detector track:

- track must have hits from PS and SE.
- track must have hits from MDC and PS.

This leads to the pp elastic scattering sample classifications listed in Table 5.3.

	PS & SE	MDC & PS (SE opt.)
A	PP1	PP4
B	PP2	(PP5)

Table 5.3: *Classification of different* pp *elastic scattering samples in dependence of the detector layers required for the backward going proton. Sample PP5 is not used due to lack of statistics (see text for explanation).*

The sample **PP5** is not considered since it usually delivers only poor statistics. It requires a track in the forward part of the MDC where the MDC efficiency is found

lacking because the number of layers hit by a charged particle decrease for small scattering angles ([Jac04]). Therefore, it is not used in the following analyses.

To select pp elastic scattering events in the analysis of Monte Carlo data, the analysis starts on the lowest processing level for Monte Carlo, the hit reconstruction. No cuts on either the energy thresholds or the hit times of individual detector elements are applied in the Monte Carlo analysis.

The hits required for a charged particle track in the Central Detector are mentioned above. For a forward track, hits in the Forward Proportional Chamber and all plastic scintillator layers except the Veto Hodoscope are required. Next, limits for the minimum and maximum scattering angle of the forward going proton are applied (cf. Table 5.4). The values listed there differ from the angular ranges given in Table 5.3 to get rid of regions with too low statistics. Additionally, the resulting geometrical acceptance is listed. It is determined as the ratio of initially generated events passing the geometrical cuts to the total number of generated events.

sample	forward going proton	geom.acc.
PP1	FD: $\Theta_{\text{lab}} = 11.5° - 17°$	21.8%
PP2	FCD: $\Theta_{\text{lab}} = 22° - 34°$	8.2%
PP4	FD: $\Theta_{\text{lab}} = 6.5° - 17°$	53.5%

Table 5.4: *Cuts on the scattering angle. FD: Forward Detector, FCD: forward part of Central Detector, geom. acc.: geometrical acceptance.*

Tracks meeting these prerequisites are marked as "valid" or "good" tracks, all others are discarded. At least one good track in both the Forward and Central detector is demanded for an pp elastic scattering event candidate.

Opening angle (Eq. 5.2) and planarity (Eq. 5.1) distributions are plotted for all three pp elastic scattering samples in Fig. 5.3. The planarity distributions (right) peak all at the expected value of 180°, their varying width between 1° and 4° is caused by the different angular resolution of the contributing detectors. The planarity cut is set to three σ around the mean value.

While the planarity of an pp elastic scattering event is a constant, the opening angle is a function of the scattering angle (cf. Eq. 5.2). For this reason, the opening angle distributions are not of normal shape and are not fitted. Instead, the average value for the opening angle as expected from kinematics is taken — 82.5° for samples **PP1** and **PP4**, 75° for sample **PP2** — and a cut of ±7.5° around the average value is chosen. Both the planarity and the opening angle cut are summarized in Table 5.5, for a tabulated summary of all cuts introduced in this section please refer to Tables B.1, B.2, and B.3 in the Appendix B.1.

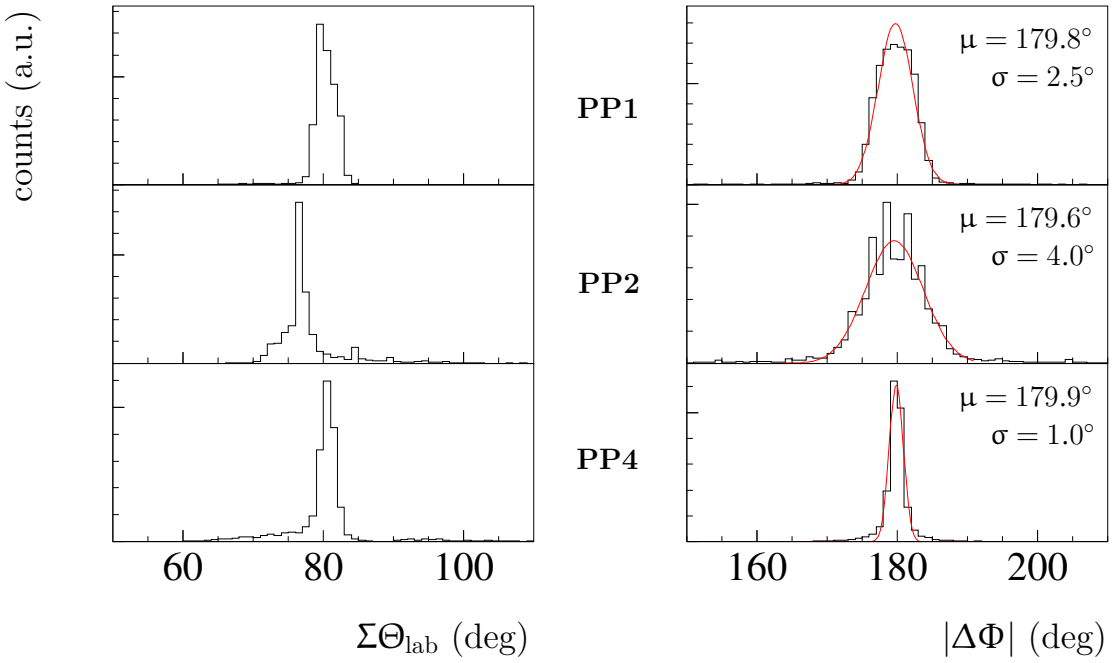

Figure 5.3: *Opening angle (left) and planarity (right) distributions for Monte Carlo data. The values for the mean value* μ *of the planarity and its standard deviation* σ *are obtained from a Gaussian fit (superimposed curve).*

sample	Cut in planarity: $\|\|\Delta\Phi\| - 180°\| \leq 3 \cdot \sigma_{\Delta\Phi}$	Cut in opening angle $\|\Theta_{1,\mathrm{lab}} + \Theta_{2,\mathrm{lab}} - \overline{\Theta}\| \leq 7.5°$
PP1	$\sigma_{\Delta\Phi} = 2.5°$	$\overline{\Theta} = 82.5°$
PP2	$\sigma_{\Delta\Phi} = 4°$	$\overline{\Theta} = 75°$
PP4	$\sigma_{\Delta\Phi} = 1°$	$\overline{\Theta} = 82.5°$

Table 5.5: *Cuts defining valid* pp *elastic scattering events, extracted from Monte Carlo data.* $\sigma_{\Delta\Phi}$ *depicts the standard deviation of the planarity distribution,* $\overline{\Theta}$ *is the average value for the kinematically expected opening angle.*

Detector Inaccuracies

To correct for systematic effects in the measured observables due to misalignment in the detector or the magnetic field of the solenoid, a Monte Carlo analysis is done, comparing event–by–event the reconstructed values for the azimuth and polar angles of both protons with the "true" ones, i.e. the angles given by the event generator GIN.

For this purpose, two pp elastic scattering samples, one simulated without a magnetic field, the other with a field of $\vec{B} = (0, 0, B_z)$, $B_z = 1$ T, are produced and analyzed.

Applying the selection rules above for the former sample, systematic differences between the reconstructed and the expected azimuthal and polar angles are extracted as functions of the reconstructed polar angle (Fig. 5.4). The shown values and error bars correspond to the mean values and the standard deviation of a Gaussian.

The first two rows in Fig. 5.4 show the difference $\Phi_{1,\mathrm{rec}} - \Phi_{1,\mathrm{true}}$ (left) and $\Theta_{1,\mathrm{rec}} - \Theta_{1,\mathrm{true}}$ plotted versus the scattering angle $\Theta_{1,\mathrm{rec}}$, where the index 1 denotes the forward going proton. The same notation holds for the lower two rows, where the corresponding differences are plotted for the backward going proton (index 2). The different symbols depict the samples **PP1** (circles), **PP4** (triangles), and **PP2** (squares), respectively.

While the azimuthal reconstruction (left column in Fig. 5.4) shows only minor or no systematic effects at all, there are significant deviations from zero in the reconstruction of the polar angle (right column). They can be explained as follows:

2nd row: In the forward part of the Central Detector, the CsI crystals do not point directly to the origin of the WASA coordinate system (cf. Fig. 2.14 and [Klo03]). This gives a systematic deviation between the initially generated and the reconstructed value.

3th row: The deviations seen are binning effects. This cannot be avoided, since the angular width of the crystal layers is not constant. (cf. Fig. 2.14).

4th row: The small dip could be connected to a decreasing detection efficiency in the Central Detector. With increasing scattering angle, the energy of the proton diminishes so that it cannot reach the PS anymore.

The situation changes if the simulation is done with a magnetic field of $\vec{B} = (0, 0, 1\ \mathrm{T})$ (cf. Fig. 5.5). Since the track reconstruction does not account for the deflection by the magnetic field (exception: the MDC track reconstruction, see remark below), one expects the reconstructed azimuth angles to differ from the true ones while the polar angles should look the same as above. However, there are two interesting details in Fig. 5.5:

- In the upper left plot, a small dip around $\Theta_{1,\mathrm{true}} = 11^\circ$ can be seen. Since only Forward Detector information is plotted here, both samples show this dip, ruling out any effect in the Central Detector. Also, no kinematical effects can account for this dip. Since the scattering angle is far from the symmetric angle (37.29°), the momentum component perpendicular to the magnetic field is a monotonically increasing function of $\Theta_{1,\mathrm{true}}$. Therefore, the difference $\Phi_{1,\mathrm{rec}} - \Phi_{1,\mathrm{true}}$ is expected to grow continuously with increasing $\Theta_{1,\mathrm{true}}$.
- The left figure in the last row shows a systematic albeit small deviation for the azimuth angle measured with the MDC. This is somewhat surprising, since the

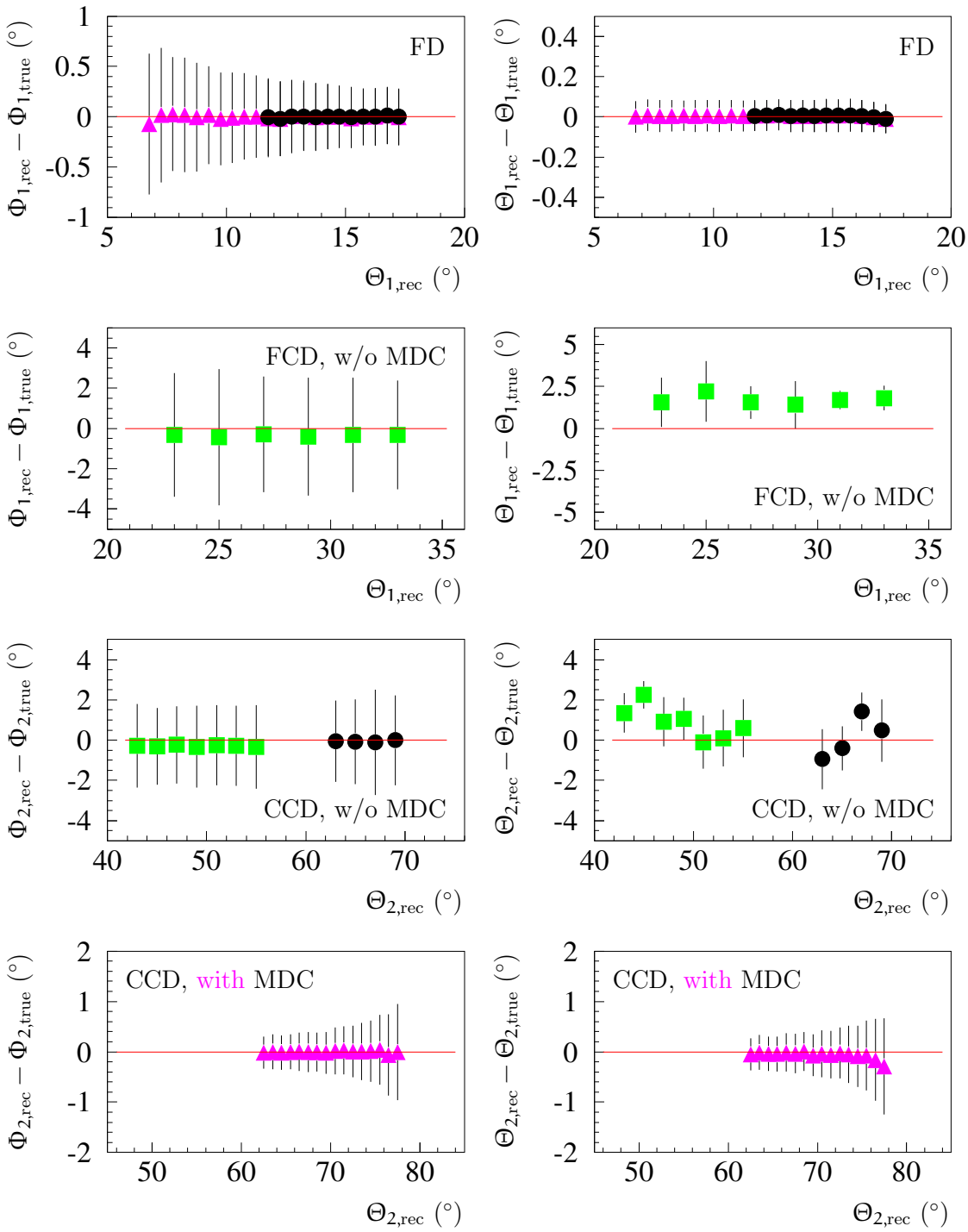

Figure 5.4: *Systematic deviations between reconstructed and true azimuth (left) and polar (right) angles for MC* pp *elastic scattering event samples* ***PP1*** *(circles),* ***PP4*** *(triangles), and* ***PP2*** *(squares) without magnetic field. The index 1 denotes the forward going proton, while index 2 stands for the backward going proton.*

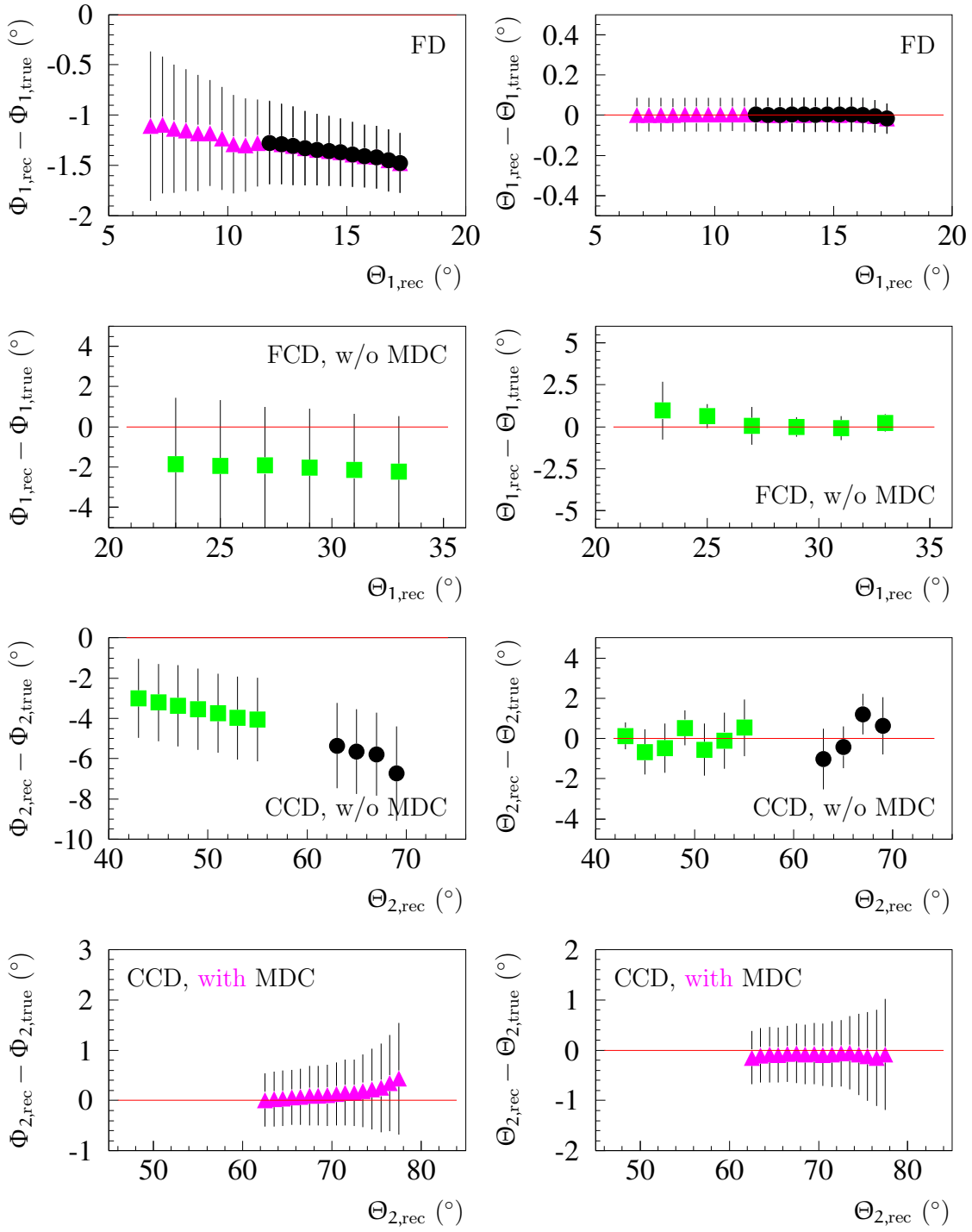

Figure 5.5: *Same as Fig 5.4, but simulated with a magnetic field of* $\vec{B} = (0, 0, B_z)$, $B_z = 1$ T.

MDC analysis takes the magnetic field into account to reconstruct the helical path of the passing particle. The angles thus determined should not show systematical effects originating from the magnetic field.

Though these two effects remain unexplained, in general all observed deviations from the expected behavior remain small within the error bars and thus do not give rise to any serious concern. They are all parameterized and used as correction to the observables in the following analysis steps for both Monte Carlo and experimental data.

It should be noted here that this correction actually depends on the simulated vertex position of the sample used here. However, this dependence is rather small and can be neglected in comparison with the resolution obtained in the following analyses.

Vertex Dependence of the Acceptance

A final Monte Carlo test is carried out to make sure that the analysis procedure does not introduce unwanted systematic effects. Since below the vertex position, i.e. the region of interaction of the incoming beam protons with the hydrogen pellets, is determined, it has to be ensured that the cuts explained above do not bias the result.

Therefore another Monte Carlo sample is generated where the vertex position has been smeared out from -3.5 cm to 3.5 cm in both x and y direction and from -20 cm to 20 cm in z. The above analysis procedure is then used to reconstruct elastic proton–proton events and the initially generated vertex position is plotted in Fig. 5.6

- before the opening angle and planarity cut (stroked line),
- after the planarity cut (dashed line), and
- after both the planarity and the opening angle cut (dotted line).

Though the statistics are reduced greatly, no systematic inefficencies are introduced by the applied cuts in the region that can be reasonably assumed to incorporate the vertex, i.e. $\pm 2 - 3$ cm in every direction.

5.1.2 Selecting and Analyzing Experimental Data

In the scope of this chapter, experimental data taken in several beam periods between December, 2002 and December, 2003 are analyzed. However, the analysis scheme is exemplified on only one data set, since the steps necessary to extract events of the desired type are always the same.

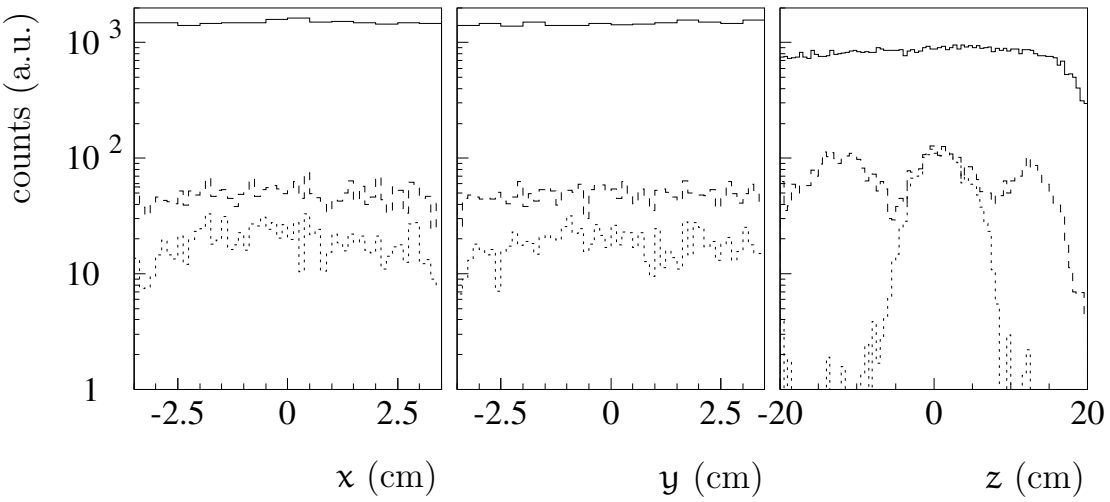

Figure 5.6: *Vertex acceptance for simulated elastic proton–proton scattering before any physics cut (stroked), after the planarity cut (dashed), and after both the planarity and the opening angle cut (dotted). The initial distributions are uniformly distributed.*

Throughout this chapter, all distributions derived from experimental data originate from the beam period in May, 2003. During this period, data at $T_{\mathrm{lab}} = 1.36$ GeV proton beam energy on hydrogen pellets were taken for about 130 h, giving a usable data set of about 94 million events (excluding test and pedestal runs).

Prior to analyzing the data, the raw data files are filtered to reduce computation time of all successive analysis steps. The filter routine selects events that were triggered by a hardware trigger of choice. The hardware triggers used in this chapter are summarized in Table 5.6. The triggers called D1 and DC1 are the main pp elastic scattering triggers being sensitive to sets **A** and **B** in Table 5.2, respectively. The other triggers listed are used for cross checks only.

Trigger name unpres. / pres.	Definition	comment
C1 / D1	1 FRH1 $\wedge$ 1 PSC	trigger for samples **PP1/4**
CC1 / DC1	1 PSF $\wedge$ 1 PSC	trigger for samples **PP2**
AF2 / BF2	1 FRH1	minimum bias trigger for FD
AC14 / BC14	1 PSC	minimum bias trigger for CD

Table 5.6: *Hardware triggers used throughout this chapter.*

Furthermore, basic checks are conducted to ensure basic soundness of the examined data sample. These include the check for broken or inoperative detector elements, noisy signals or detector elements with gains extraordinarily high or low.

Reconstruction Criteria and Efficiency

If the Monte Carlo description of the experimental setup was perfect, the investigation above on Monte Carlo data would be sufficient and the cuts and corrections derived in Sec. 5.1.1, "Selection Rules and Cuts", could be applied without hesitation.

This is, however, not necessarily the case. Therefore, the behavior of experimental data have to be checked and compared to Monte Carlo data and possibly additional corrections need to be imposed on the simulated data sets to reflect the characteristics of the experimental data more closely.

To obtain a clean experimental data sample and to ensure that all the hits processed in the reconstruction steps belong to the event that triggered the data acquisition, additional contraints are put on the hit time of each detector element required for a "valid" track.

To ensure that these time constraints do not cut away valid events, an efficiency study is necessary. To determine the efficiency of one plane to *detect* and *reconstruct* tracks in the Forward Detector, charged particle tracks are selected without this particular detector plane. The number of tracks with hits in this detector plane divided by the total number of tracks is the efficiency of this plane.

A detector element should contain a hit if it has a geometrical overlap with the track coordinates. A hit is defined by the presence of an ADC and TDC entry in the Hit Bank within a given time window.

This study is done on experimental as well as Monte Carlo data to compare how far the behavior of the detector planes examined is described appropriately in the detector simulation. All Forward Detector planes are tested except for the spiral FHD planes, which would require a rather complicated treatment for the geometrical overlap condition.

Figure 5.7 shows the results for a BF2 trigger sample. The detection efficiency is plotted versus the scattering angle of the particle track. Monte Carlo data represented by filled circles are compared to the results of experimental data with different time windows (shown in squares, triangles and open circles).

Examining at first the distributions given by Monte Carlo data, the drop of efficiency towards small angles and at the highest angular bin for some sector shaped detectors is striking. The lower efficiency at the highest angle can be traced back to an edge effect where the particle trajectory does not traverse the whole thickness of the detector plane. For decreasing polar angles, two effects abate the efficiency: First, the ratio between the insensitive gaps between the elements and the active detector area increases. This will be the dominating effect for both the FWC and FHD3. Second, the further a particle penetrates the Forward Detector, the larger are the effects of multiple scattering, thus the decrease in the efficiency from FRH2 to FRH4.

The result for FRH1 is trivial: since FRH1 is part of the trigger condition for

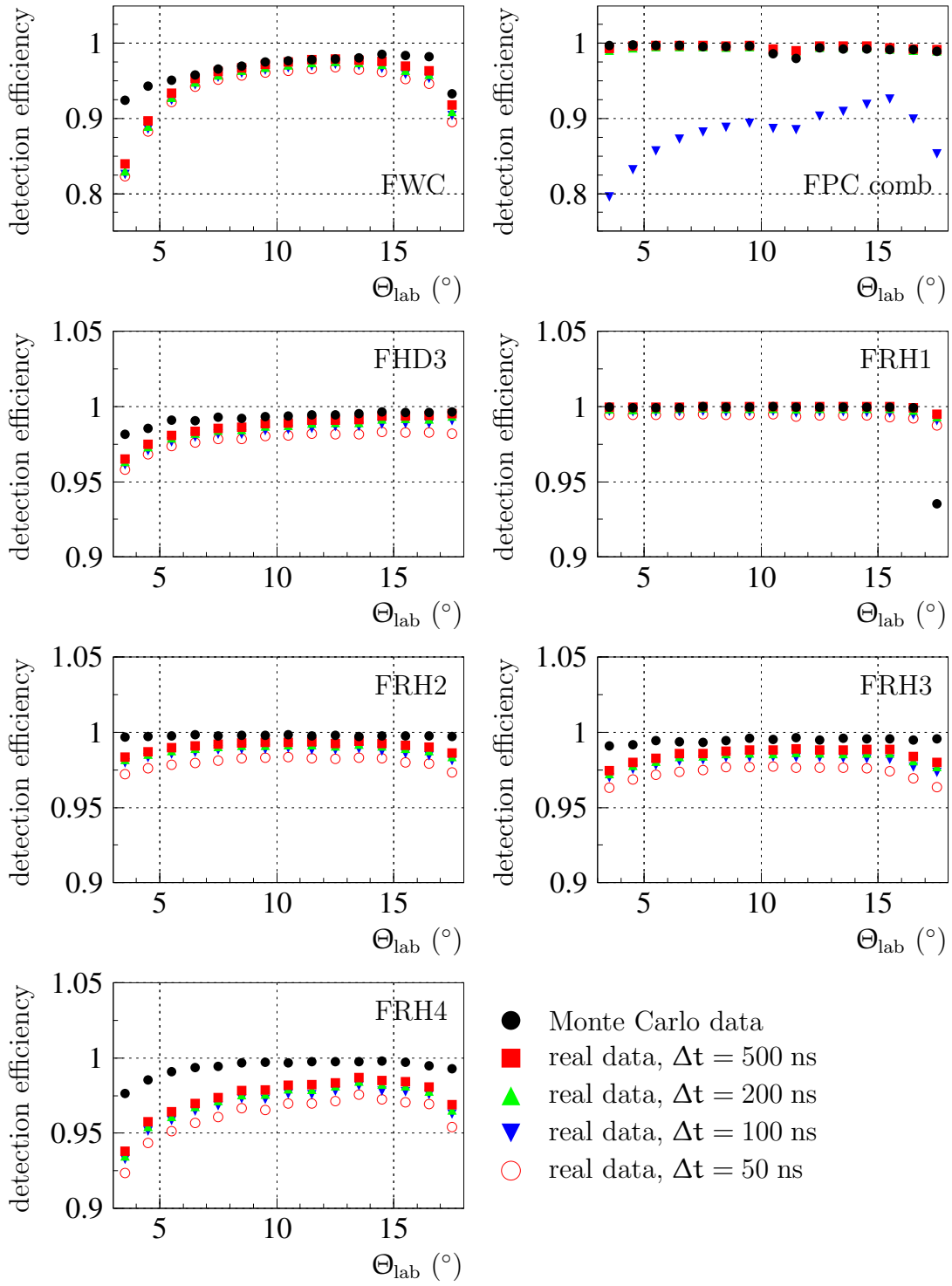

Figure 5.7: *Detection efficiency of a selection of detector planes in the Forward Detector. The time cuts* Δt *mark the time window around the trigger time at* 2000 ns. *Please note the zero suppression in all graphs.*

trigger BF2, the detection efficiency is one within the statistical accuracy, even for the smallest time window. Since this trigger condition is simulated in the Monte Carlo simulation, a constant efficiency is obtained.

The experimental data distributions for the FRH planes two and three and FHD3 show a detection efficiency well above 95% over the whole scattering range and their shapes for the three wider time windows are very well described by the Monte Carlo distributions. The FRH4 and the FWC, though, show large deviations from the simulated spectra, especially towards smaller angles. The deviations amount to almost 10% for the innermost areas of FWC and have to be taken into account in the Monte Carlo reconstruction for a proper detection efficiency correction.

In the case of FPC, the results for a combination of all eight layers has been plotted instead of individual layers. It is labeled FPCcombo and defined as at least one hit in the first FPC module and at least one hit in the second FPC module. This combination ensures that the track has both a x– and y–coordinate measured by the FPC, giving a two dimensional spatial information. As one can see, this combination reacts most sensitive to the different time windows employed. For the smallest time window, the detection efficiency drops to 70% or less and is below the scale of the histogram. For $\Delta t = 100$ ns, the detection efficiency differs significantly from the Monte Carlo efficiency. Also noteworthy is the small dip in the efficiency around $\Theta_{lab} = 11°$. Though the exact origin of the inefficiency is unknown, it explains the dip in Fig. 5.5.

Concluding this analysis, a time window of $\Delta t = 100$ ns is chosen for all plastic scintillators and $\Delta t = 200$ ns for the FPC planes combination. The differences between the Monte Carlo efficiency and the experimental one is included in the Monte Carlo reconstruction.

Physics Cuts

Just like in the case for Monte Carlo data, the last step is to cut on the physical properties of the pp elastic scattering, namely to apply the conditions listed in Table 5.5 after adjusting them to fit experimental data.

Figure 5.8 compares the opening angle and the planarity distributions for simulated and experimental data for all three samples **PP1**, **2**, and **4**. Especially for samples **PP1** and **PP4**, the real data distributions are very well described by the simulated data. Of course, there is still some background contained in the experimental distributions, however, even without any physics cuts, the contamination is rather low.

For samples **PP2**, the simulated distributions are in agreement with the real ones, too, if one takes into account the higher background content.

Using the same argumentation as in Sec. 5.1.1 for Monte Carlo data, the physics cuts for experimental data are extracted and summarized in Table 5.7. It is striking that the angular resolution is somewhat worse for experimental data than in Monte

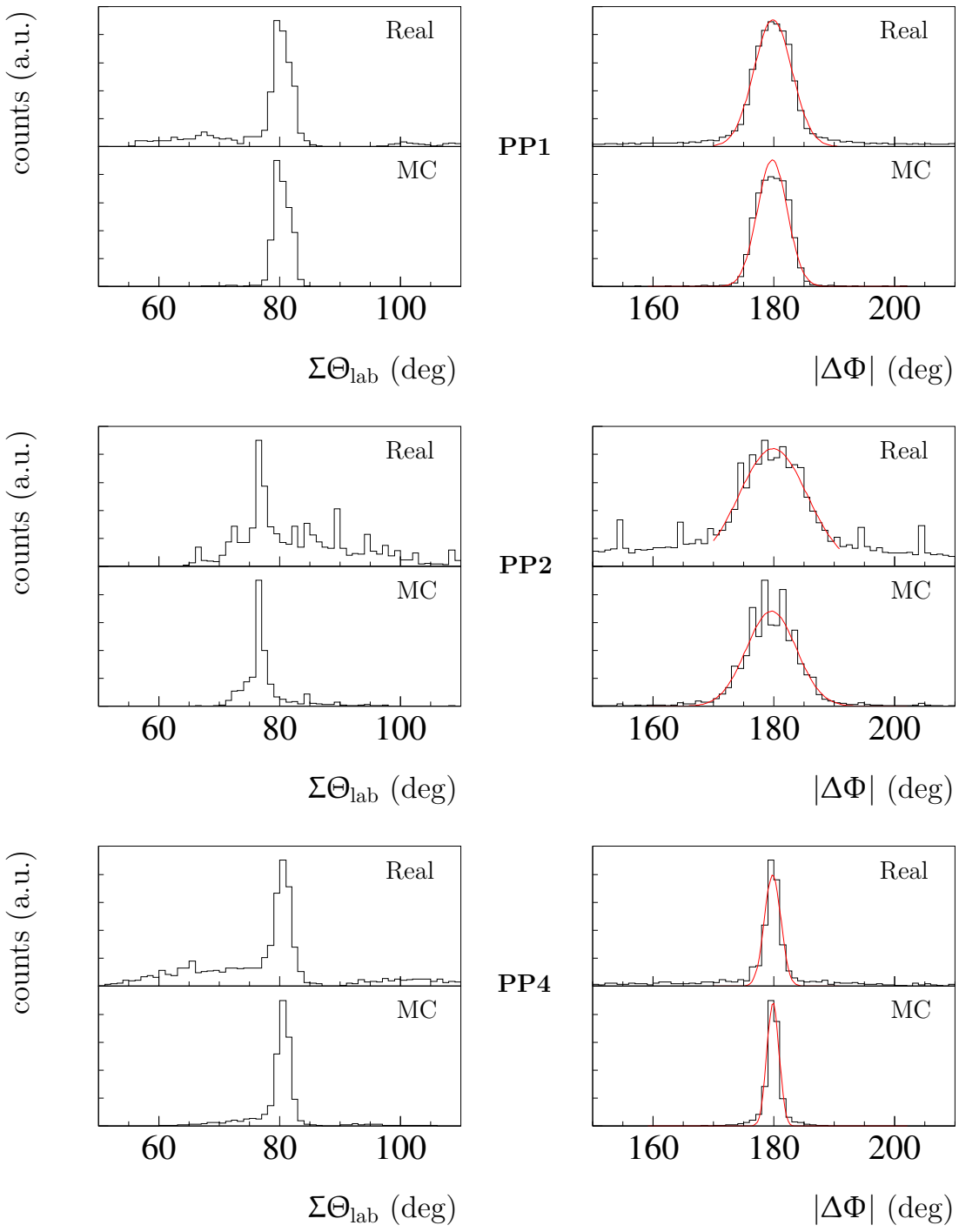

Figure 5.8: *Comparison of the opening angle (left) and planarity (right) distribution for experimental and simulated data prior to the physical cuts. For samples **PP1** and **4**, the real data distributions agree quite well with the Monte Carlo distributions, while for sample **PP2** the background is considerably larger than for the former two samples.*

Carlo. This relates to the fact that the energy resolution, which is not as accurate in experimental data as expected from Monte Carlo, enters through the clustering and track merging into the angular information.

sample	Cut in planarity: $\|\|\Delta\Phi\| - 180°\| \leq 3 \cdot \sigma_{\Delta\Phi}$	Cut in opening angle $\|\Theta_{1,\mathrm{lab}} + \Theta_{2,\mathrm{lab}} - \overline{\Theta}\| \leq 10°$
PP1	$\sigma_{\Delta\Phi} = 3.1°$	$\overline{\Theta} = 82.5°$
PP2	$\sigma_{\Delta\Phi} = 6.0°$	$\overline{\Theta} = 75°$
PP4	$\sigma_{\Delta\Phi} = 1.4°$	$\overline{\Theta} = 82.5°$

Table 5.7: *Cuts defining valid* pp *elastic scattering events, extracted from experimental data.* $\sigma_{\Delta\Phi}$ *depicts the standard deviation of the planarity distribution,* $\overline{\Theta}$ *is the average value for the kinematically expected opening angle.*

All selection criteria imposed on experimental data can be found in the Appendix B.1 in Tables B.4, B.5, and B.6.

To make an estimate of the amount of the remaining background, both the opening angle and the planarity distributions are fitted iteratively with a Gaussian (signal) and a polynomial (background) to separate them.

Figure 5.9 illustrates this method. The left plot shows the planarity distribution obtained with the planarity cut from Table 5.7 for sample **PP1**. The resulting opening angle distribution is plotted on the right. By fitting alternatingly a Gaussian and a second degree polynomial, the function superimposed is deduced as background estimation and can be subtracted from the whole spectrum. The background spectrum ontained this way and the remaining signal spectrum are integrated within the limits given in Table 5.7 for the opening angle cut, which is from 72.5° to 92.5°, and the background to signal ratio is calculated. The results are listed in Table 5.8.

	N_{bkg}	N_{elastic}	$R = \frac{N_{\mathrm{bkg}}}{N_{\mathrm{bkg}}+N_{\mathrm{elastic}}}$
PP1	7946	100770	7.3%
PP2	5585	7312	43%
PP4	107	7546	1.4%

Table 5.8: *Background contamination of all samples after all physics cuts.*

Trigger Efficiency

Now that it has been defined what a proper pp elastic scattering event in experimental data looks like, the trigger efficiency can be estimated.

The trigger efficiency gives the probability that a valid pp elastic scattering event is registered with trigger D1 and DC1, respectively. It parameterizes the performance of the trigger electronics if a set of valid hits is presented to it.

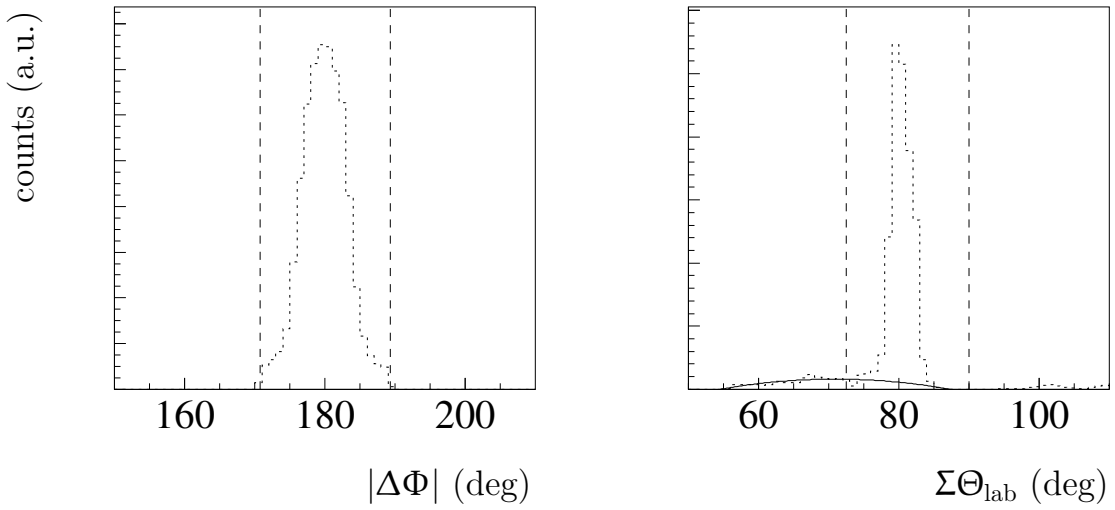

Figure 5.9: *Estimating the background contribution after all physics cuts (here for sample **PP1**): First, the planarity distribution (left) obtained with all cuts (planarity cut: dashed lines) except the opening angle cut is plotted. Then, the resulting opening angle plot (right) is fitted alternatingly a Gaussian and a second degree polynomial, till the background function (superimposed curve) is deduced. Integrating both background and remaining signal within the limits of the opening angle cut (dashed lines) gives the signal–to–background ratio.*

To calculate the trigger efficiency for D1 or DC1, they are compared to a different trigger that fulfills the following conditions:

- It covers at least the same angular range as D1 and DC1, respectively.
- It has a simpler trigger condition so that it can be safely assumed to be close to 100% efficient.

For this purpose, there are usually a few triggers included in the data acquisition system that require only hits in one detector plane and therefore do not need any coincidence condition. Trigger BF2 and BC14 are good examples. The former covers the same angular range in the forward part as trigger D1, while BC14 is part of trigger DC1 which means they fulfill the above requirements.

Figure 5.10 shows the trigger efficiency distribution for D1 using the **PP1** sample selection criteria. It is obtained by analyzing the experimental data set selected with the BF2 trigger condition and checking, how often the unprescaled condition C1, which is the same as D1 except for the prescaling factor, is present. The ratio between these events and the total event number per angular bin gives the plotted distribution.

This calculated trigger efficiency is used to correct the Monte Carlo analysis in the same way the reconstruction efficiency is (compare above).

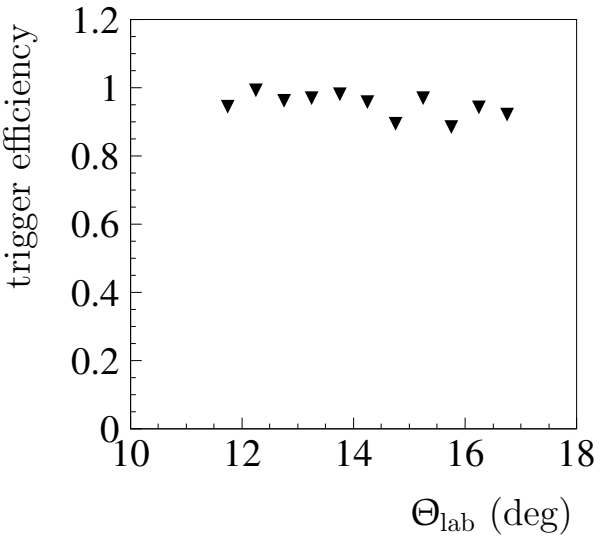

Figure 5.10: *Trigger efficiency distribution of trigger D1 calculated for sample **PP1** selected with trigger BF2.*

5.1.3 Conclusions

The feasibility of simulating and measuring pp elastic scattering with the present WASA detector has been investigated.

Using the known angular distributions from the SAID database, a realistic simulated pp elastic scattering data set can be produced. Analyzing this set shows, that from all possible elastic samples defined by the subdetectors used in the tagging, three samples prove usable. They are used to extract a set of cuts summarized in Tables B.1, B.2, and B.3.

Using the information gained from these samples, pp elastic scattering events are extracted from experimental data. The same procedure as in the simulated case is carried out to determine the cuts necessary to get clean samples. The selection criteria for real data are listed in Tables B.4, B.5, and B.6.

- While sample **PP1** shows a rather small background contamination and reasonably good and clean spectra, it has to be checked if the low spatial resolution of the Central Detector track prohibits the use of this sample for the vertex determination (cf. Sec. 5.2).

- Considering internal consistency, sample **PP2** has an interesting property: since it is based on the Central Detector only, it is not affected by any misalignment between the Forward and the Central Detector. It could have been of use to cross check the other two samples. After the analyses above, though, both the low angular resolution and the high background contamination make this sample unsuitable for any of the studies to follow.

- The sample **PP4** including the MDC shows the best angular resolution in the opening angle and planarity distributions. This is not surprising, since both

track vectors are measured in wire chambers, the FPC in the Forward Detector and the MDC in the Central Detector. Hence, this sample is ideal for the vertex calculations (Sec. 5.2), where only spatial information is needed. However, the better resolution is accompanied with a tremendous increase in computing time, caused by the MDC pattern recognition and final fitting procedures. For pp elastic scattering, the event preselection takes about 60 times longer. For cases, where it is sufficient to have a good angular information on the forward going track only, sample **PP1** is more practical to use.

5.2 The Reaction Vertex

Having thus discussed the venture of simulating and detecting pp elastic scattering with the WASA detector, the gained expertise shall be put into practice. In the following section, the prospects of determining the vertex position, i.e. the region of interaction of the incoming beam protons with the hydrogen pellets, will be assessed. This section is divided into two parts, one of which discusses the position of the vertex in the plane perpendicular to the incident beam, the (x, y)–plane. The second part deals with the vertex position along the beam trajectory which is the symmetry axis for the WASA setup, called z–axis (cf. Fig. 2.4 for the definition of the coordinate system).

Throughout this section, only two samples utilizing the Forward Detector (FD) in combination with the Central Detector (CD) are used: sample **PP1**, requiring hits in the Plastic Barrel (PS) and Electromagnetic Calorimeter (SE) for a valid charged Central Detector track, and **PP4**, which requires hits in the Mini Drift Chamber (MDC) only.

5.2.1 Determining the (x, y)–vertex

Figure 5.11 describes the geometry for the following discussion. Consider a vertex shifted in the (x, y)–plane with regard to the origin which is defined by the Central Detector alignment. The CELSIUS beam is assumed to be parallel to the detector symmetry axis.

An arbitrary pp elastic scattering event is plotted in Fig. 5.11. While the forward going proton p_1 is recorded in the FPC, the MDC measures the momentum vector of prong p_2 (sample **PP4**, sample **PP1** is discussed in Appendix B.6).

The MDC analysis procedure reconstructs the helical path of the particle through the detector. Therefore, the azimuthal angle Φ_2 measured for prong p_2 is independent of the vertex shift, always giving the emission angle Φ'_2, $\Phi_2 = \Phi'_2$. The measured azimuthal angle of the forward going proton Φ_1, however, will deviate from the emission angle Φ'_1.

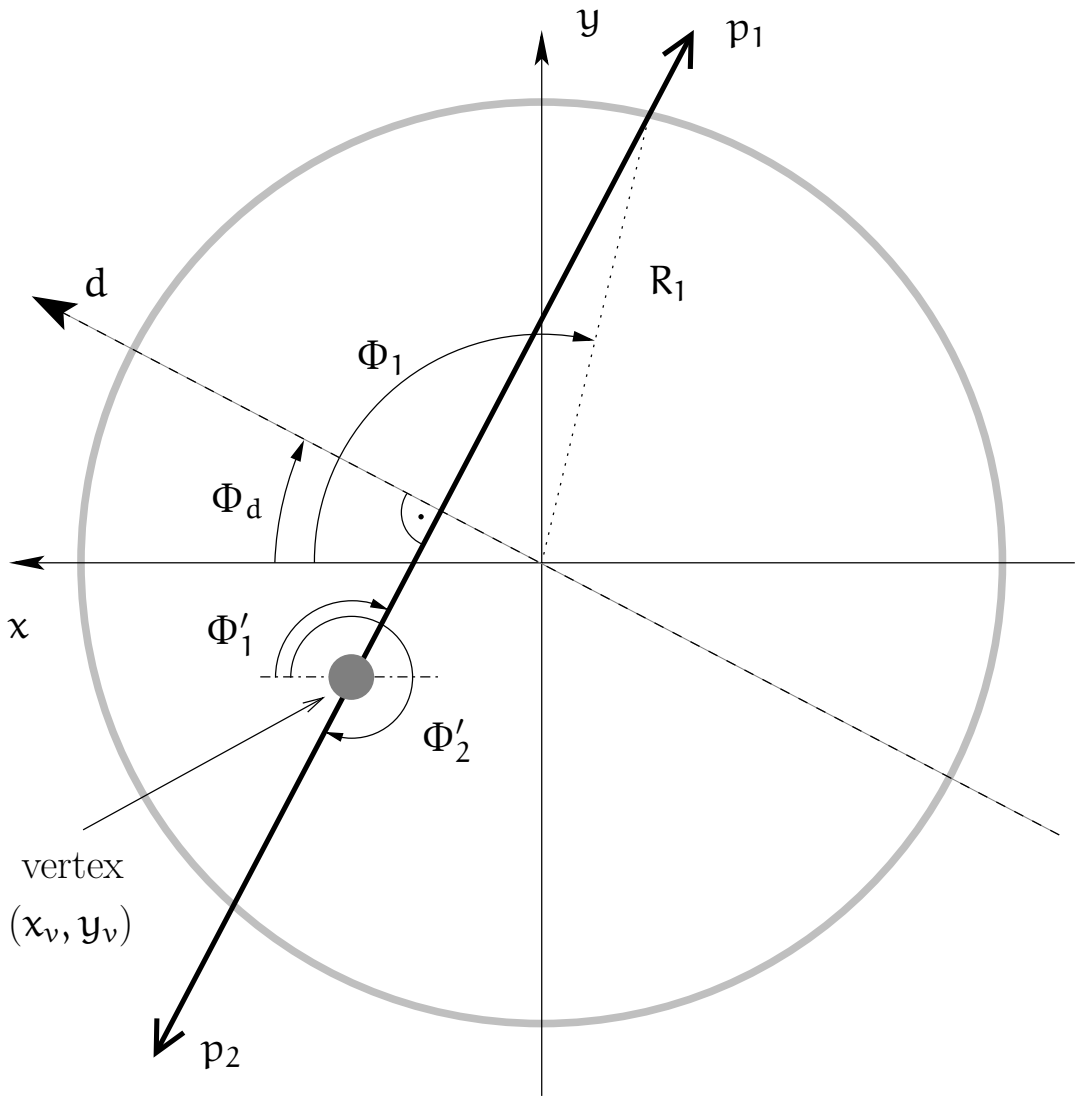

Figure 5.11: *Determining the vertex coordinates x_v, y_v. The (x, y)–plane is shown at $z = 0$ mm, with the z–axis, defined by the incident proton beam, pointing into the plane. p_1 and p_2 depict the projection of the two prongs of a pp elastic scattering event in the (x, y)–plane originating from the vertex (x_v, y_v). While prong p_2 is registered in the MDC, giving the azimuth angle Φ'_2, prong p_1 intersects the FPC at radius R_1. Therefore, its measured azimuth Φ_1 will deviate from the "true" value Φ'_1, thus giving rise to a deviation of $\Phi'_2 - \Phi_1$ from coplanarity. With the newly introduced values d and Φ_d, the deviation is parameterized and utilized to calculate (x_v, y_v). See text for further details.*

On that account, the opening angle $\Phi_1 - \Phi'_2$ will deviate from coplanarity. The discrepancy can be measured in dependence of the true vertex position (x_v, y_v).

In practice, the coplanarity is not directly used to determine (x_v, y_v). Instead, the measured values R_1, Φ_1, and Φ'_2 of both prongs are transformed into a more convenient coordinate system. A perpendicular is constructed on the proton prongs called d, forming a right–angled triangle with prong p_1 and $|R_1|$. The azimuthal angle between d and the x–axis is called Φ_d.

Using the definition of the cosine, d can be written as

$$d = R_1 \cdot \cos(\Phi_1 - \Phi_d), \tag{5.4}$$

and Φ_d is given by

$$\Phi_d = \begin{cases} \Phi'_2 - \dfrac{\pi}{2}, & 0 \le \Phi'_2 \le \pi \\ \Phi'_2 - \dfrac{3\pi}{2}, & \pi \le \Phi'_2 \le 2\pi \end{cases}, \tag{5.5}$$

with $\Phi_d \in [-\frac{\pi}{2}, \frac{\pi}{2}]$.

With the new parameters (d, Φ_d) the beam position can be calculated as

$$d = x_v \cos \Phi_d + y_v \sin \Phi_d \tag{5.6}$$

by using basic trigonometric relations (cf. Appendix B.5).

The radius R_1 varies with the scattering angle since the detector that "registers" the proton, the FPC, is a plane perpendicular to the z–axis. R_1 is given by

$$R_1 = Z_{FPC} \cdot \tan(\Theta_{FDC}). \tag{5.7}$$

To assure that these assumptions are reasonable the whole procedure is first tested with Monte Carlo data.

Monte Carlo Tests

To avoid any bias in the coplanarity distribution, the cut on coplanarity is omitted in this section. All other cuts described in Sec. 5.1.1, "Selection Rules and Cuts", are applied correspondingly and d and Φ_d are calculated for each remaining event. Dividing the range of Φ_d ($[-\frac{\pi}{2}, \frac{\pi}{2}]$) into 18 intervals, the events are sorted according to their Φ_d value. In this manner, 18 spectra with d–distributions are accumulated. Then, the integral of each spectrum is normalized to one and fitted by a Gaussian

$$n(d) = \frac{1}{\sqrt{2\pi}\sigma_d} \exp\left(-\frac{(d - \bar{d})^2}{\sigma_d^2}\right), \tag{5.8}$$

with two fit parameters $\bar{d}$ and σ_d. For given Φ_d the parameters can be calculated with

$$\bar{d} = x_v \cos \Phi_d + y_v \sin \Phi_d \tag{5.9}$$

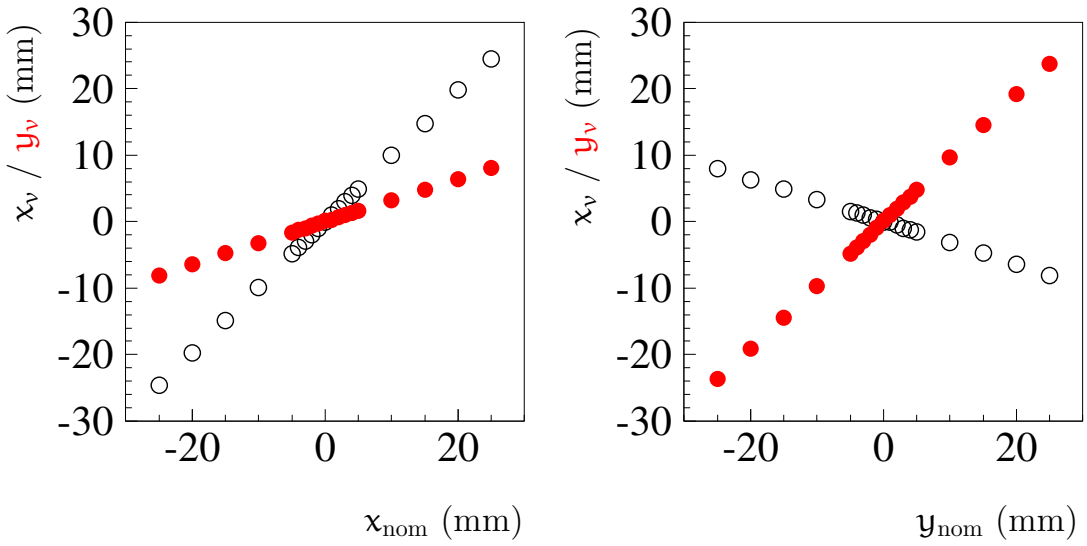

Figure 5.12: *Results of the fit routine for* x*–shifted (left) and* y*–shifted (right) Monte Carlo samples. The resulting coordinates* x_ν *(rings) and* y_ν *(circles) are plotted as functions of* x_{nom} *(left) and* y_{nom} *(right).*

and

$$\sigma_d = \sqrt{\sigma_{x_\nu}^2 \cos^2\Phi_d + \sigma_{y_\nu}^2 \sin^2\Phi_d + \sigma_{\Phi_d}^2 (y_\nu \cos\Phi_d - x_\nu \sin\Phi_d)^2}. \tag{5.10}$$

The d–distributions for the two bins centered at $\Phi_d = -5°$ and $5°$ tend to have lower statistics then the other bins. Though they are included in the subsequent plots, they are excluded from the overall fit. The remaining spectra are fitted simultaneously with the five fit parameters $x_\nu, y_\nu, \sigma_{x_\nu}, \sigma_{y_\nu}, \sigma_{\Phi_d}$ using the MINUIT minimization package of the CERNLIB program library.

Figures B.1, B.2, and B.3 show d–distributions for simulated vertices at $(-20, 0)$, $(0, 0)$, and $(20, 0)$ respectively. The superimposed curve represents the fit function Eq. 5.8.

The results for the fit parameters for the unshifted and all x– and y–shifted samples are shown in Fig. 5.12. The fitted x_ν (rings) and y_ν (circles) coordinates are plotted as a function of x_{nom} for the x–shifted samples (left) and y_{nom} (right) for the y–shifted samples. While the fitted values of the shifted variable reproduce the nominal shift well, the other variable differs significantly from the expected value zero.

The situation becomes even clearer if the nominal coordinates and the fitted coordinates are plotted in Fig. 5.13. The fitted coordinates seem to be rotated with respect to the nominal ones.

Therefore, the following ansatz is made to transform the fit results into the ex-

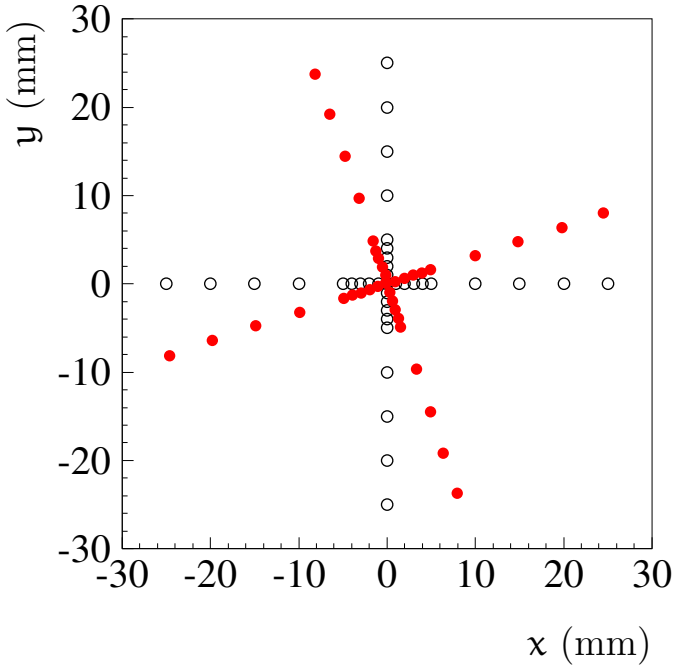

Figure 5.13: *Nominal (rings) and fitted (circles) vertex position in the (x, y)–plane. The resulting coordinate system of the latter can be mapped to the nominal one with Eq. 5.11.*

pected values

$$\begin{pmatrix} x_{nom} \\ y_{nom} \end{pmatrix} = k \cdot \begin{pmatrix} \cos\varphi & \sin\varphi \\ -\sin\varphi & \cos\varphi \end{pmatrix} \begin{pmatrix} x_v \\ y_v \end{pmatrix}, \tag{5.11}$$

introducing also a scaling factor k which is expected to be one.

By fitting the above expression to the results in Fig. 5.13 the two parameters k and φ are determined to be

$$k = 0.9755$$
$$\varphi = 18.26^\circ$$

The rotation arises from the magnetic field, which is tested by simulating a sample without a magnetic field. As already mentioned in Sec. 5.1.1, "Checking the Observables", the magnetic field corrections applied to the angles prior to the fitting are only valid for the unshifted sample. To test if the rotation in Eq. 5.11 is a function of the simulated displacement the rotation was determined using only samples with the same absolute shift in x and y. Table 5.9 shows the result of this test. Apparently, the spread is small enough to assume a constant rotation factor.

This method should be insensitive to any displacement in the z–direction since only the projections of the two prongs into the (x, y) are used. This assumption is tested by applying the whole procedure to samples shifted along the z–axis. As expected, the resulting vertex positions (x_v, y_v) agree with $(0, 0)$.

$\lvert x_v\rvert$, $\lvert y_v\rvert$	k	φ (°)
25	0.9789	18.45
20	0.9748	18.11
15	0.9740	18.21
10	0.9710	18.26
5	0.9753	18.12
4	0.9788	18.26
3	0.9689	18.42
2	0.9781	17.06
1	0.9846	14.17

Table 5.9: *The rotation angle and the scale factor from Eq. 5.11 as a function of the simulated shift.*

Experimental Data

Since the procedure works well with Monte Carlo data, it is applied to experimental data. The available data set is divided into two samples, the first containing data from runs 27–37, the second runs 38–52. Check Sec. 5.1.2, "Physics Cuts", for selection criteria applied to the data set. Again, the coplanarity cut is not used.

Figures B.4 and B.5 show d–distributions for runs 27–37 and 38–52, resp. Again, the fit function Eq. 5.8 is shown as a superimposed curve. The outcomes of both fits are listed in Table 5.10. Using Eq. 5.11 to correct for the magnetic field, the resulting vertex position are:

$$\begin{aligned} &\text{May, 2003, runs 27–37:} && (x_v, y_v) = (-2.3 \pm 1.3, -1.6 \pm 1.2)\,\text{mm} \\ &\text{May, 2003, runs 38–52:} && (x_v, y_v) = (-2.2 \pm 1.3, -1.3 \pm 1.2)\,\text{mm} \end{aligned} \tag{5.12}$$

The results for the (x, y)–vertex are comparable to the recent results from [Jac04], where $(x_v, y_v) = (0 \pm 0.4, 0 \pm 0.5)$ mm. However, the deviation from the nominal position $(0, 0)$ is significant.

x_v (mm)	y_v (mm)	σ_{x_v} (mm)	σ_{y_n} (mm)
May03, runs 27–37			
−1.7±1.3	−2.3±1.2	6.5±2.2	6.2±1.9
May03, runs 38–52			
−1.7±1.4	−2.0±1.2	6.8±2.2	6.5±1.9

Table 5.10: *Uncorrected results for the real data set from the May, 2003 beam period.*

5.2.2 Determining the z–vertex

Figure 5.14 illustrates the geometry of this exercise. It shows a longitudinal cross section through the WASA detector in the plane defined by two outgoing prongs p_1 and p_2 of an arbitrary pp elastic scattering event. The vertical hatched box depicts the FPC, the hatched horizontal boxes symbolize the layers of the MDC. The CELSIUS proton beam (coming from the left, not shown) is assumed to line up with the detector symmetry axis.

Calling the scattering (polar) angles of each prong Θ'_1 and Θ'_2, respectively, the "kinematical correlation" of pp elastic scattering (cf. Eq. 5.2) can be written as

$$\tan\Theta'_1 \tan\Theta'_2 = \frac{1}{\gamma_{cm}^2} = (1 + \frac{T}{2m_p})^{-1} \tag{5.13}$$

for an incoming proton (rest mass m_p) beam with kinetic energy T.

Again, the information gained from both prongs acts differently for a shifted vertex along z. While the MDC directly measures the angle at emission point Θ'_2, the measured angle in the FPC, Θ_1, defined by the intersection points of the prong p_1 with the detector plane, will deviate from the emission angle Θ'_1, if the reaction vertex does not coincide with the origin but is displaced along z by z_v. The relation between those two angles can be calculated geometrically, yielding

$$\frac{1}{\tan\Theta'_1} = \frac{1}{\tan\Theta_1}(1 - \frac{z_v}{Z_1}), \tag{5.14}$$

with the distance of the FPC from the origin Z_1. Replacing $\tan\Theta'_1$ in Eq. 5.13 with Eq. 5.14 gives

$$1 + \frac{T}{2m_p} = \frac{1}{\tan\Theta_1}(1 - \frac{z_v}{Z_1})\frac{1}{\tan\Theta'_2}, \tag{5.15}$$

and solving for $\tan\Theta'_2$ results in

$$\tan\Theta'_2 = \frac{1 - \frac{z_v}{Z_1}}{\tan\Theta_1(1 + \frac{T}{2m_p})}. \tag{5.16}$$

Thus, by plotting the angular correlation Θ'_2 vs. Θ_1, the unknown z_v can be extracted.

Monte Carlo Tests

For all Monte Carlo samples with shifted z–vertex the cut on the opening angle (cf. Sec. 5.1.1, "Selection Rules and Cuts") is omitted to avoid any bias on the kinematical correlation. The remaining events are sorted according to their Θ_1 value

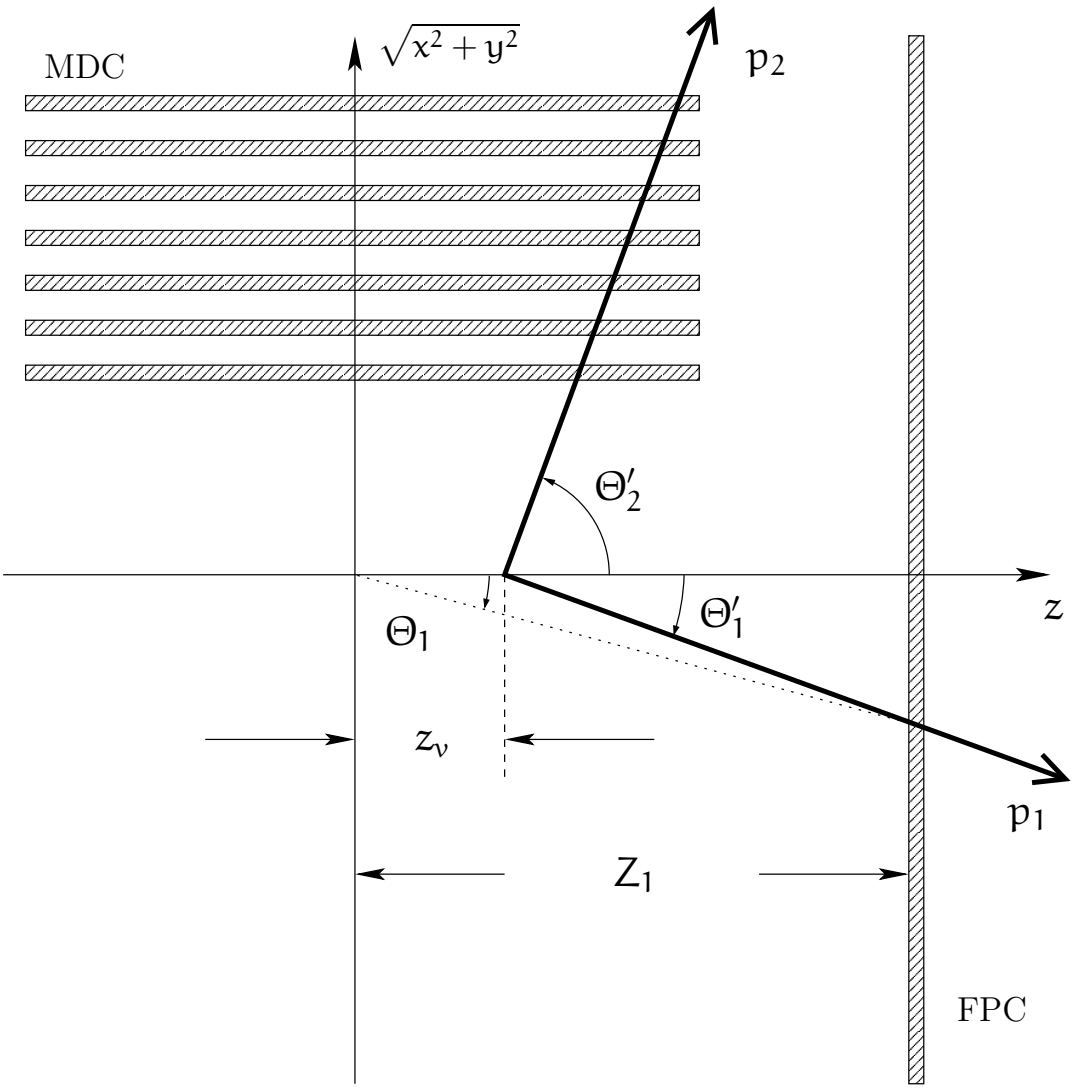

Figure 5.14: *Determining the z–vertex. A longitudinal section along the plane defined by the two prongs p_1 and p_2 of a pp elastic scattering event is shown. The two prongs are registered at their intersection points with the FPC and the MDC planes. Due to a shift of the reaction vertex z_v along the z–axis, the measured scattering angle Θ_1 will deviate from the emission angle Θ_1'. See text for further details.*

in 40 intervals between 0° and 20°, accumulating Θ'_2 distributions in dependence of Θ_1.

Not all distributions are filled or accumulate sufficient statistics for fitting. Therefore, only 23 spectra in the range $6.5° \leq \Theta_1 \leq 18°$ are chosen, normalized to one and fitted by a Gaussian

$$n(d) = \frac{1}{\sqrt{2\pi}\sigma_{\Theta'_2}} \exp\left(-\frac{(\Theta'_2 - \overline{\Theta}_2)^2}{\sigma^2_{\Theta_2}}\right), \tag{5.17}$$

with two fit parameters $\overline{\Theta}_2$ and σ_{Θ_2}. For a given Θ_1 the parameters can be calculated with

$$\overline{\Theta}_2 = \tan^{-1}\left(\frac{1 - \frac{z_v}{Z_1}}{\gamma^2_{cm}\tan\Theta_1}\right), \tag{5.18}$$

with $\gamma^2_{cm} = 1 + \frac{T}{2m_p}$ and

$$\begin{aligned}\sigma_{\Theta_2} = &\left(\frac{\cos\overline{\Theta}_2}{\gamma^2_{cm}\tan\Theta_1}\right)^2 \\ &\cdot\sqrt{\left[\sigma_z\frac{\gamma^2\tan\Theta_1}{Z_1}\right]^2 + \left[\sigma_T\frac{\tan\Theta_1(1-\frac{z_v}{Z_1})}{2m_p}\right]^2 + \left[\sigma_{\Theta_1}\frac{\gamma^2_{cm}(1-\frac{z_v}{Z_1})}{\cos^2\Theta_1}\right]^2}.\end{aligned} \tag{5.19}$$

The spectra are fitted simultaneously with the fit parameters $T, \sigma_T, z_v, \sigma_z, \sigma_{\Theta_1}$ using the MINUIT minimization package of the CERNLIB program library. The parameters T and σ_T are fixed to the values,

$$T = 1.36\ \text{GeV}, \sigma_T = 1\ \text{MeV}.$$

Figure B.6 displays the obtained Θ'_2–distribution for the unshifted sample together with the results of the fit procedure as superimposed Gaussians.

In Fig. 5.15, the fit results are plotted against the nominal z values. The fitted values z_{fit} do not give the nominal values, but rather seem to be displaced by an offset of about −5 mm. To get a rough correction function, a linear function is fitted to the data points, depicted by the dashed line. The function (cf. Eq. 5.20) can be used to calculated the true vertex z_v from the fitted values.

$$z_v = 1.07 \cdot z_{fit} + 5.90\,\text{mm} \tag{5.20}$$

Experimental Data

Again, the two experimental data samples from the beam period in May, 2003 are analyzed. As above, the opening angle cut is ignored, otherwise all cuts in Sec. 5.1.2, "Physics Cuts", are applied as described.

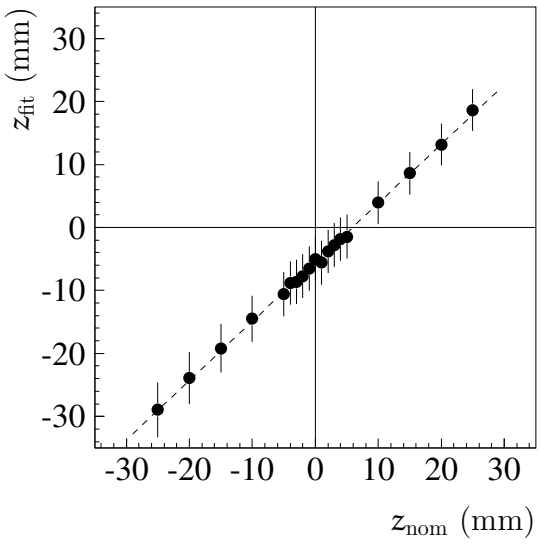

Figure 5.15: *Results of the z–vertex Monte Carlo tests. The resulting fitted values z_{fit} are plotted as functions of the nominal shift z_{nom}. The dashed line depicts a linear fit to the data points (cf. Eq. 5.20).*

Furthermore, the vertex position in the (x, y)–plane as determined in Sec. 5.2.1 is used to correct the angular information of the reconstructed protons. This is necessary since a displacement along the (x, y)–plane changes the measured value for the forward scattering angle Θ_1.

Table 5.11: *Uncorrected results for the real data set from the May, 2003 beam period.*

z_v (mm)
May03, runs 27–37
-12.3 ± 6.4
May03, runs 38–52
-14.5 ± 6.9

Figures B.7 and B.8 show Θ_2'–distributions for runs 27–37 and 38–52, respectively. The fit function Eq. 5.17 is superimposed. The outcomes of both fits are listed in Table 5.11. Correcting those values by applying Eq. 5.20, the vertex position along z is found to be:

$$\begin{aligned} &\text{May, 2003, runs 27–37:} \quad z_v = (-7.3 \pm 6.8)\,\text{mm} \\ &\text{May, 2003, runs 38–52:} \quad z_v = (-9.6 \pm 7.4)\,\text{mm} \end{aligned} \tag{5.21}$$

While the results for the (x, y)–vertex are comparable to the already mentioned results from [Jac04] — $(x_v, y_v, z_v) = (0 \pm 0.4, 0 \pm 0.5, 6.9 \pm 6.8)$ mm — the z–position seems to be shifted in the opposite direction. To investigate this further, the procedure described in [Gre01] is used.

There, the vertex position along z is determined by using Eq. 5.2 to calculate γ_{cm}^2 for each z–shifted Monte Carlo sample above and both real data samples. By fitting the real γ_{cm}^2–distribution with the ones obtained from the Monte Carlo samples, relative weight factors are extracted that are used to calculate the mean vertex position.

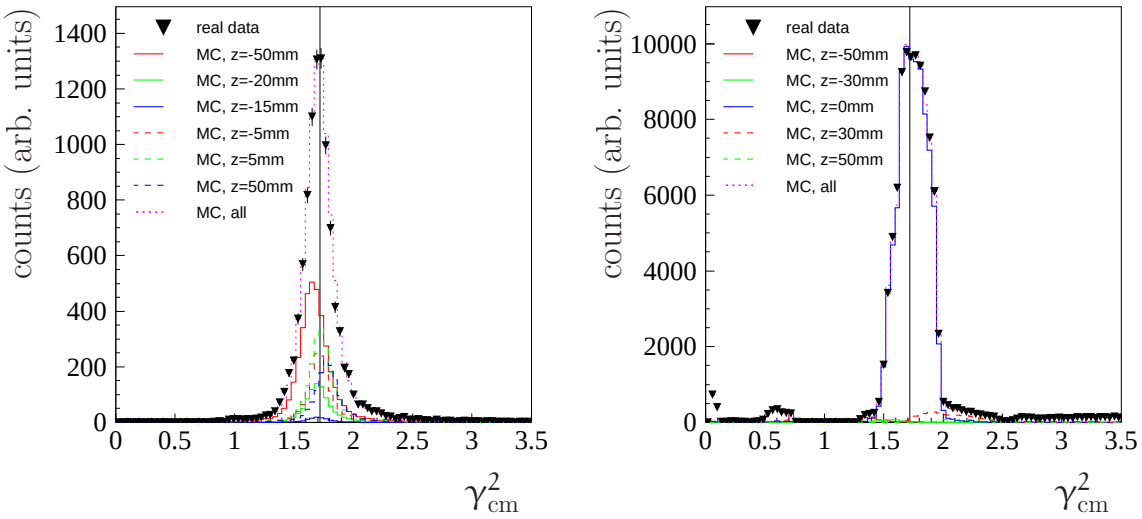

Figure 5.16: γ^2_{cm}*–distributions for data from May, 2003, runs 38–52 (black crosses), sample* ***PP4*** *(left) and sample* ***PP1*** *(right). The superimposed colored histograms are distributions from Monte Carlo samples with indicated shift fitted to the real data distribution. The vertical black line indicates the nominal* $\gamma^2_{cm} = 1.72$ *at* $T_{lab} = 1.36$ GeV.

In [Gre01], only sample **PP1** could be used, since the MDC had not been commissioned yet. Here, the procedure can and is applied to both samples.

Figures B.9 and B.10 show Monte Carlo distributions of γ^2_{cm} for samples **PP4** and **PP1**, respectively. Due to the higher angular resolution for the Central Detector track, the distributions in sample **PP4** are smooth and show no significant structures. In fact, γ^2_{cm}–distributions for **PP4** do not seem to change at all with the variation of the z–vertex. The explanation is simple: since the angular information for the Central Detector track in sample **PP4** comes from the MDC, it is independent of the z–vertex. Thus, only the angle of the forward going track changes with different simulated z positions resulting in a rather low sensitivity of sample **PP4** for the z–vertex when compared with sample **PP1** in the context of the method described here.

Keeping this in mind one can turn to the real data distributions and the fit results, shown in Fig. 5.16.

The nominal value for γ^2_{cm} at $T_{lab} = 1.36$ GeV is 1.72. This value is reproduced by the real data distributions of both samples rather well indicating a z–vertex around zero. This fact is reflected in sample **PP1** where the Monte Carlo sample at $z = 0$ contributes most to the composition of the real distribution. The weight factors and the resulting z–vertex positions are given in Table 5.12. While the sample **PP1** gives -1.6 mm, agreeing fairly well within the errors with the above observation and the being more compatible with the result from [Jac04], sample **PP4** gives -17 mm, a

	sample **PP4**	sample **PP1**
$z = -50$ mm	45.7%	6.7%
$z = -30$ mm	0	1.5%
$z = -20$ mm	6.4%	0
$z = -15$ mm	1.1%	0
$z = -5$ mm	14.0%	0
$z = 0$ mm	0	86.1%
$z = 5$ mm	19.0%	0
$z = 30$ mm	0	4.0%
$z = 50$ mm	13.8%	1.7%
resulting z	-17 mm	-1.6 mm

Table 5.12: *Result for the vertex distribution fit for both **PP4** and **PP1** sample.*

value even smaller than the result in Eq. 5.21. It must be concluded that there is a large systematic error of unknown origin in the **PP4** sample.

With the weight factors from Table 5.12 it is tempting to draw conclusions about the z–vertex distribution. Besides the main contributions around $z = 0$ mm, there are small ones coming from $z < -30$ mm and $z > 30$ mm (sample **PP1**). This could be interpreted as an indication for events that originate far away from the nominal position of the pellet target. However, if one includes Monte Carlo samples with higher displacement, e.g. $z = 60$ mm (cf. Fig. 5.17, left) and $z = 70$ mm

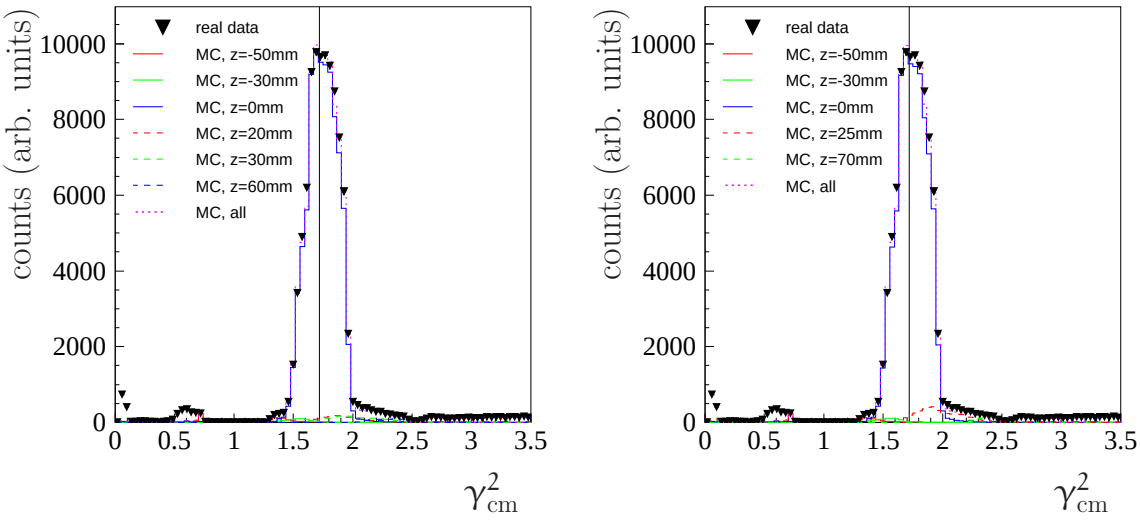

Figure 5.17: *γ^2_{cm}–distributions for data from May, 2003, runs 27-37 (black crosses), sample **PP1**, including Monte Carlo samples with $z = 60$ mm (left) and $z = 70$ mm (right). The fit favors the Monte Carlo samples with highest displacement to describe the tails of the distribution from real data.*

(cf. Fig. 5.17, right), the samples with the highest displacement are favored by the fit to describe the tails of the real data γ^2_{cm}–distribution. Therefore, the composition of the z–vertex distribution remains unclear.

5.2.3 Conclusion and Further Improvements

A method to determine the displacement of the reaction vertex has been introduced. It consists of two steps. In the first, the shift in the plane perpendicular to the incident beam is determined by measuring the deviation of the sample's planarity from 180°. After correcting for this shift, the vertex position along the z–axis is extracted by calculating the sample's deviation from the scattering angle correlation.

Tests with Monte Carlo data show that the vertex position can be reconstructed, yielding uncertainties

- σ_{x_v} and σ_{y_v} of less then 2 mm, and
- σ_{z_v} of less than 5 mm.

The errors are given by the maximum standard deviation observed for the Monte Carlo fit results displayed in Figs. 5.13 and 5.15. They are interpreted as systematic uncertainties of the methods described.

While the results for the (x, y)–vertex are compatible with recent results from [Jac04] — $(x_v, y_v, z_v) = (0 \pm 0.4, 0 \pm 0.5, 6.9 \pm 6.8)$ mm — the z–position differs significantly.

Using an alternate procedure described in [Gre01] for the determination of z_v, the conclusion is reached that the method described in Sec. 5.2.2 suffers from an unknown but large systematical error. The alternate procedure gives a z–vertex close to $z = 0$, which brings it closer to the result from [Jac04], but still the deviations are significant and cannot be explained by the statistical inaccuracies involved. Running the analysis on experimental data sets from May, 2003, results in the following vertex positions:

$$\begin{aligned} &\text{runs 27–37:} \quad (x_v, y_v, z_v) = (-2.3 \pm 1.3, -1.6 \pm 1.2, -2.0 \pm 1.2) \text{ mm} \\ &\text{runs 38–52:} \quad (x_v, y_v, z_v) = (-2.2 \pm 1.3, -1.3 \pm 1.2, -1.6 \pm 1.2) \text{ mm} \end{aligned} \tag{5.22}$$

In principle, this analysis can be extended to take into account a beam being tilted with respect to the z–axis. This would require sampling a broader scattering angle range by including the **PP2** sample into the analysis (cf. [Roh95]).

Furthermore, also the beam energy could be determined here. The beam energy has been set to the nominal value throughout this analysis. Usage of the momentum information from the MDC for the backward proton, however, would make it possible to include the beam energy into the fitting process in Sec. 5.2.2.

An improvement of the analysis shown here can be expected when the third layer of the Forward Proportional Chamber (FPC) and the drift time information of all

three FPC layers are included in the analysis framework. However, more dramatical enhancements would be achieved by improving the spatial resolution of the MDC.

5.3 Luminosity

Now that the interaction position is known, the pp elastic scattering shall be used to determine another basic parameter in particle physics experiments: the luminosity.

This section first relates the quantity luminosity to the experimental observables. Then the method of how the luminosity can be determined in the WASA experiment is discussed by using sample **PP1**. Finally, results over several beam periods are presented.

5.3.1 Definition

The cross section for any reaction measured in a beam–target–collision experiment is given by

$$\sigma = \frac{N_{exp}}{\epsilon L}, \tag{5.23}$$

where N_{exp} is the number of events measured in the experiment for the investigated reaction, ϵ the overall efficiency of the detector system and L the time integrated luminosity. The latter is a measure for the extent of the beam–target overlap and expresses the intensity of the beam–target interaction.

Usually, the cross section σ or the angular distribution $\frac{d\sigma}{d\Omega}$ are the quantities to be measured in scattering experiments. Therefore, the luminosity is a prerequisite for absolute values. However, the situation may be reversed for a determination of L, which is an important parameter when judging the performance of an experimental setup in particle physics, too.

5.3.2 The Method

In this chapter, the luminosity is calculated using the pp elastic scattering sample **PP1**. First, the selection rules described above are applied to extract pp elastic scattering events from the examined experimental data set. For the resulting sample, the angular distribution $N_{pp}(\Theta)$ is plotted. To extract the "true" angular distribution $t_{pp}(\Theta)$, $N_{pp}(\Theta)$ has to be corrected for

- the overall efficiency and
- remaining background events.

The overall efficiency is the product of

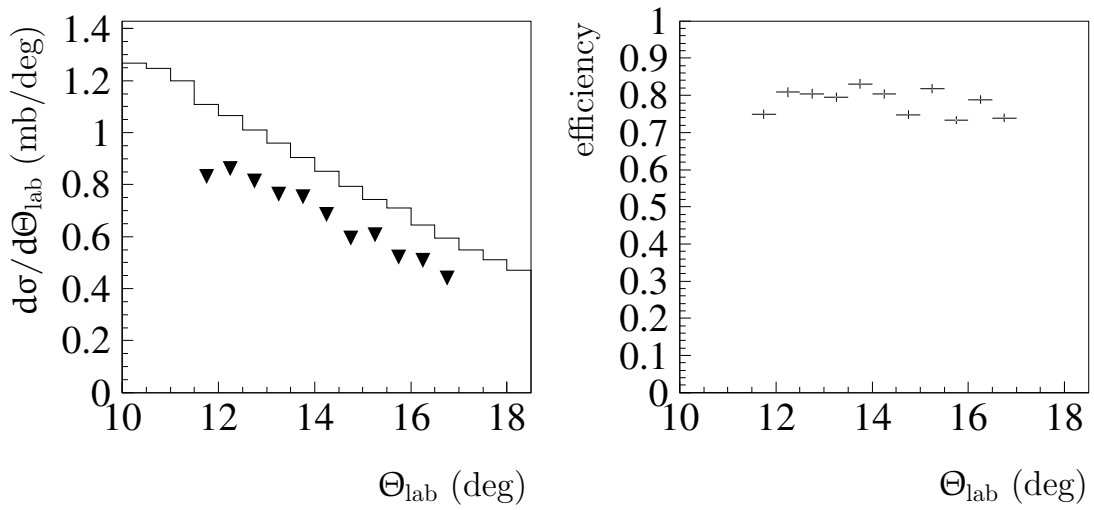

Figure 5.18: *Determining the overall efficiency distribution. On the left side, the GIN (histogram) and the Monte Carlo (triangles) angular distribution for* pp *elastic scattering (sample* ***PP1****, forward going proton) is plotted. The ratio GIN divided by Monte Carlo gives the efficiency distribution (right).*

- the geometrical acceptance,
- the detection efficiency,
- the reconstruction efficiency, and
- the trigger efficiency,

which have been introduced and discussed in the preceding sections. All of the above efficiency factors are included in the Monte Carlo analysis.

The efficiency correction function is obtained by first selecting Monte Carlo data with the same selection criteria used on the real data set to be corrected. The resulting angular distribution is divided by the initial one generated with GIN, resulting in the overall efficiency distribution $\epsilon(\Theta)$ that describes the simulated influence of the detection system on the input angular distribution (cf. Fig. 5.18).

For an evaluation of the remaining background in the final sample the calculation done in Sec. 5.1.2, "Physics Cuts", is not sufficient, since it cannot be used to extract a correction function for the angular distribution. Here, an assumption must be made about the background's constituency. Therefore, Monte Carlo simulations of the most prominent background reactions are carried out. These include the single and the double pion production in proton–proton reactions (cf. Table 5.13).

All background reactions are processed with the same reconstruction job as the Monte Carlo pp elastic scattering sample. Similar to the procedure visualized in

	σ (mb)	weight function in GIN (a.u.)
$pp \to d\pi^+$	0.4	$w = \frac{0.33 + 0.3 \cdot \cos^2(\Theta)}{(M_{N\pi^+} - M_\Delta)^2 + \Gamma_\Delta^2/4} \cdot \exp(-10 \cdot t)$
$pp \to pn\pi^+$	17.5	$w = \frac{0.278 + 0.41 \cdot \cos^2(\Theta)}{(M_{p\pi^0} - M_\Delta)^2 + \Gamma_\Delta^2/4} \cdot \exp(-10 \cdot t)$
$pp \to pp\pi^0$	4.5	$w = 0.27 + \cos^2(\Theta) - 0.6 \cdot \cos^4(\Theta)$
$pp \to pp\pi^0\pi^0$	0.24	$w = 1$ (phasespace)
$pp \to pp\pi^+\pi^-$	1.0	$w = 1$ (phasespace)
$pp \to pn\pi^+\pi^0$	1.0	$w = 1$ (phasespace)
$pp \to nn\pi^+\pi^+$	0.2	$w = 1$ (phasespace)
$pp \to pp$	22.0	SAID

Table 5.13: *Simulated reactions posing a background for the luminosity determination with cross sections from [S+82]. The* pp *elastic scattering is listed for comparison. The weights* w *are functions of the scattering angle* Θ *and the momentum transfer* t.

Fig. 5.9, the planarity cut is applied and the resulting opening angle distribution plotted. However, instead of using a polynomial it is fitted now with a histogram composed of the opening angle distributions of the individual background reactions, summed up by using the cross sections listed in Table 5.13 as relative weight. The total weight for each background reaction is the product of the cross section and the result of this background fit. Now, the inelastic angular distribution $u(\Theta)$ can be used to correct the experimental distribution $N(\Theta)$ (cf. Fig. 5.19).

Putting these corrections together, the "true" angular distribution $t_{pp}(\Theta)$ can be written as

$$t_{pp}(\Theta) = \frac{N_{pp}(\Theta) - u(\Theta)}{\epsilon(\Theta)}, \tag{5.24}$$

where

$N_{pp}(\Theta)$ is the uncorrected experimental angular distribution,
$u(\Theta)$ is the Monte Carlo background distribution, and
$\epsilon(\Theta)$ is the Monte Carlo efficiency distribution.

Using Eq. 5.24 in Eq. 5.23 one obtains

$$\sigma = 2\pi \int_{\Theta_{min}}^{\Theta_{max}} d\cos(\Theta) \frac{d\sigma_{pp}}{d\Omega_{lab}} = \frac{\sum_{\Theta_{min} \le \Theta_i \le \Theta_{max}} t_{pp}(\Theta_i)}{L}, \tag{5.25}$$

where

$L = \int \mathfrak{L} dt$ is the time integrated luminosity.

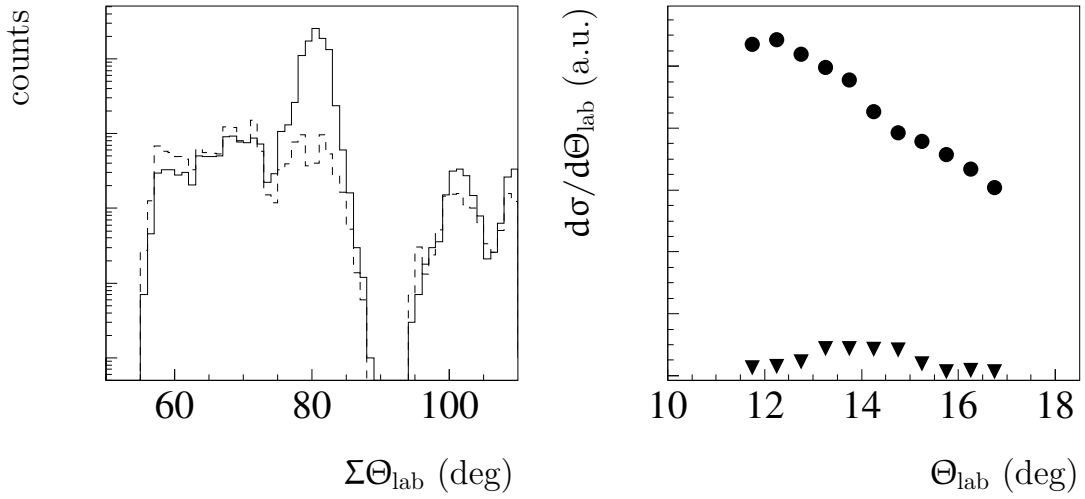

Figure 5.19: *Fitting the background contribution. The real data opening angle distribution (left, solid line) is fitted with background histogram containing simulated background reactions (dashed line) outside the kinematical correlation. With resulting weights, the angular distributions for real data and the simulated background can be plotted (right, circles and triangles, resp.)*

Though the integral luminosity L can be calculated easily with Eq. 5.25, more insight can be gained by comparing the expected and measured angular distributions:

$$2\pi \sin\Theta_i \Delta\Theta \frac{d\sigma_{pp}}{d\Omega_{lab}} = \Delta\Theta \frac{d\sigma_{pp}}{d\Theta_{lab}}(\Theta_i) = \frac{t_{pp}(\Theta_i)}{L}. \tag{5.26}$$

In this case, L is determined by fitting the left hand side with the right hand expression. This way, oddities in the measured distribution can be seen and the quality of the corrections applied judged.

In Fig. 5.20, the result for run 57 from the beam period in May, 2003, is shown. The triangles depict the efficiency corrected and background subtracted data points fitted to the GIN generated angular distribution. The data points reproduce the given distribution well within the shown statistical errors. The integral luminosity for this run is

$$L(55\text{ s} - 147\text{ s}) = (4.242 \pm 0.008(\text{stat}))\text{ nb}^{-1}. \tag{5.27}$$

5.3.3 Luminosity and Life Time

While the integral luminosity is the quantity needed for cross section calculations, it is generally not much good in judging the performance of this experiment. For that purpose, the luminosity is calculated by taking into account the elapsed life time.

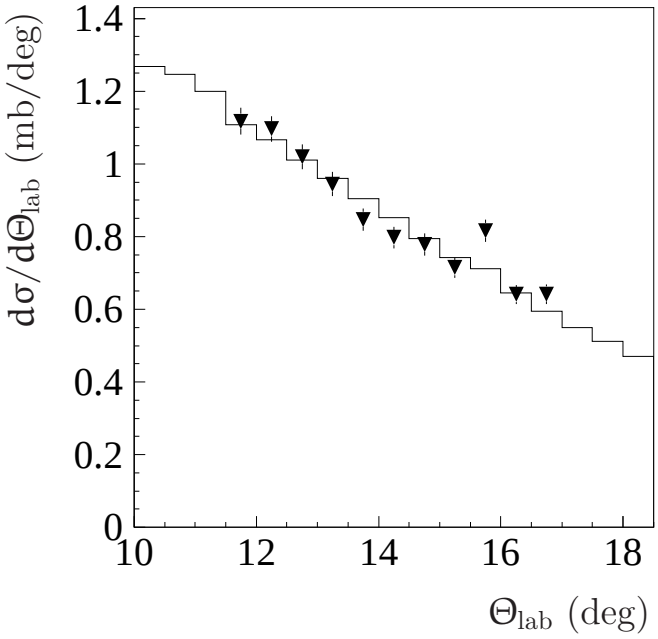

Figure 5.20: *The resulting experimental data angular distribution from May, 2003, run 57 (triangles) after subtracting the background, applying all efficiency corrections and fitting to the known angular distribution from SAID (solid line).*

The life time is calculated from the real time, which is the time elapsed in the laboratory, by taking into account two factors:

- The so–called duty factor f_{duty} of the accelerator. It is calculated as the ratio between the cycle time (typically 180 s), and the actual time interval, where the data acquisition can take place (usually the flat top, 55 s–147 s).
- The life time of the data acquisition system. It is calculated by comparing two scalers: One counts during the whole flat top, while the other is blocked, when the data acquisition system is busy with processing an event. The ratio f_{live} of the latter to the former gives the fraction where the data acquisition is alive.

There are two pairs of scalers available to determine the life time. One is based on a 100 kHz clock, the other on the unprescaled trigger signal CC1. Since the relation between the measured rate and the true rate is nonlinear, the clock based calculation will overestimate the lifetime the higher the initial luminosity is. Therefore, the CC1 based signal is used to evaluate f_{live}.

Using both the duty factor and the life time factor on the real time, one gets

$$\mathfrak{L} = \frac{L}{t_{life}}, \qquad t_{life} = t_{real} \cdot f_{duty} \cdot f_{live} \tag{5.28}$$

for the luminosity $\mathfrak{L}$ averaged over the whole run. The real time t_{real} is calculated by using the time tags at the beginning and the end of a run. Typically, a run taken under stable conditions is about 2 h long.

For the run shown above in Fig. 5.20, the elapsed real time adds up to 6240 s. With the duty factor of $f_{duty} = \frac{147\,s - 55\,s}{180\,s} = 51.1\%$ and an average life time of $f_{live} = 42.7\%$, the average luminosity from Eq. 5.27 is

$$\mathfrak{L} = (3.116 \pm 0.035(stat))\ 10^{30}\,cm^{-2}s^{-1}. \tag{5.29}$$

5.3.4 Systematic Errors

There are several sources for systematic errors in the luminosity calculation. Their magnitude is estimated by making reasonable assumptions on their variation and then processing the varied quantities through the whole luminosity determination.

The first and most important sources are the observables measured for the whole analysis: the *scattering and azimuthal angles* from both the Forward and the Central Detector. Using the granularity of both detector systems as an estimate for the angular resolution, the systematic errors can be deduced. For the Forward Detector, the errors in both the scattering and azimuthal angle amount to less than 0.5%. In the Central Detector, however, the errors are much larger. They reach 3% for the scattering angle, and 1.5% for the azimuth, which is not surprising minding the coarse granularity of the Electromagnetic Calorimeter.

Equally important is the error in the *background determination and subtraction*. There is an additional experimental knowledge on the background distribution from Fig. 5.9 and Table 5.8. Alternatively to the method used in this section, the background estimate of 7.3% from there is taken and the resulting integral luminosity is scaled by that value. This gives a luminosity that is 2.7% smaller than the one calculated above. To make a maximal error estimate, this value is treated as standard deviation, so that the systematic error of the background determination is $\sigma_{bkg} = 2.7\%$.

Since the sample used in this context uses both the Central and the Forward Detector, systematic errors can result from a relative *misalignment* of both detector arrays. To estimate this influence on the luminosity determination, the position of the Forward Detector was varied with respect to the origin along all three dimensions. If one assumes the Forward Detector to be misaligned less than 10 mm in all three dimensions, the combined error is less than 2%.

Another kind of systematic error arises from the uncertainity of the *vertex determination*. Using the result above (Sec. 5.2.3) and varying the vertex position within the errors given there, the influence on the luminosity calculation remains smaller than 1%.

Since the SAID database does not provide errors to the observables, the *normalization* error is estimated with the data set measured by the EDDA experiment [EDDA04a]. As above (Sec. 5.1.1), the data set for $T_{lab} = 1.328$ GeV is used. [EDDA04a] states two types of errors:

angles measured in the FD:	
polar $\sigma_{\Theta_{\mathrm{FD}}}$	$< 0.5\%$
azimuth $\sigma_{\Phi_{\mathrm{FD}}}$	$< 0.5\%$
angles measured in the CD:	
polar $\sigma_{\Theta_{\mathrm{CD}}}$	3.0%
azimuth $\sigma_{\Phi_{\mathrm{CD}}}$	1.5%
background subtraction σ_{bkg}	2.7%
detector misalignment σ_{alig}	$< 2.0\%$
vertex position σ_{vx}	$< 1.0\%$
normalization σ_{norm}	$< 0.1\%$
total	4.9%

Table 5.14: *Summary of systematic errors for the luminosity determination.*

- The total systematic and statistical error, which is a function of the scattering angle. For simplicity, the maximum observed error is taken for the whole distribution: $\sigma_{\mathrm{tot}} \approx 3.5\%$.
- The absolute and relative normalization error, which are given as 1.5% and 2.5% respectively: $\sigma_{\mathrm{n}} \approx 3.0\%$.

Varying the generated angular distribution by the quadratic sum of both errors above, it appears that the normalization error totally vanishes within the statistical error of the real distribution, giving $\sigma_{\mathrm{norm}} < 0.1\%$ for the normalization error.

All errors are summarized in Table 5.14. The total systematic error adds up to $\sigma_{\mathrm{tot}} = 4.9\%$.

5.3.5 Routine Application and Luminosity Monitoring

Extending the described method to other beam periods gives the opportunity to assess the evolution and performance of the CELSIUS/WASA experiment. Taking runs from December, 2002 till December, 2003, the resulting luminosities are listed in Table 5.15. A steady increase in the obtained luminosity can be seen that is due to improvements in the Pellet Target and the data acquisition system.

The method described here to calculate the luminosity is extensive, since it requires an exhaustive analysis. Though this cannot be avoided to get the stated accuracies, which are necessary for the cross section determination, it would be convenient to have the means to make a quick estimate of the present luminosity during the measurement by using a calibrated monitor.

One solution is to plot the average luminosity versus the rate of the C1 fastbus scaler, which counts the frequency of the unprescaled trigger C1 (cf. Table 5.6). This is done in Fig. 5.21. Apparently, the data points align along a straight line, except

for the data point from December, 2002. Leaving it out, a straight line is fitted to the remaining points, yielding a proportionality factor of about 55 kHz/10^{30}cm^{-2}s^{-1}. Since the fastbus scalers are available in the online monitoring system, this number can be used to estimate the luminosity with an accuracy of about 10%–15%.

Meanwhile, absolute luminosity numbers obtained through the method described in the preceding sections have been used to deduce absolute cross sections in different CELSIUS/WASA experiments (cf. [Jac04], [Koc04], and [P$^+$04]). Good agreement was found with literature values whereever available.

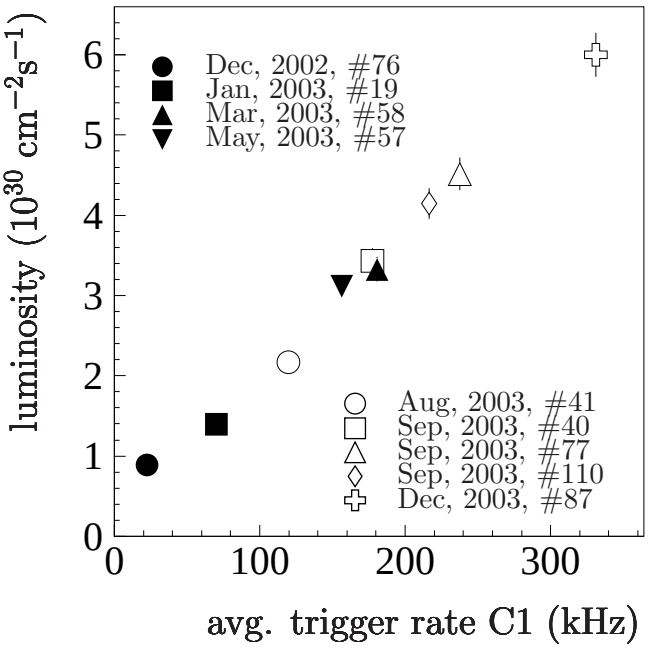

Figure 5.21: *The relation between the average luminosity and the scaler rate of trigger C1 for several beam periods. Obviously, the scaler rate is proportional to the luminosity and can therefore be used as luminosity monitor.*

beam period	run	avg. luminosity (10^{30} cm^{-2}s^{-1})
December, 2002	76	0.886 ± 0.025(stat)± 0.044(syst)
January, 2003	19	1.394 ± 0.009(stat)± 0.070(syst)
March, 2003	58	3.328 ± 0.024(stat)± 0.166(syst)
May, 2003	57	3.116 ± 0.035(stat)± 0.156(syst)
August, 2003	41	2.170 ± 0.014(stat)± 0.109(syst)
September, 2003	40	3.434 ± 0.027(stat)± 0.172(syst)
September, 2003	77	4.517 ± 0.040(stat)± 0.226(syst)
September, 2003	110	4.148 ± 0.041(stat)± 0.207(syst)
December, 2003	87	5.999 ± 0.047(stat)± 0.300(syst)

Table 5.15: *Average luminosities of selected runs from different periods.*

Chapter 6

Summary and Outlook

Two distinct analyses of data taken with the unique WASA detector at the CELSIUS hadron synchrotron have been presented in this work.

The first one has discussed data taken during the November, 2001 beam period, where a deuteron beam of $T_d = 560$ MeV impinged on hydrogen pellets. Differential distributions for the reactions $dp \to dp\pi^0$ and $dp \to dp\gamma$ have been extracted and compared to the predictions of the Spectator Model ([MN93]).

Qualitatively, the previous results from [Gre99] have been confirmed with the WASA setup's larger accepted phase space and increased sensitivity for the phenomenological models used in the analysis. The Spectator Model alone fails to describe the experimental distributions. Coherent mechanisms have to be added to the model which has been done in a similar fashion as in the previous work.

Quantitatively, the Spectator Model contribution amounted to 64% (59% in [G+00]) for the pion production reaction and 66% (65% in [G+02]) for the bremsstrahlung process. Within the statistical accuracy, both results here are in well agreement with the previous ones. The luminosity has been determined through the pion production process, yielding $1.26 \pm 0.31 \cdot 10^{30}$ cm^{-2}s^{-1} (12.81 ± 3.15 nb^{-1}) for the luminosity (integral luminosity). Using this result and the percentage of the Spectator Model, the quasifree cross section $\sigma_{\mathrm{tot},dp\to d\gamma p_s}$ for the bremsstrahlung process has been determined as 10.3 ± 4.9 μb, being in agreement with the previous result of 17.9 ± 5.5 μb.

However, the outcome of the experiment ranged below the expectations. Although both the acceptance and the luminosity were higher than in the previous experiment, smaller statistics were collected for both reactions in almost twice the time (cf. Table 6.1).

It seems that the extended capabilities of the detection system, i.e. almost full angular coverage and the Pellet Target system, were outweighted by the experimental difficulties originating from the beam target interaction. The heating of the deuteron beam in the pellet target caused a large beam spread, resulting in a low beam life time and high background conditions. The former let to a significantly lower duty factor of the accelerator (28% vs. 79% in the previous experiment), the latter, in combination with triggers with a low selectivity, forced high prescaling

	[Gre99]	WASA
total time (s)	59400	95520
main trigger prescaling factor	8	80
duty factor (%)	79	28
life time fraction (%)	45	38
integral luminosity (nb^{-1})	17.2	12.81
$dp \to dp\pi^0$ "MM"	12480	4072
$dp \to dp\gamma$	590	360

Table 6.1: *Comparison of experimental parameters in the present work and the previous experiment [Gre99].*

factors on the physics triggers, eating away the gain in detector acceptance and luminosity. Improvements can be expected from the production of pellets with smaller diameters and from a more advanced data acquisition system with more selective triggers and a faster readout; good progress has been made recently in both fields.

Furthermore, no attempt to investigate the systematic errors has been done. Due to the missing MDC at that time, the best known reaction at the given projectile energy, the elastic deuteron–proton scattering, could not be investigated.

To gain a deeper insight into the WASA detection system, the analysis of several beam periods between December, 2002 and December, 2003, has been carried out. To overcome the experimental difficulties involved by a low energy deuteron beam impinging on the Pellet Target, data taken with a high energy proton beam of $T_p = 1.36$ GeV have been chosen for this investigation. The analysis is detailed for a data sample from May, 2003.

First, both the generation of simulated and the selection of experimental elastic proton–proton events has been discussed in great detail. The gained samples are used to check for detector inaccuracies and inefficiencies. Then the vertex position is calculated, showing a small shift of the vertex which is not in agreement with the nominal vertex position within the given errors:

$$\text{runs 27–37:} \quad (x_v, y_v, z_v) = (-2.3 \pm 1.3, -1.6 \pm 1.2, -2.0 \pm 1.2) \text{ mm}$$
$$\text{runs 38–52:} \quad (x_v, y_v, z_v) = (-2.2 \pm 1.3, -1.3 \pm 1.2, -1.6 \pm 1.2) \text{ mm}$$

Using these results, angular distributions from simulated and experimental data are extracted. The correction function for the overall efficiency is calculated as well as the background contribution to the experimental data distribution, obtained by producing inelastic Monte Carlo data sets. With reference to the well–known differential cross section, both the luminosity and the integral luminosity are calculated. It shows that the luminosity steadily increased in the investigated time period, reaching $6 \cdot 10^{30}$ $cm^{-2}s^{-1}$ in December, 2003, which is almost a factor of seven higher than in December, 2002. Several sources for systematic errors have

been investigated, showing an overall systematic error of less than 5%.

Outlook

As has already been mentioned in Chap. 2, the basic research program at the CELSIUS storage ring will end in the fall of 2005. While the TSL will move its main applied research focus towards proton therapy, the WASA detector is proposed to be moved to another hadron synchrotron, the COSY in Jülich, Germany. The COSY storage ring is newer and larger than the CELSIUS ring, it offers proton and deuteron beams of higher intensity and reaches energies of up to $T_p = 2.5$ GeV for protons. In addition, COSY delivers also spin polarized beams.

The physics goals of "WASA at COSY" take up the decay physics program of CELSIUS/WASA, searching for not–so–rare and rare decays of the η meson. Due to the increase in beam energy, also the η' meson can be produced. The decays of both mesons provide a platform where symmetries and symmetry breaking patterns in hadronic systems can be investigated. Concerning the production physics, "WASA at COSY" will be able to investigate exotic hadron resonances like the Pentaquark.

The present status of the "WASA at COSY" experiment is as follows:

- A detailed proposal ([COSY04]) has been prepared and submitted to the COSY Program Advisory Commitee (PAC).
- The PAC responded in its 29th session in November, 2004, endorsing the "WASA at COSY" project.
- Preliminary time schedules plan to dismantle the whole experimental setup in late summer 2005. Preparations for the installation of WASA in the COSY ring are underway. The installation itself could begin already at the end of 2005.

Appendix A

Acronyms

ADC	**A**nalog–To–**D**igital **C**onverter
C	**C**harge conjugation
CD	**C**entral **D**etector
CDN	**n**eutral particle **C**entral **D**etector track
CELSIUS	**C**ooling with **El**ectrons and **S**toring of **I**ons from **U**ppsala **S**ynchrocyclotron
DAQ	**D**ata **A**cquisition **S**ystem
CERN	**C**onseil **E**uropéen pour la **R**echerche **N**ucléaire
COSY	**Co**oler **Sy**nchrotron
CP	**C**harge conjugation and **P**arity
CPT	**C**harge conjugation, **P**arity, and **T**ime reversal
EDDA	**E**xcitation function **D**ata acquisition **D**esigned for the **A**nalysis of phase shifts
FD	**F**orward **D**etector
FDC	**c**harged particle **F**orward **D**etector track
FHD	**F**orward **Hod**oscope
FJH	**F**orward **J**ülich **H**odoscope
FPC	**F**orward **P**roportional **C**hambers
FRA	**F**orward **R**ange **A**bsorber
FRH	**F**orward **R**ange **H**odoscope
FRI	**F**orward **R**ange **I**nterleaving **H**odoscope
FSI	**F**inal **S**tate **I**nteraction
FTH	**F**orward **T**rigger **H**odoscope
FVH	**F**orward **V**eto **H**odoscope
FWC	**F**orward **W**indow **C**ounters
FWHM	**F**ull **W**idth at **H**alf **M**aximum
IUCF	**I**ndiana **U**niversity **C**ooler **F**acility
MM	**M**issing **M**ass
MDC	**M**ini **D**rift **C**hamber
ph.sp	**ph**ase **sp**ace
P	**P**arity

PM	**p**hoto**m**ultiplier
PMT	**p**hoto**m**ultiplier **t**ube
PROMICE	**PRO**duction of **M**esons **I**n **CE**lsius
PSB	**P**lastic **S**cintillator Barrel, **b**ackward part
PSC	**P**lastic **S**cintillator Barrel, **c**entral part
PSF	**P**lastic **S**cintillator Barrel, **f**orward part
QCD	**Q**uantum **C**hromo **D**ynamics
QDC	charge (**Q**) sensitive Analog–To–**D**igital **C**onverter
SAID	**S**cattering **A**nalysis **I**nteractive **D**ial–In
SM	**S**pectator **M**odel
SCS	**S**uper**c**onducting **S**olenoid
SEB	**S**cintillating **E**lectromagnetic Calorimeter, **b**ackward part
SEC	**S**cintillating **E**lectromagnetic Calorimeter, **c**entral part
SEF	**S**cintillating **E**lectromagnetic Calorimeter, **f**orward part
TDC	**T**ime–to–**D**igital **C**onverter
TSL	**T**he **S**vedberg **L**aboratory
WASA	**W**ide **A**ngle **S**hower **A**pparatus

Appendix B

Beam and Target Diagnostics — Supplements

B.1 Definitions of Cuts Applied on Elastic pp Scattering

Time cuts (P4TM)	none
Selection cuts (SLxx)	all off
Thresholds (P4PE)	Version "P4PES" (Status without thresholds), A540
Track selection	1 charged track in FD (hits in FWC, FPC, FHD3, FRH1–4) with $11.5^\circ \leq \Theta_{1,\mathrm{lab}} \leq 17^\circ$ 1 charged track in central CD (PSC and SEC required)
Opening angle	$\lvert\Theta_{1,\mathrm{lab}} + \Theta_{2,\mathrm{lab}} - 82.5^\circ\rvert \leq 7.5^\circ$
Planarity	$\lvert\lvert\Delta\Phi\rvert - 180^\circ\rvert \leq 3 \cdot \sigma_{\Delta\Phi}, \quad \sigma_{\Delta\Phi} = 2.5^\circ$

Table B.1: *Cuts and selection rules for elastic sample **PP1**, Monte Carlo data.*

Time cuts (P4TM)	none
Selection cuts (SLxx)	all off
Thresholds (P4PE)	Version "P4PES" (Status without thresholds), A540
Track selection	1 charged track in forward CD (PSF and SEF required) with $20^\circ \leq \Theta_{1,\mathrm{lab}} \leq 36^\circ$ 1 charged track in central CD (PSC and SEC required)
Opening angle	$\lvert\Theta_{1,\mathrm{lab}} + \Theta_{2,\mathrm{lab}} - 75^\circ\rvert \leq 7.5^\circ$
Planarity	$\lvert\lvert\Delta\Phi\rvert - 180^\circ\rvert \leq 3 \cdot \sigma_{\Delta\Phi}, \quad \sigma_{\Delta\Phi} = 4.0^\circ$

Table B.2: *Cuts and selection rules for elastic sample **PP2**, Monte Carlo data.*

Time cuts (P4TM)	none
Selection cuts (SLxx)	all off
Thresholds (P4PE)	Version "P4PES" (Status without thresholds), A540
Track selection	1 charged track in FD (hits in FWC, FPC, FHD3, FRH1–4) with $6.5^\circ \leq \Theta_{1,\mathrm{lab}} \leq 17^\circ$ 1 charged track in CD (MDC required)
Opening angle	$\lvert\Theta_{1,\mathrm{lab}} + \Theta_{2,\mathrm{lab}} - 82.5^\circ\rvert \leq 7.5^\circ$
Planarity	$\lvert\lvert\Delta\Phi\rvert - 180^\circ\rvert \leq 3 \cdot \sigma_{\Delta\Phi}, \quad \sigma_{\Delta\Phi} = 1.0^\circ$

Table B.3: *Cuts and selection rules for elastic sample **PP4**, Monte Carlo data.*

Period / Runs	5401xx / 27-37,38-52
Trigger	D1 (1 FRH1 $\wedge$ 1 PSC)
Time cuts (P4TM)	(1900-2000/1950-2050) on FD/PS scintillators (0-200,150-350) on FPC (1850-2150) on SE, (1980-2150/2225/2300) on MDC
Selection cuts (SLxx)	all off
Thresholds (P4PE)	Version "P4PES" (Status without thresholds), A540
Track selection	1 charged track in FD (hits in FWC, FPC, FHD3, FRH1–4) with $11.5^\circ \leq \Theta_{1,\mathrm{lab}} \leq 17^\circ$ 1 charged track in central CD (PSC and SEC required)
Opening angle	$\lvert\Theta_{1,\mathrm{lab}} + \Theta_{2,\mathrm{lab}} - 82.5^\circ\rvert \leq 10^\circ$
Planarity	$\lvert\lvert\Delta\Phi\rvert - 180^\circ\rvert \leq 3 \cdot \sigma_{\Delta\Phi}, \quad \sigma_{\Delta\Phi} = 3.1^\circ$

Table B.4: *Cuts and selection rules for elastic sample **PP1**, experimental data from May, 2003.*

Period / Runs	5401xx / 27-37,38-52
Trigger	DC1 (1 PSF $\wedge$ 1 PSC)
Time cuts (P4TM)	(1950-2050) on PS, (1850-2150) on SE (1980-2150/2225/2300) on MDC
Selection cuts (SLxx)	all off
Thresholds (P4PE)	Version "P4PES" (Status without thresholds), A540
Track selection	1 charged track in forward CD (PSF and SEF required) with $20^\circ \leq \Theta_{1,\mathrm{lab}} \leq 36^\circ$ 1 charged track in central CD (PSC and SEC required)
Opening angle	$\lvert\Theta_{1,\mathrm{lab}} + \Theta_{2,\mathrm{lab}} - 75^\circ\rvert \leq 10^\circ$
Planarity	$\lvert\lvert\Delta\Phi\rvert - 180^\circ\rvert \leq 3 \cdot \sigma_{\Delta\Phi}, \quad \sigma_{\Delta\Phi} = 6.0^\circ$

Table B.5: *Cuts and selection rules for elastic sample **PP2**, experimental data from May, 2003.*

Period / Runs	5401xx / 27-37,38-52
Trigger	D1 (1 FRH1 $\wedge$ 1 PSC)
Time cuts (P4TM)	(1950-2050/1900-2100) on FD/PS scintillators (0-200,150-350) on FPC (1850-2150) on SE, (1980-2150/2225/2300) on MDC
Selection cuts (SLxx)	all off
Thresholds (P4PE)	Version "P4PES" (Status without thresholds), A540
Track selection	1 charged track in FD (hits in FWC, FPC, FHD3, FRH1–4) with $6.5^\circ \leq \Theta_{1,\mathrm{lab}} \leq 17^\circ$ 1 charged track in CD (MDC required)
Opening angle	$\lvert\Theta_{1,\mathrm{lab}} + \Theta_{2,\mathrm{lab}} - 82.5^\circ\rvert \leq 10^\circ$
Planarity	$\lvert\lvert\Delta\Phi\rvert - 180^\circ\rvert \leq 3 \cdot \sigma_{\Delta\Phi}, \quad \sigma_{\Delta\Phi} = 3.1^\circ$

Table B.6: *Cuts and selection rules for elastic sample **PP4**, experimental data from May, 2003.*

B.2 Monte Carlo and Experimental d–distributions

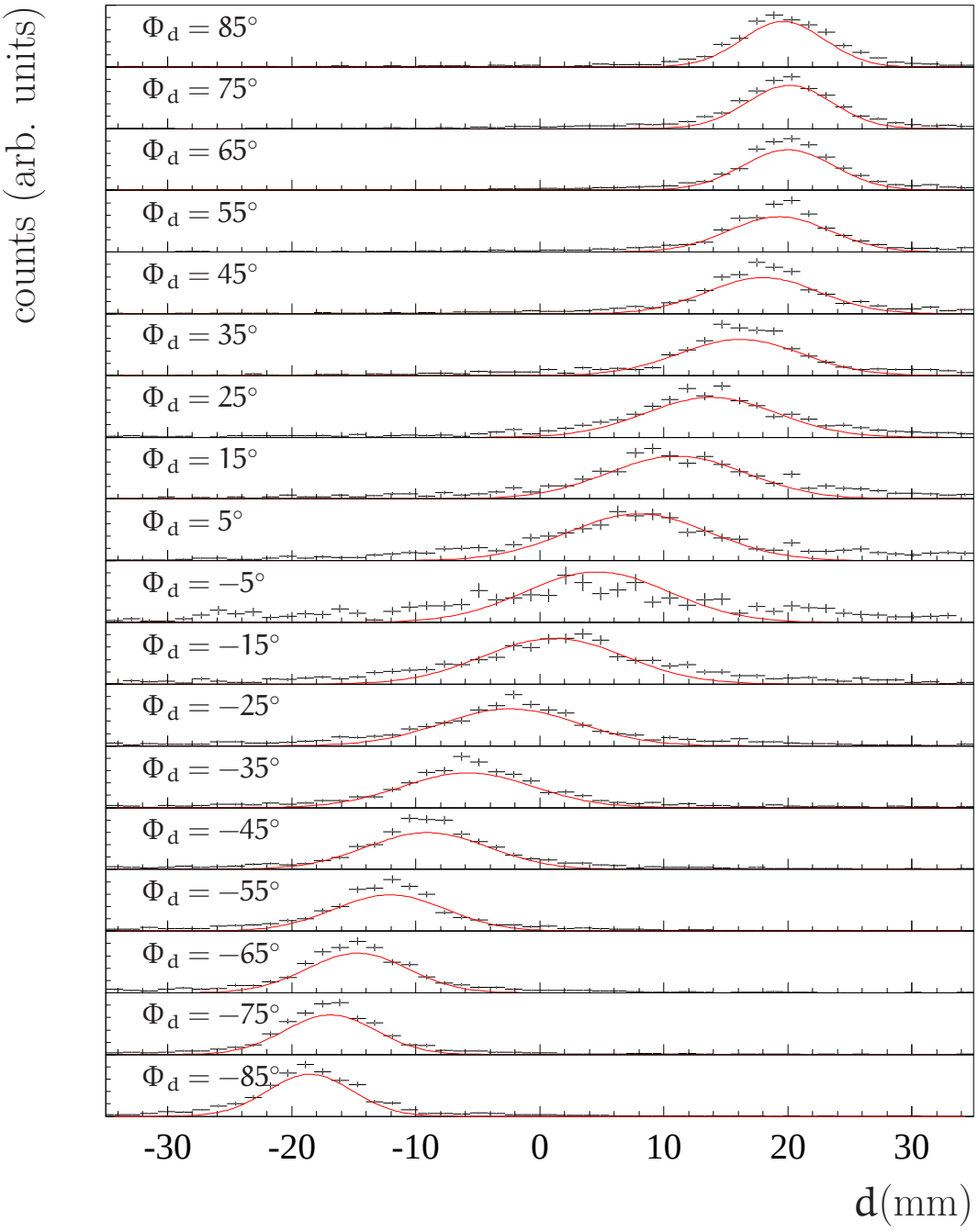

Figure B.1: *Simulated* d*–distributions for a displaced vertex position at* $(0, -20\,\mathrm{mm}, 0)$*. The fitted Gaussian is superimposed.*

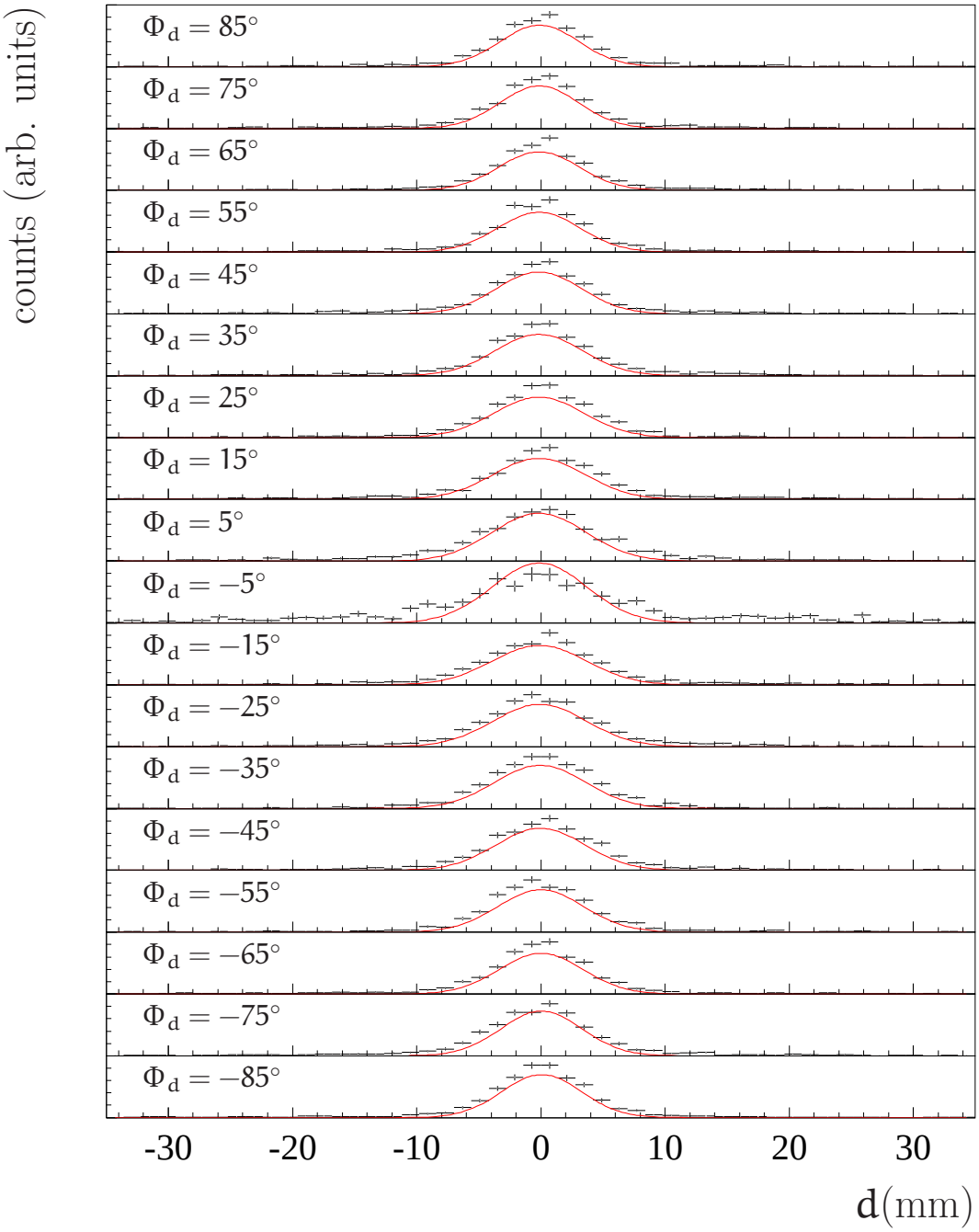

Figure B.2: *Simulated* d*–distributions for a vertex at the origin* $(0, 0, 0)$*. The fitted Gaussian is superimposed.*

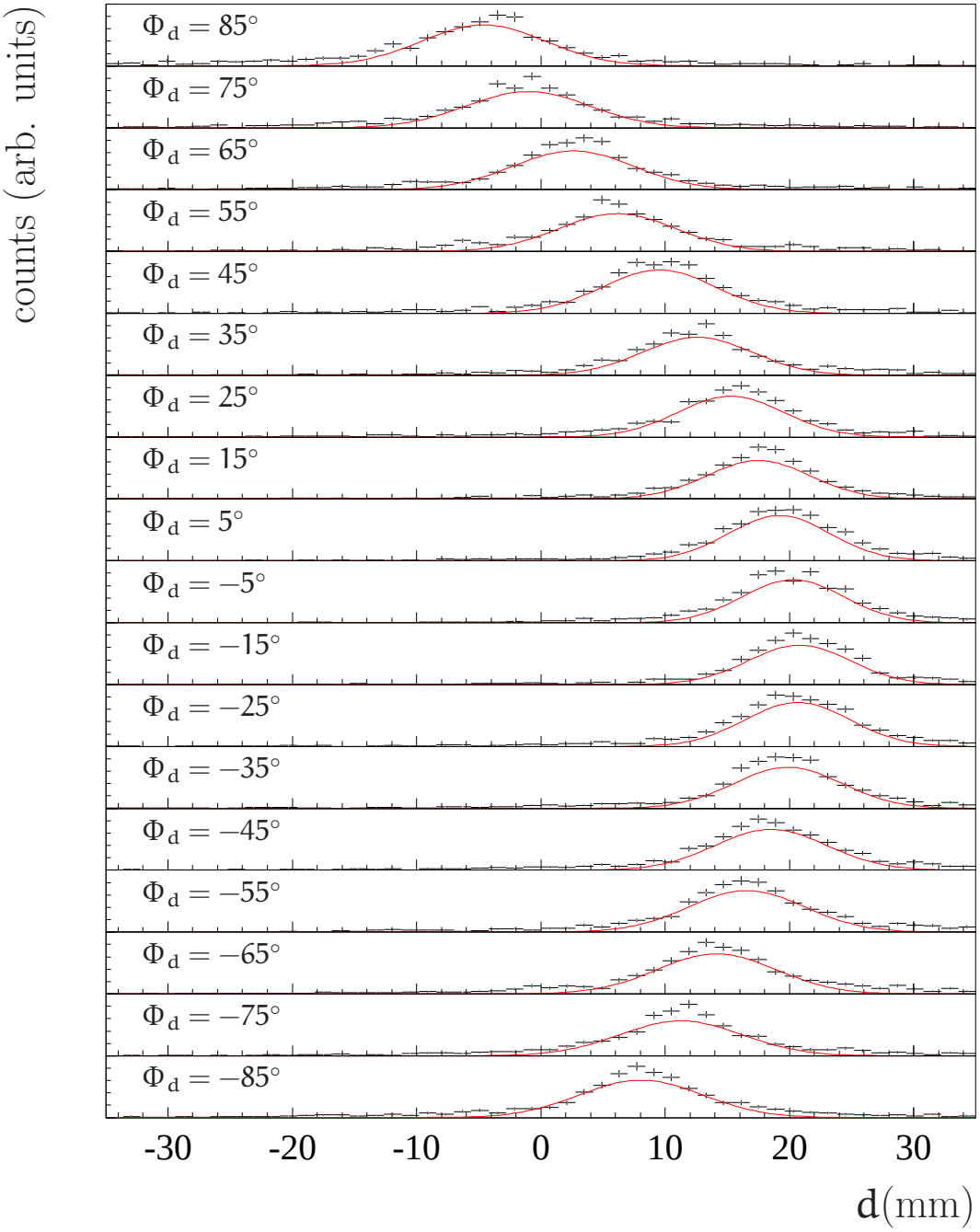

Figure B.3: *Simulated* d*–distributions for a displaced vertex position at* $(20\,\mathrm{mm}, 0, 0)$*. The fitted Gaussian is superimposed.*

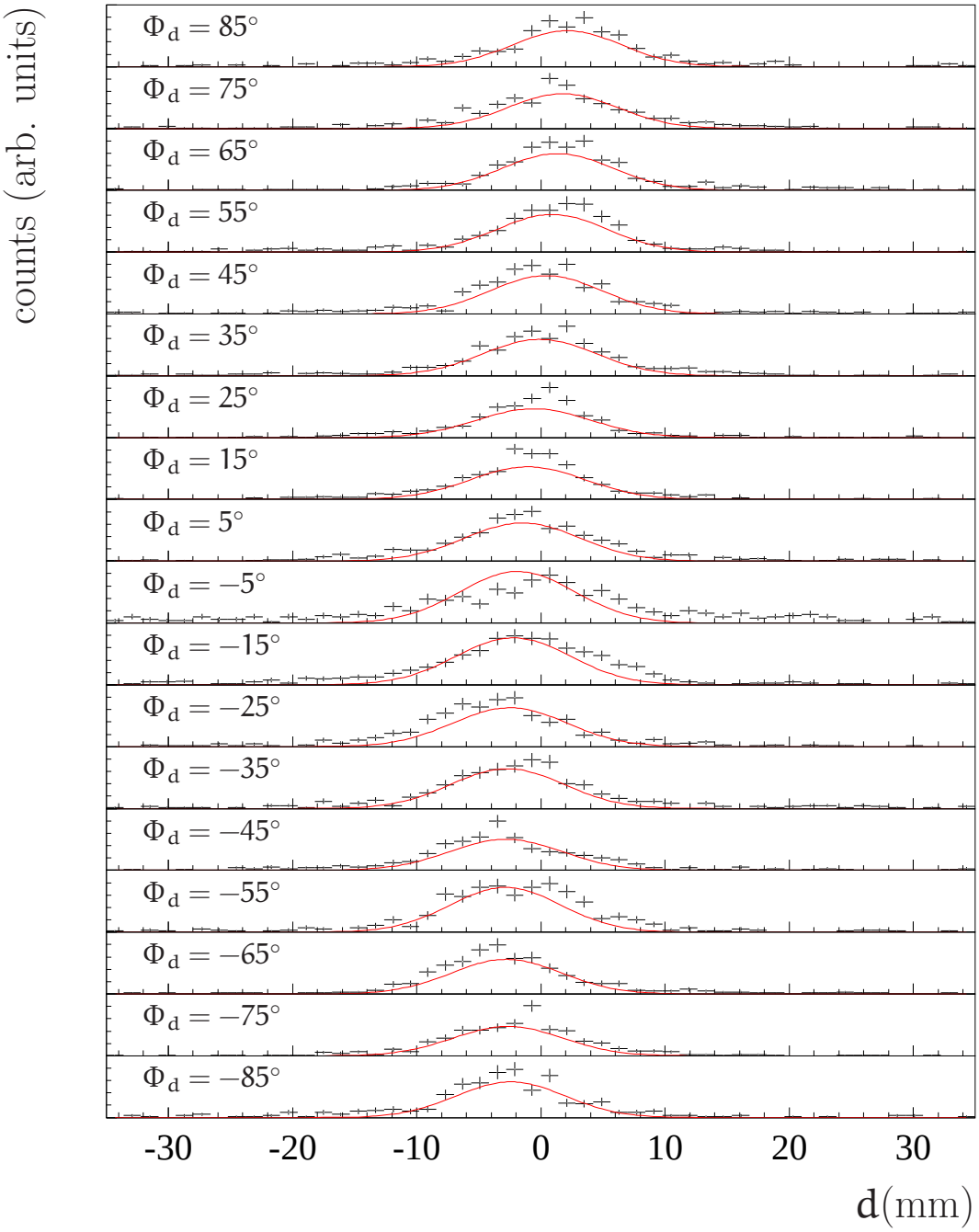

Figure B.4: *Experimental* d*–distributions for Runs 27-37 from the May 2003 beam period. The fitted Gaussian is superimposed.*

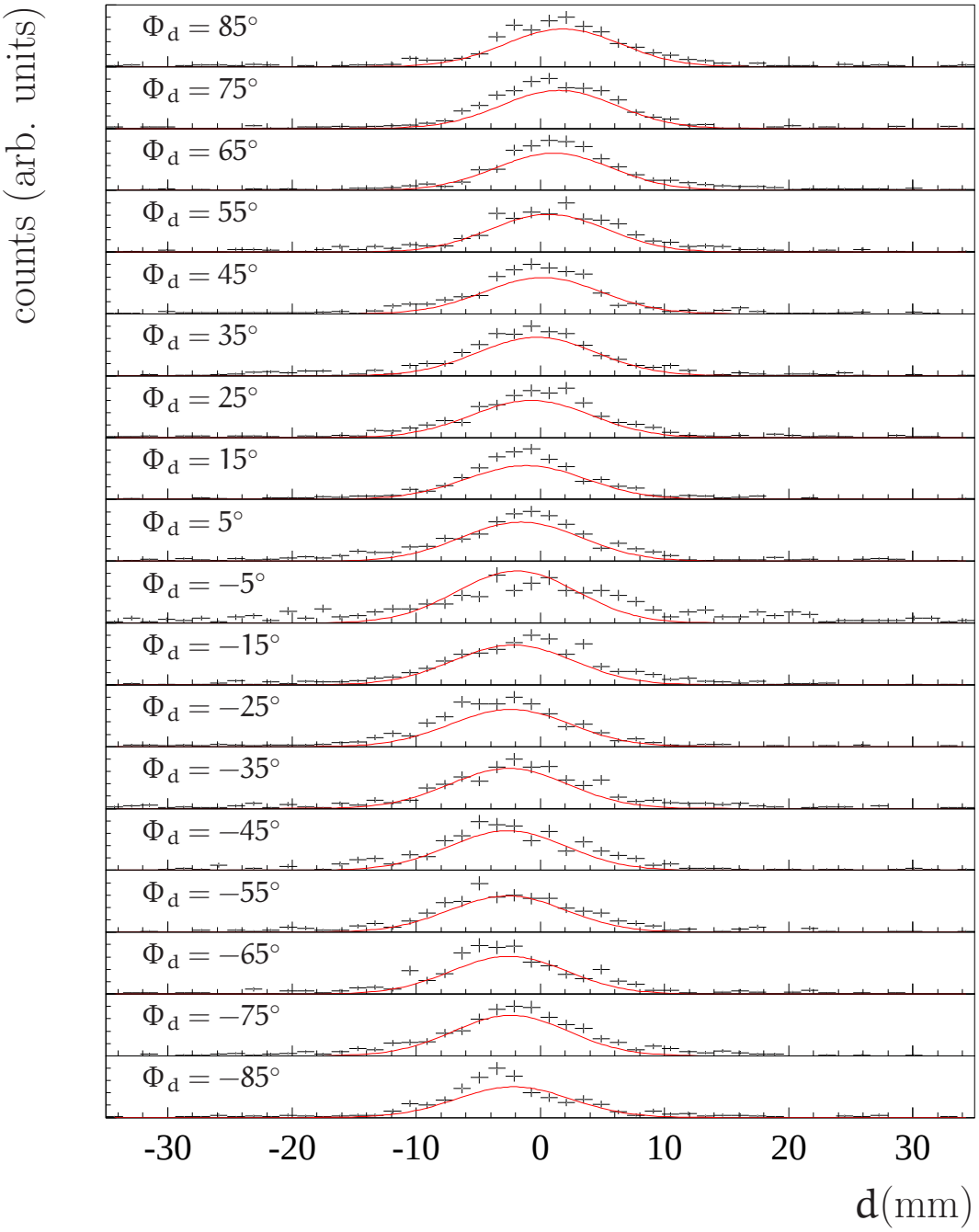

Figure B.5: *Experimental* d*–distributions for Runs 38-52 from the May 2003 beam period. The fitted Gaussian is superimposed.*

B.3 Monte Carlo and Experimental Θ_2'–distributions

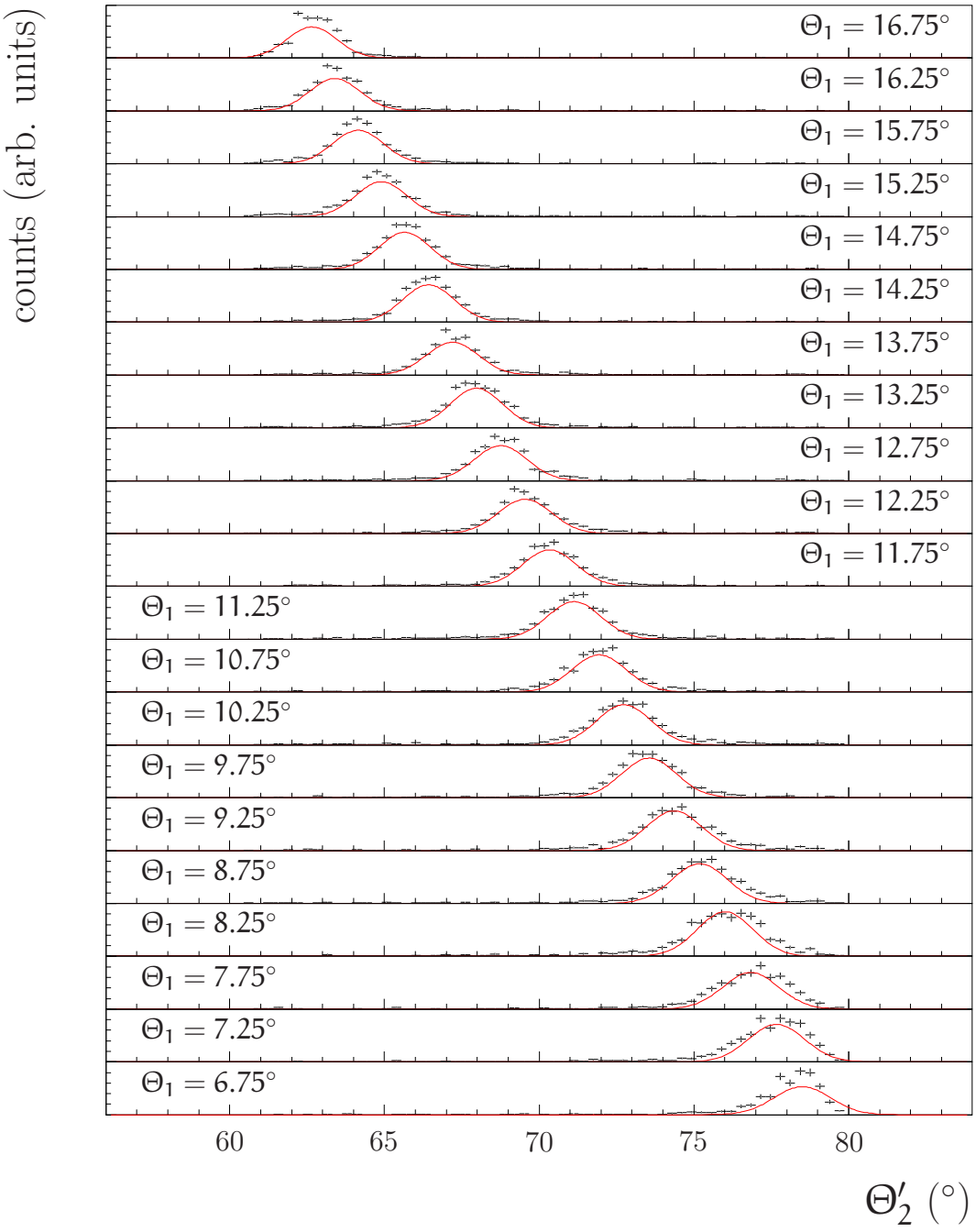

Figure B.6: *Simulated Θ_2'–distributions for the unshifted sample. The fitted Gaussian is superimposed.*

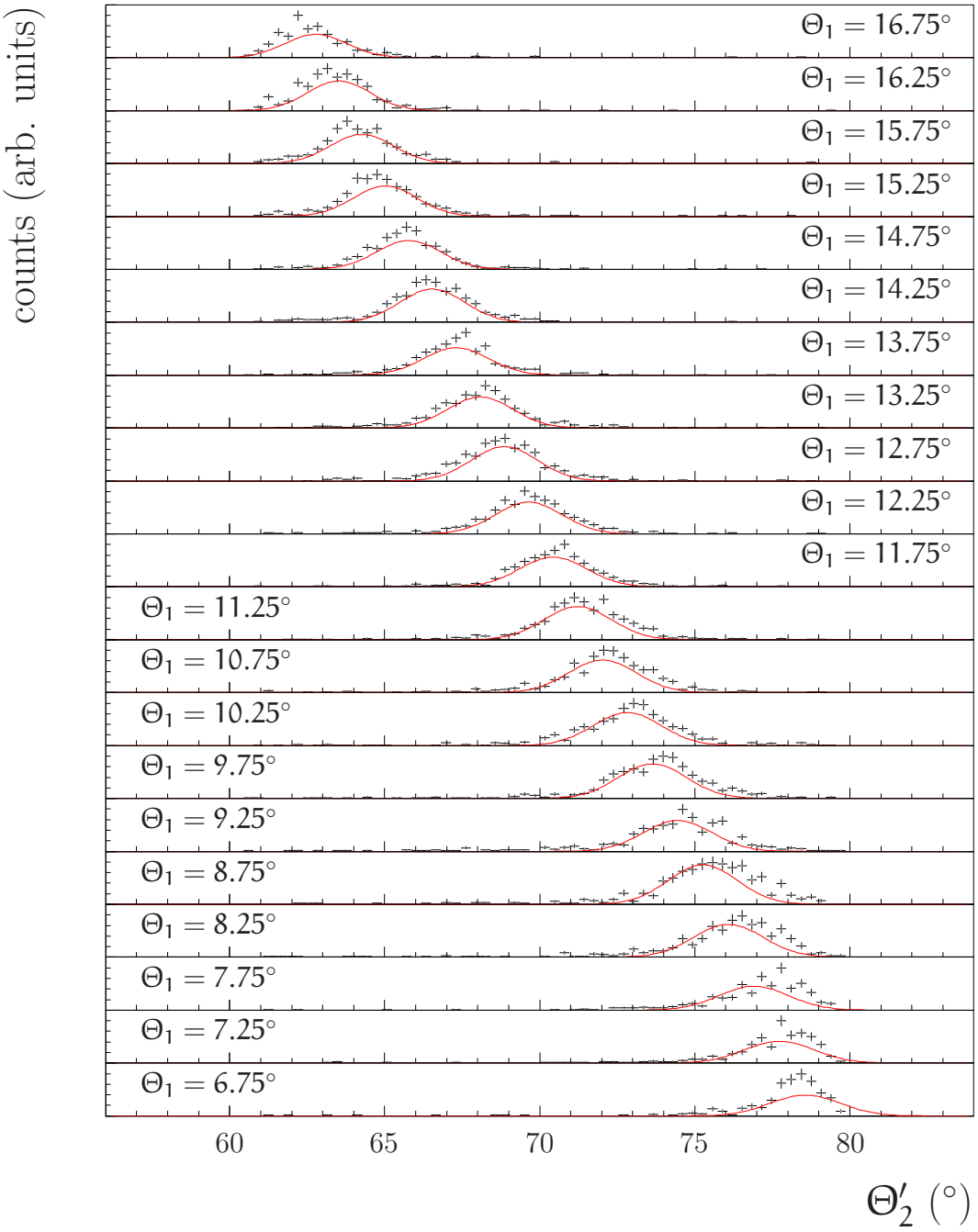

Figure B.7: *Experimental Θ'_2–distributions for Runs 27-37 from the May 2003 beam period. The fitted Gaussian is superimposed.*

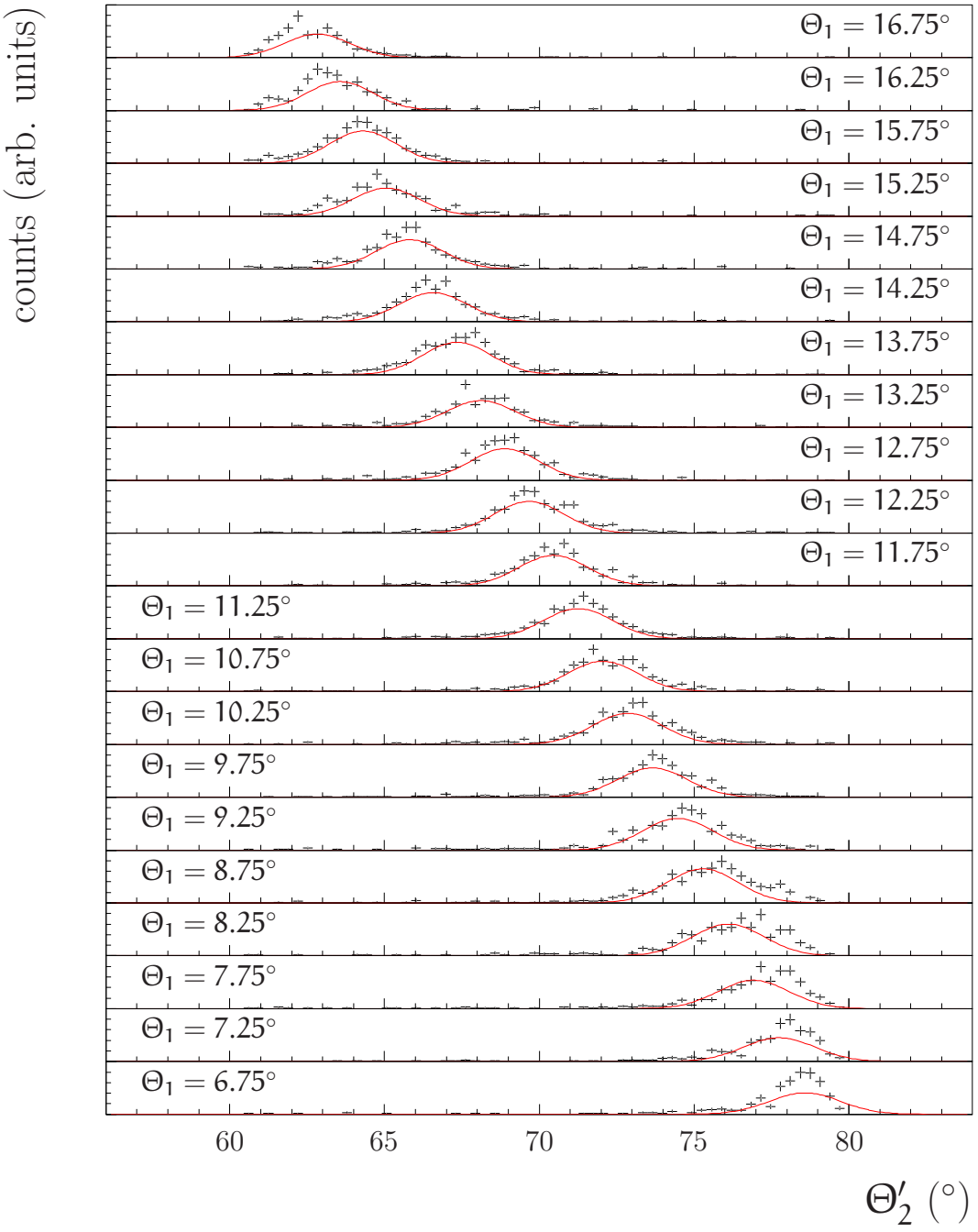

Figure B.8: *Experimental Θ'_2–distributions for Runs 38-52 from the May 2003 beam period. The fitted Gaussian is superimposed.*

B.4 Monte Carlo γ^2_{cm}–distributions

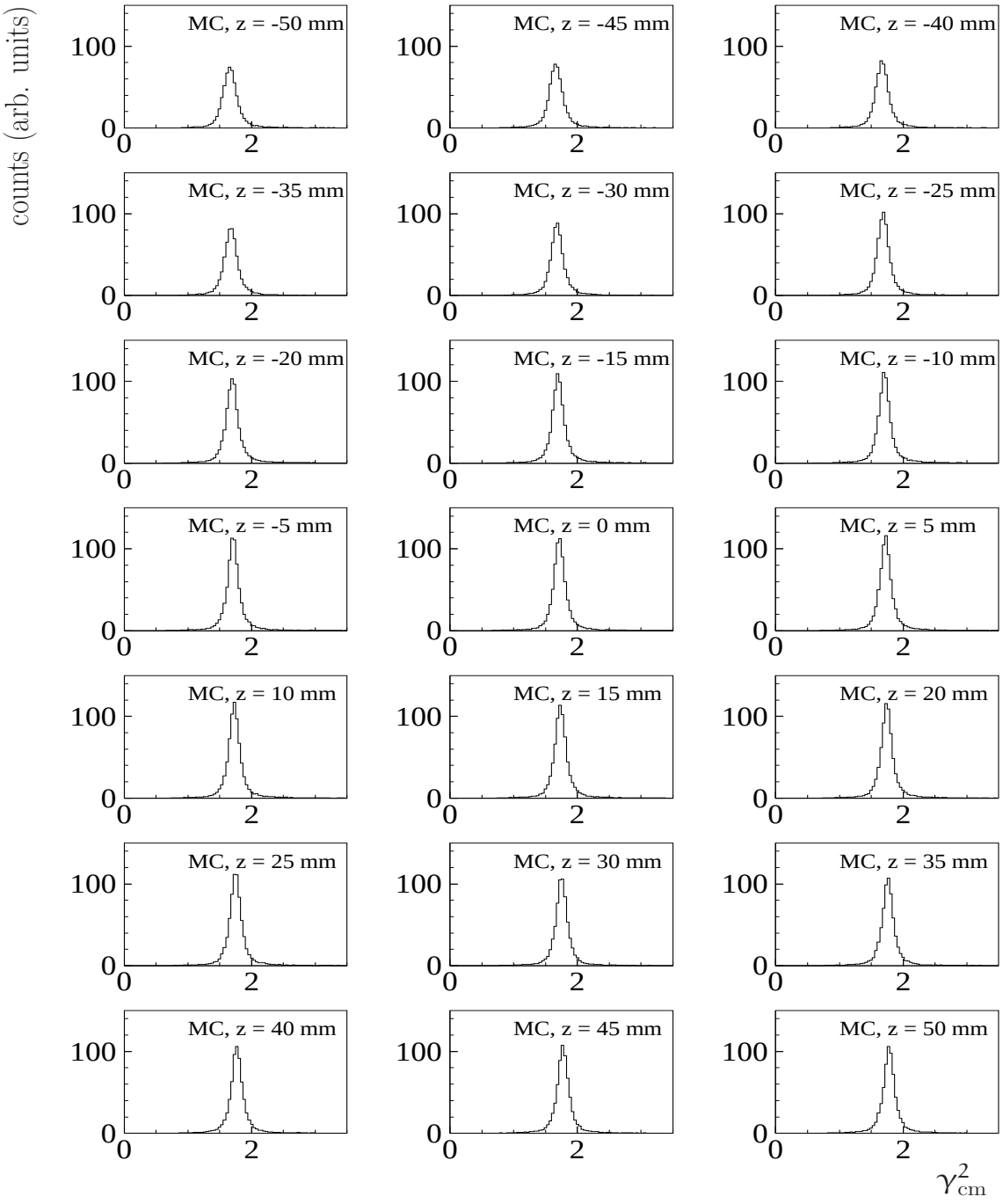

Figure B.9: *Distributions of γ^2_{cm} for sample **PP4**, simulated at different z positions.*

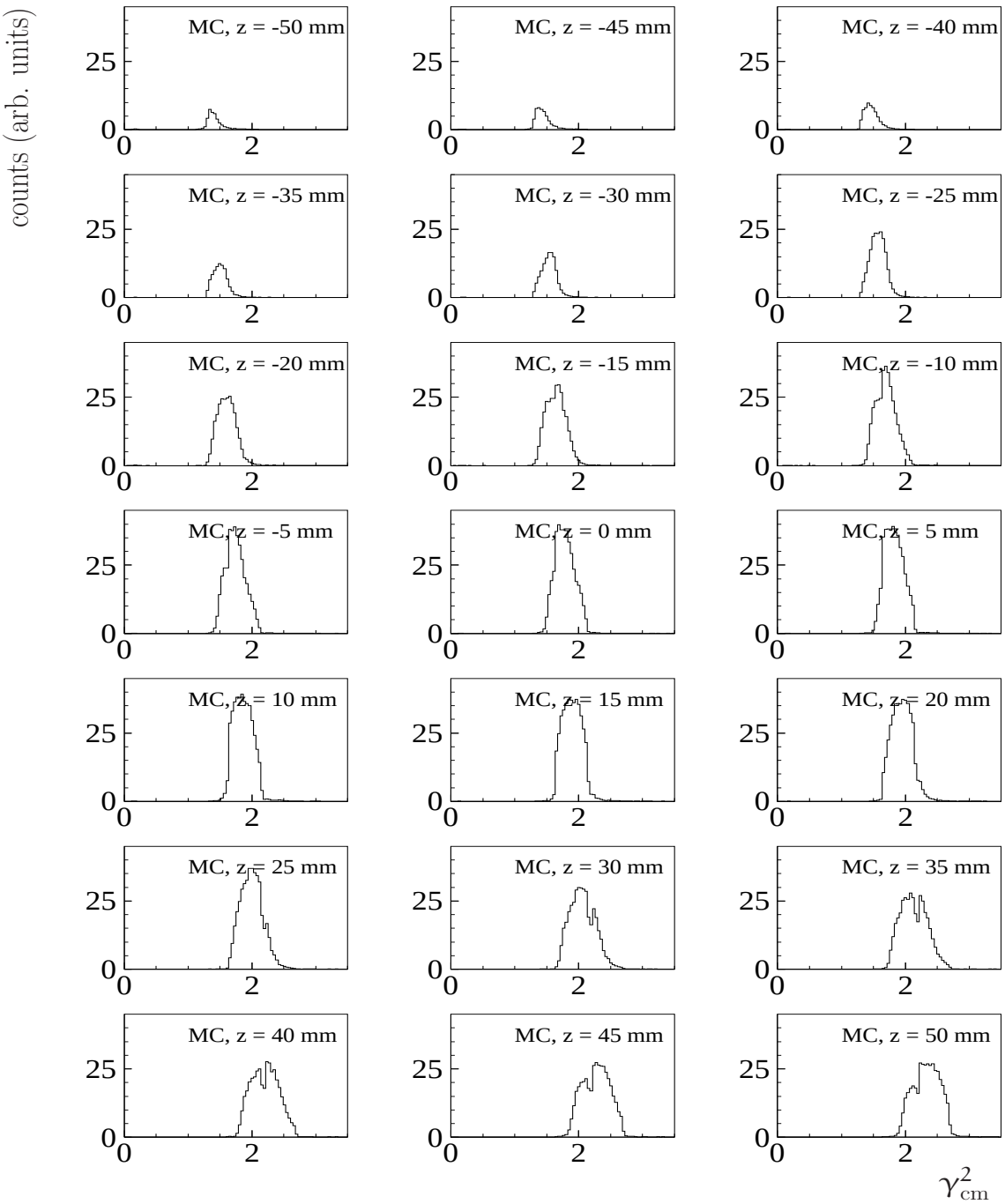

Figure B.10: *Distributions of γ^2_{cm} for sample **PP1**, simulated at different z positions.*

B.5 Relation between (x_v, y_v) and (d, Φ_d)

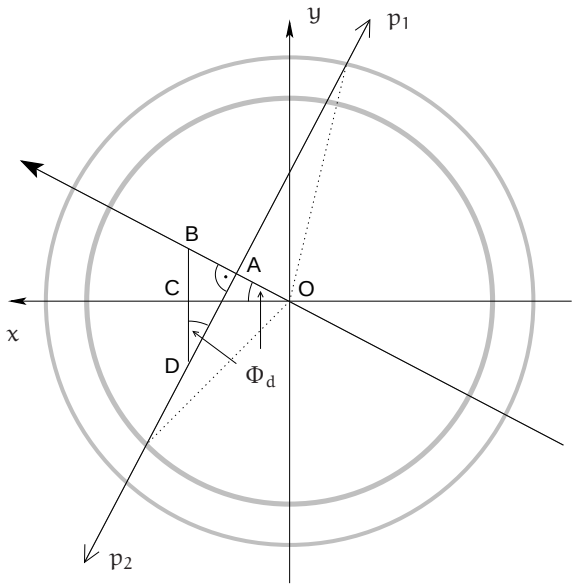

Figure B.11: *Schematical view of the geometry.*

To calculate $d = |AO|$ (see fig.B.11) in terms of x_v and y_v, an additional line $|BC|$ is introduced. Then the angle $\angle(BDA)$ equals Φ_d and with $D = (x_v, y_v)$ one can write the following equations:

$$d = |BO| - |BA|,$$

$$\text{with} \qquad |BO| = \frac{|CO|}{\cos\Phi_d}, \qquad |BA| = (|BC| + |CD|) \cdot \sin\Phi_d,$$

$$|CO| = x_v, \qquad |BC| = x_v \cdot \tan\Phi_d, \qquad |CD| = -y_v.$$

Putting it all together one gets:

$$\begin{aligned} d &= \frac{x_v}{\cos\Phi_d} - (x_v \cdot \tan\Phi_d - y_v) \cdot \sin\Phi_d \\ &= \frac{x_v}{\cos\Phi_d} - \frac{x_v \cdot \sin^2\Phi_d}{\cos\Phi_d} + y_v \cdot \sin\Phi_d \\ &= \frac{x_v(1 - \sin^2\Phi_d)}{\cos\Phi_d} + y_v \cdot \sin\Phi_d \end{aligned}$$

resulting in

$$d = x_v \cos\Phi_d + y_v \sin\Phi_d.$$

B.6 Resolution with and without MDC Information

Since the MDC reconstruction package takes a lot of computing time, the analysis in Sec. 5.2.1 is done without the usage of any MDC information. One can expect a significantly worse resolution for the vertex coordinates, but if it proves to be sufficient, a great deal of computation time can be saved (about a factor of 60 for the data set selection).

However, the derivation in Sec. 5.2.1 has to be modified, because without the MDC the measured angle Φ_2 of the Central Detector track will deviate from the "true" angle Φ'_2. The geometry is described in Fig. B.12.

Equation 5.4 is amended by another definition for the parameter d:

$$d = R_1 \cdot \cos\Phi_1 - \Phi_d \tag{B.1}$$

$$d = R_2 \cdot \cos 2\pi + \Phi_d - \Phi_2 \tag{B.2}$$

with the radius of the PS $R_2 = 230$ mm.

The definition of Φ_d in Eq. 5.5 isn't valid in this case. To calculate Φ_d, Eqs. B.1 and B.2 are combined:

$$\begin{aligned}
\frac{R_1}{R_2}\cos(\Phi_1 - \Phi_d) &= \cos(2\pi + \Phi_d - \Phi_2) \\
\frac{R_1}{R_2}(\cos\Phi_1\cos\Phi_d + \sin\Phi_1\sin\Phi_d) &= \cos\Phi_d\cos\Phi_2 + \sin\Phi_d\sin\Phi_2 \\
\sin\Phi_d\left(\sin\Phi_2 - \frac{R_1}{R_2}\sin\Phi_1\right) &= \cos\Phi_d\left(\frac{R_1}{R_2}\sin\Phi_1 - \cos\Phi_2\right) \\
\tan\Phi_d\left(\sin\Phi_2 - \frac{R_1}{R_2}\sin\Phi_1\right) &= \frac{R_1}{R_2}\sin\Phi_1 - \cos\Phi_2,
\end{aligned}$$

which results in

$$\tan\Phi_d = \frac{\frac{R_1}{R_2}\sin\Phi_1 - \cos\Phi_2}{\sin\Phi_2 - \frac{R_1}{R_2}\sin\Phi_1}, \tag{B.3}$$

with $\Phi_d \in [-\frac{\pi}{2}, \frac{\pi}{2}]$.

The fitting procedure follows the description in Sec. 5.2.1, "Monte Carlo Tests", since Eqs. 5.9 and 5.10 are independent of the selection criteria used.

Doing the modified procedure on the unshifted Monte Carlo sample leads to the (uncorrected) values in Table B.7. As expected, the worse angular resolution of the PS gives significantly larger values for both the errors of the vertex coordinates and the distribution widths.

Fig. B.13 shows two d–distributions at $\Phi_d = 20°$. The left one contains data from sample **PP1**, the right one **PP4**.

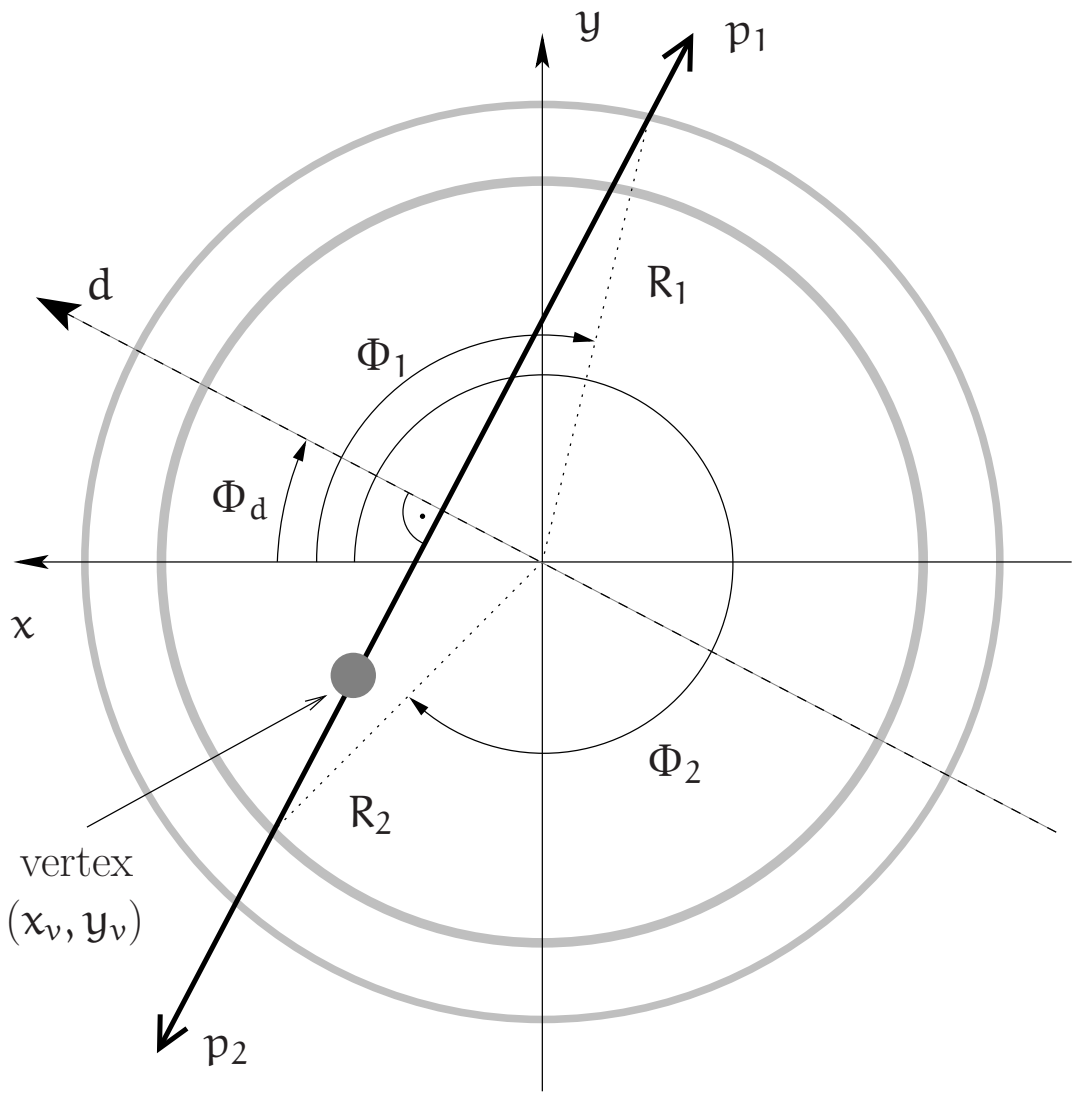

Figure B.12: *Determining the (x, y) vertex without the MDC. The shown geometry is same as in Fig. 5.11 with p_1 and p_2 depicting the projection of the two prongs of an elastic proton–proton event in the (x, y) plane originating from the vertex (x_v, y_v). Both are registered at radii R_1 and R_2 in the FPC and PS, respectively. Again, the deviation of the measured azimuthal opening angle $\Phi_2 - \Phi_1$ is used to calculate the vertex position. See text for further details.*

	PP1 (without MDC)	**PP4** (with MDC)
x_v (mm)	-0.021 ± 1.39	-0.121 ± 0.57
y_v (mm)	0.063 ± 1.22	0.090 ± 0.44

Table B.7: *Comparison of the fit results for samples **PP1** and **PP4**.*

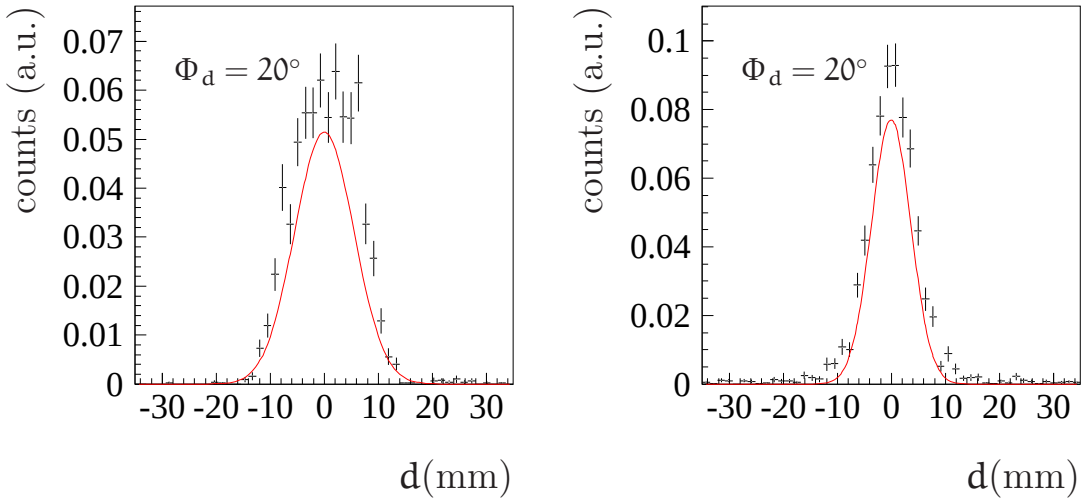

Figure B.13: *Simulated* d*–distributions at* $\Phi_d = 20°$ *for the unshifted sample. The left picture is made with the* ***PP1*** *sample, the right one with* ***PP4****.*

Bibliography

[Ali99] D. Alighieri, *The Divine Comedy*, The ELF project, 1999, http://www.divinecomedy.org/divine_comedy.html, translated by Henry Wadsworth Longfellow.

[ASW00] R. A. Arndt, I. I. Strakovsky and R. L. Workman, *Nucleon nucleon elastic scattering to 3-GeV*, Phys. Rev. C **62**, 034005 (2000).

[B+97] R. Bilger et al., *CELSIUS as an eta factory*, Nucl. Phys. A **626**, 93c–96c (1997).

[Bir64] J. B. Birks, *The Theory and Practice of Scintillation Counting*, Pergamon Press, Oxford, 1964.

[BK73] E. Byckling and K. Kajantie, *Particle Kinematics*, John Wiley & Sons, London, 1973.

[Bro95] W. B. Brodowski, *Design und Aufbau einer Vetowand für den WASA/PROMICE-Detektor am CELSIUS-Speicherring und erste Messungen der Reaktion* $\mathrm{pp} \rightarrow \mathrm{pp}\pi^-\pi^+$, Diploma thesis, Universität Tübingen, Physikalisches Institut, 1995.

[C+78] G. Carron et al., *STOCHASTIC COOLING TESTS IN ICE*, Phys. Lett. B **77**, 353–354 (1978).

[C+96] H. Calén et al., *Detector setup for a storage ring with an internal target*, Nucl. Instrum. Meth. Phys. Res. A **379**, 57–75 (1996).

[CER93a] CERNLIB – Catalog of Program packages and entries, CERN Program Library Short Writeups , 1993.

[CER93b] GEANT – Detector Description and Simulation Tool, CERN Program Library Long Writeup W5013, 1993.

[CER99] PAW – Physics Analysis Workstation User's Guide, CERN Program Library Long Writeup Q121, 1999.

[CHIC03a] P. Golubev et al. (CHIC Collaboration), *CHICSi–a compact ultra-high vacuum compatible detector system for nuclear reaction experiments at storage rings. II. Detectors*, Nucl. Instrum. Meth. Phys. Res. A **500**, 96–115 (2003).

[CHIC03b] L. Westerberg et al. (CHIC Collaboration), *CHICSi–a compact ultra-high vacuum compatible detector system for nuclear reaction experiments at storage rings. I. General structure, mechanics and UHV compatibility*, Nucl. Instrum. Meth. Phys. Res. A **500**, 84–95 (2003).

[CHIC04] L. Carlen et al. (CHIC Collaboration), *CHICSi: A compact ultra-high vacuum compatible detector system for nuclear reaction experiments at storage rings. III: Readout system*, Nucl. Instrum. Meth. Phys. Res. A **516**, 327–347 (2004).

[CK00] H. Calén and A. Kupść, Overview of the CELSIUS/WASA Offline Programs, Manual, 1992, 2000.

[COSY04] H. H. Adam et al. (WASA-at-COSY Collaboration), *Proposal for the Wide Angle Shower Apparatus (WASA) at COSY-Jülich - 'WASA at COSY'*, (2004), nucl-ex/0411038.

[CW93] H. Calén and M. Waters, Calibration of the Forward Detector, PW memo 11/93, 1993.

[D+94] M. Dahmen et al., *A Three layer circular scintillator hodoscope*, Nucl. Instrum. Meth. Phys. Res. A **348**, 97–104 (1994).

[Dyr97] J. M. Dyring, *Detailed Studies of the Reaction* $pp \to pp\eta$ *using a Straw Chamber Tracking Device*, PhD thesis, Uppsala Universitet, 1997.

[E+96] C. Ekstroem et al., *Hydrogen pellet targets for circulating particle beams*, Nucl. Instrum. Meth. Phys. Res. A **371**, 572–574 (1996).

[EDDA04a] D. Albers et al. (EDDA Collaboration), *A precision measurement of p p elastic scattering cross sections at intermediate energies*, Eur. Phys. J. A **22**, 125–148 (2004).

[EDDA04b] F. Bauer (EDDA Collaboration), *Excitation functions of spin correlation parameters A(NN), A(SS), and A(SL) in elastic p(pol.) p(pol.) scattering between 0.45-GeV and 2.5-GeV*, (2004), nucl-ex/0412014.

[EDDA05] M. Altmeier et al. (EDDA Collaboration), *Excitation functions of the analyzing power in elastic proton proton scattering from 0.45-GeV to 2.5-GeV*, Eur. Phys. J. A **23**, 351–364 (2005).

[EW88] T. E. O. Ericson and W. Weise, *Pions and Nuclei*, Clarendon Press, Oxford, 1988.

[Fra04] K. Fransson, Private Message, 2004.

[G+00] J. Greiff et al., *Pion production in* $\mathtt{dp} \to \mathtt{dN}\pi$, Phys. Rev. C **62**, 064002 (2000).

[G+02] J. Greiff et al., *Quasifree bremsstrahlung in the* $\mathtt{dp} \to \mathtt{dp}\gamma$ *reaction above the pion production threshold*, Phys. Rev. C **65**, 034009 (2002).

[Gal67] G. Galilei, *Dialogue Concerning the two Chief World Systems: the Ptolemaic and the Copernican*, University of California Press, Berkeley and Los Angeles, second edition, 1967, translated by S. Drake.

[GP60] P. Gooding and H. Pugh, *The response of plastic scintillators to high-energy particles*, Nucl. Instrum. Meth. **7**, 189 (1960).

[Gre99] J. Greiff, *Investigation of Inelastic Reactions in Deuteron Proton Collisions Between* $\mathsf{T}_\mathtt{d}$ *= 437 and 559 MeV Using the PROMICE/WASA Detector at CELSIUS*, PhD thesis, Universität Hamburg, Institut für Experimentalphysik, 1999.

[Gre01] J. Greiff, z-Vertex-Distribution for WASA, obtained with elastic pp-scattering., WASA memo 02/01, 2001.

[Gri87] D. Griffiths, *Introduction to Elementary Particles*, John Wiley & Sons, New York, 1987.

[H+91] D. A. Hutcheon et al., *Measurements of* $N\,N \to d\,\pi$ *very near threshold. 1. The* $n\,p \to d\,\pi^0$ *cross-section*, Nucl. Phys. A **535**, 618–636 (1991).

[H+04] M. N. Harakeh et al., editors, *NuPECC long range plan 2004: Perspectives for nuclear physics research in Europe in the coming decade and beyond. NuPECC report*, April 2004, Europ. Sci. Found. Strasbourg - (04/04,rec.Aug.) 181 p.

[Hag63] R. Hagedorn, *Relativistic Kinematics*, W. A. Benjamin, Inc., New York, Amsterdam, 1963.

[Höi79] B. Höistad, *Pion Production in Proton–Nucleus Collisions*, Adv. Nucl. Phys. **11**, 135–178 (1979).

[Jac04] M. Jacewicz, *Measurement of the Reaction* $\mathtt{pp} \to \mathtt{pp}\pi^+\pi^-\pi^0$ *with CELSIUS/WASA at 1.36 GeV*, PhD thesis, Uppsala Universitet, 2004.

[Jam68] F. James, *Monte Carlo Phase Space*, (1968), CERN Lectures 1967-1968.

[Jam77] F. James, FOWL - a General Monte–Carlo Phase Space Program, CERN Program Library Long Writeup W505, 1977.

[Jam98] F. James, MINUIT – Function Minimization and Error Analysis, CERN Program Library Long Writeup D506, 1998.

[Klo03] V. Klose, *Ereignisrekonstruktion der Reaktion* $pp \to pp(\eta \to \gamma\gamma)$ *bei 1300 MeV mit dem CELSIUS/WASA Experiment*, Diploma thesis, Universität Hamburg, Institut für Experimentalphysik, 2003.

[Kno79] G. F. Knoll, *Radiation Detection and Measurement*, John Wiley & Sons, New York, 1979.

[Koc97] I. Koch, *Luminositätsmessungen des Experiments* $dp \to dp\pi^0$ *mit Hilfe von Halbleiterdetektoren*, Diploma thesis, Universität Hamburg, Institut für Experimentalphysik, 1997.

[Koc04] I. Koch, *Measurements of* $2\pi^0$ *and* $3\pi^0$ *Production in Proton–Proton Collisions at a Center of Mass Energy of 2.465 GeV*, PhD thesis, Uppsala Universitet, 2004.

[Kul87] S. Kullander, WASA: Wide Angle Shower Apparatus for particle physics at CELSIUS, Proposal to the TSL, 1987.

[Kul00] S. Kullander, *Swedish accelerators take a look at the past*, CERN Cour. **40N4**, 20–22 (2000).

[Kup02] A. Kupść, CWlib C++ Libraries for CELSIUS/WASA, Manual, 2002.

[LeC01] LeCroy Research Systems, Product Datasheet Library, http://www.lecroy.com/lrs/dsheets/dslib.htm, 2001.

[Leh01] C. Lehmann, *Zeitverhalten von Prototypen eines ortsauflösenden Szintillatorhodoskops für das CELSIUS-WASA-Experiment*, Diploma thesis, Universität Hamburg, Institut für Experimentalphysik, 2001.

[M+92] H. O. Meyer et al., *Total cross-section for* $p + p \to p + p + \pi^0$ *close to threshold*, Nucl. Phys. A **539**, 633–661 (1992).

[Mar01] P. Marciniewski, *Fast digital Trigger Systems for Experiments in High Energy Physics*, PhD thesis, Uppsala Universitet, 2001.

[Mes99] O. Messner, *Design and Setup of the Window Hodoscope for the new WASA 4π-Detector at CELSIUS*, Diploma thesis, Universität Tübingen, Physikalisches Institut, 1999.

[MHE87] R. Machleidt, K. Holinde and C. Elster, *The Bonn Meson Exchange Model for the Nucleon Nucleon Interaction*, Phys. Rept. **149**, 1–89 (1987).

[MID01] MIDAS PSI Home Page, http://midas.psi.ch, 2001.

[MM79] D. F. Measday and G. A. Miller, *Hopes and Realities for the (p, π) Reaction*, Ann. Rev. Nucl. Part. Sci. **29**, 121–160 (1979).

[MN93] H. O. Meyer and J. A. Niskanen, *Quasifree pion production in the three nucleon system*, Phys. Rev. C **47**, 2474–2480 (1993).

[Nef95] B. M. K. Nefkens, *What is so special about eta meson physics?*, Few Body Syst. Suppl. **9**, 193–202 (1995).

[OP47] G. P. S. Occhialini and C. F. Powell, *Nuclear disintegration produced by slow charged particles of small mass*, (1947), In *Bristol 1987, Proceedings, 40 years of particle physics* 197-201. Nature 159 (1947) 186-190. (see HIGH ENERGY PHYSICS INDEX 29 (1991) No. 6809).

[P+04] C. Pauly et al., Multipionic Final States at CELSIUS/WASA, Presented at the MESON 2004 Workshop, Cracow, Poland, June 4–8, 2004.

[Pät02] J. Pätzold, *Exclusive Measurement of the* $\mathrm{pp} \to \mathrm{pp}\pi^+\pi^-$ *Reaction Close to Threshold*, PhD thesis, Universität Tübingen, Physikalisches Institut, 2002.

[Pau01] C. Pauly, *Untersuchung von Lichtausbeute und Ansprechvermögen an Prototypen eines ortsauflösenden Szintillatorhodoskops für das CELSIUS/WASA-Experiment*, Diploma thesis, Universität Hamburg, Institut für Experimentalphysik, 2001.

[Pau05] C. Pauly, Dissertation in preparation, 2005.

[PDG04] S. Eidelman et al. (PDG Collaboration), *Review of particle physics*, Phys. Lett. B **592**, 1 (2004).

[R+93] H. Rohdjess et al., *Total cross-section for* $p + d \to p + d + \pi^0$ *close to threshold*, Phys. Rev. Lett. **70**, 2864–2867 (1993).

[Roh94] H. Rohdjeß, *Pion Production in pd Reactions Close to Threshold*, PhD thesis, Universität Hamburg, Institut für Experimentalphysik, 1994.

[Roh95] H. Rohdjeß, Determining COSY Beam Parameters from Elastic Proton–Proton Scattering, EDDA internal report 95–04, 1995.

[Rub99] R. Ruber, *An ultra–thin walled superconducting solenoid for meson–decay physics*, PhD thesis, Uppsala Universitet, 1999.

[S+82] F. Shimizu et al., *Measurement of the p p cross-sections in the momentum range 0.9 GeV/c – 2.0 GeV/c*, Nucl. Phys. A **386**, 571 (1982).

[SAI04] CNS Data Analysis Center, SAID Home Page, http://gwdac.phys.gwu.edu, 2004.

[Sch00] C. Schuck, Project Work, 2000, Uppsala Universitet.

[Sco99] W. Scobel, Investigation of inelastic dp reactions at WASA/CELSIUS with deuteron projectiles, Proposal to the TSL, accepted as **CA55** in April 1999.

[Sco01] W. Scobel, Position Sensitive Extension of the WASA Forward Range Hodoscope, Proposal to the TSL, accepted as **CA70** in Mai 2001.

[Sta03] Y. Stark, *Commissioning of a position sensitive hodoscope for the CELSIUS/WASA experiment*, Diploma thesis, Universität Hamburg, Institut für Experimentalphysik, 2003.

[Tho92] H. D. Thoreau, *Walden*, Princeton University Press, Princeton, New Jersey, fifth edition, 1992.

[Tro95] B. Trostell, *Vacuum injection of hydrogen microsphere beams*, Nucl. Instrum. Meth. Phys. Res. A **362**, 41–52 (1995).

[TSL98] The Svedberg Laboratory, Uppsala University, Progress Report 1996 - 1997, 1998.

[TSL99] The Svedberg Laboratory, Brochure, 1999.

[TSL00] The Svedberg Laboratory, Uppsala University, Progress Report 1998 - 1999, 2000.

[TSL02] The Svedberg Laboratory, Uppsala University, Progress Report 2000 - 2001, 2002.

[Zło03] J. Złomańczuk, Odin User's Guide, Manual, 2003.

Acknowledgement

While I sit here, finally at the end, and do contemplate about the twists and turns that the adventure of the past years took, I cannot help myself but feel that more often than not,

> *I found myself within a forest dark,*
> *For the straightforward pathway had been lost.*
> — The Inferno, Canto I, lines 2-3 ([Ali99]).

Methinks, however, that I have been blessed nevertheless, for my voyage was never a lonely one, having dear companions and guides on my long way round. Therefore, I like to express my deepest gratitude towards ...

... Wolfgang Scobel, who supported me in every way possible to make this thesis happen. Having been at my best and my worst, I deeply appreciate your guidance and patience, giving me the time I needed to get from there to here.

... all the experts in Uppsala, namely Hans Calén, Kjell Fransson, Jan Greiff, Andrzej Kupść, Paweł Marciniewski, and Magnus Wolke, who were always helpful and sympathetic, regardless how unreflected my inquiries have been.

... Oleg Eyser, who shared many a ride with me through the absurdities of life, and Christian Pauly and Marek Jacewicz, my "comrades-in-arms", for sharing my up's and down's in the past years. It would have been half the fun and double the pain without your friendship.

... all the (ex–)students that shared my time in Hamburg and Uppsala: Filippo Cappellaro, Inken Koch, Tatiana Skorodko, Jens Pätzold, Mikhail Bashkanov, Yuliya Stark, and Verena Klose, to name a few, who made this experience worthwhile.

... the technical personnel in Hamburg, namely Wolfgang Gärtner, Norbert Schirm, Helmut Krause, Ronald Mohrmann, and Rainer P. Feller, who are all artist in their fields and moreover fun to work with.

... my parents for their loving support. Ellerinizden ve gözlerinizden öperim.